Since 1955

Strojniški vestnik
Journal of Mechanical Engineering

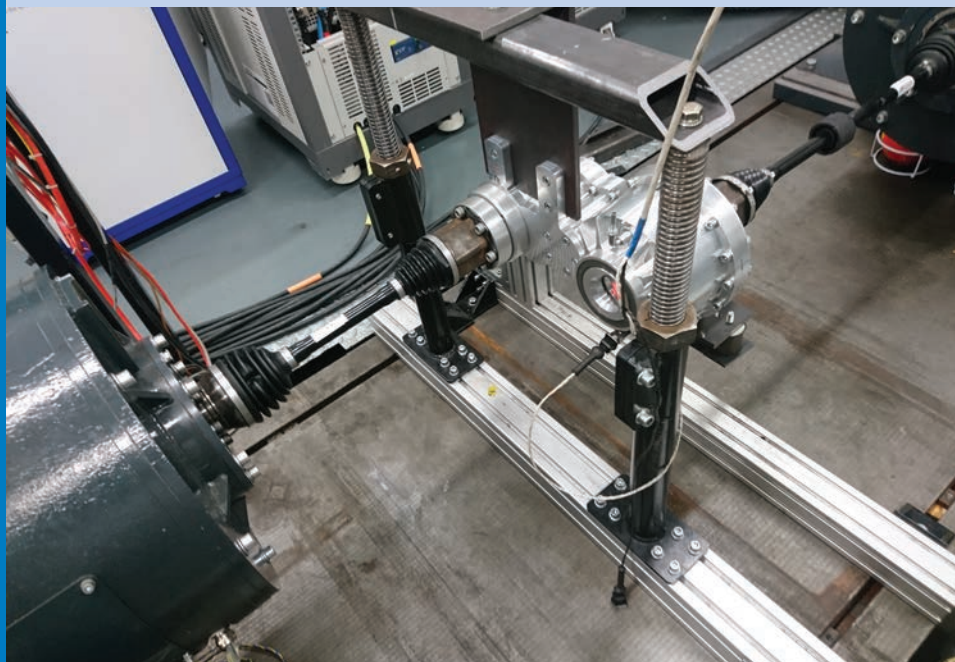

no. 5
year 2022
volume 68

Strojniški vestnik – Journal of Mechanical Engineering (SV-JME)

Aim and Scope
The international journal publishes original and (mini)review articles covering the concepts of materials science, mechanics, kinematics, thermodynamics, energy and environment, mechatronics and robotics, fluid mechanics, tribology, cybernetics, industrial engineering and structural analysis.
The journal follows new trends and progress proven practice in the mechanical engineering and also in the closely related sciences as are electrical, civil and process engineering, medicine, microbiology, ecology, agriculture, transport systems, aviation, and others, thus creating a unique forum for interdisciplinary or multidisciplinary dialogue.
The international conferences selected papers are welcome for publishing as a special issue of SV-JME with invited co-editor(s).

Editorial Office
University of Ljubljana, Faculty of Mechanical Engineering
SV-JME, Aškerčeva 6, SI-1000 Ljubljana, Slovenia
Phone: 386 (0)1 4771 137
Fax: 386 (0)1 2518 567
info@sv-jme.eu, http://www.sv-jme.eu

Print: Demat d.o.o., printed in 250 copies

Founders and Publishers
University of Ljubljana, Faculty of Mechanical Engineering, Slovenia
University of Maribor, Faculty of Mechanical Engineering, Slovenia
Association of Mechanical Engineers of Slovenia
Chamber of Commerce and Industry of Slovenia, Metal Processing Industry Association

Cover:
A single-speed aluminium alloy gearbox specially developed for a four-motor autonomous modular battery electric vehicle to transfer power between the electric motor and the vehicle wheel.
The gearbox was tested in detail in the powertrain testbed using a suitable methodology. The chosen methodology consisted of connecting the input and output shafts of the gearbox to two dynamometers using drive shafts and then loading the gearbox with speed and torque. This methodology made it possible to determine its mechanical efficiency during different driving cycles.

Image Courtesy: Tomas Petr, Josef Brousek, Jakub Jezek, Tomas Zvolsky, Robert Vozenilek, Technical University of Liberec, Dept. of Vehicle and Engines, Czech Republic, © The Authors, CC BY 4.0 Int.

General information
Strojniški vestnik – Journal of Mechanical Engineering is published in 11 issues per year (July and August is a double issue).

Institutional prices include print & online access: institutional subscription price and foreign subscription €100,00 (the price of a single issue is €10,00); general public subscription and student subscription €50,00 (the price of a single issue is €5,00). Prices are exclusive of tax. Delivery is included in the price. The recipient is responsible for paying any import duties or taxes. Legal title passes to the customer on dispatch by our distributor. Single issues from current and recent volumes are available at the current single-issue price. To order the journal, please complete the form on our website. For submissions, subscriptions and all other information please visit: *http://www.sv-jme.eu*.

You can advertise on the inner and outer side of the back cover of the journal. The authors of the published papers are invited to send photos or pictures with short explanation for cover content.

We would like to thank the reviewers who have taken part in the peer-review process.

ISSN 0039-2480, ISSN 2536-2948 (online)

The journal is subsidized by Slovenian Research Agency.

SV-JME is indexed / abstracted in: SCI-Expanded, Compendex, Inspec, ProQuest-CSA, SCOPUS, TEMA. The list of the remaining bases, in which SV-JME is indexed, is available on the website.

Strojniški vestnik - Journal of Mechanical Engineering is available on *https://www.sv-jme.eu*.

Contents

Strojniški vestnik - Journal of Mechanical Engineering
volume 68, (2022), number 5
Ljubljana, May 2022
ISSN 0039-2480

Published monthly

Papers

Strojniški vestnik - Journal of Mechanical Engineering 68(2022)5, 303-313
DOI:10.5545/sv-jme.2021.7437
Original Scientific Paper
Received for review: 2021-10-12
Received revised form: 2022-02-21
Accepted for publication: 2022-03-07

Measuring the Efficiency of Reduction Gearboxes for Electric Utility Vehicles during Specific Driving Cycles

Tomas Petr* – Josef Brousek – Jakub Jezek – Tomas Zvolsky – Robert Vozenilek
Technical University of Liberec, Department of Vehicle and Engines, Czech Republic

This paper presents the results and the procedure for measuring the efficiency of a single-speed reduction gearbox developed for an autonomous electric utility vehicle. The resulting efficiency of the gearbox was investigated on three different driving cycles, which were selected because their speed profiles most closely matched the expected use of the autonomous vehicle. The required torque for each cycle was obtained from simulations of the vehicle's driving behaviour including its predicted mass and dimensional parameters after a given driving cycle. The results of this research represent the achieved efficiency and average power loss of the gearbox on each driving cycle. The resulting gearbox efficiency was around 50 % in the predominant areas of driving cycles.
Keywords: efficiency, gearbox, powertrain, electric vehicle, driving cycle

Highlights
- *Presentation of a method for measuring the instantaneous efficiency of a separate gearbox during driving cycle.*
- *Study of a gearbox designed for an autonomous electric utility vehicle.*
- *The efficiency of the gearbox can have a significant effect on the electric powertrain efficiency in certain cases.*
- *The gearbox achieved average efficiency values of around 50 % in the predominant driving cycle areas.*

0 INTRODUCTION

One of the most significant disadvantages of car transport is its adverse impact on the environment. For this reason, car manufacturers are under constant pressure from national governments to reduce the pollutants produced by internal combustion engine cars. This pressure has resulted in the search for new solutions to develop internal combustion engine vehicles or new alternative means of propulsion for these vehicles, as hybrid electric vehicles (HEV), plug-in hybrid electric vehicles (PHEV), battery electric vehicles (BEV), etc. Car manufacturers are also under pressure from customers to maintain optimum performance, low consumption (in the case of high mileage electric vehicles (EVs)) and low prices. For this reason, it is now essential to look for possible compromises and ways to achieve the desired result.

One of the ways to reduce emissions or increase the range of electric vehicles, a topic which is currently being addressed by a large number of researchers, is the optimization of individual powertrain components to reduce energy loss in the drive train of the car [1] and [2]. Other researchers say that the so-called Achilles heel of electric vehicles is its batteries [3].

The results [4] show a trend towards improved power train efficiency for all types of conventional cars, with the comparative average power train efficiency for all vehicles in the categories reaching 18 % in 2005 and 20.9 % in 2013. In this study, the powertrain efficiency of 37 pairs of conventional vehicles of the same model was compared for the years 2005 and 2013. The eighteen pairs were passenger cars, two pairs were minivans, twelve pairs were sport utility vehicles (SUV) and five pairs were pickup trucks [5].

In general, the tank-to-wheel efficiency of the vehicles with internal combustion engines is 14 % to 30 % for gasoline and 28 % to 42 % for diesel. The powertrain of an electric vehicle has a significantly higher efficiency of 60 % to 80 %. In BEVs, the lossiest components are the electric motor, electric generator and the mechanical transmission if the electric vehicle is equipped with one [6].

In this study, we investigated the efficiency of the gearbox for an autonomous electric utility vehicle, which, according to previous research, together with the efficiency of the electric motor, has a significant effect on the overall energy consumption of electric vehicles [6].

In general, gearbox efficiency is investigated in two basic ways. One way is through the use of mathematical models and advanced simulations, and the other important tool is experimental measurements. Experimental measurements of gearbox efficiency are usually performed at dedicated test benches with electric dynamometers, and experiments of ten measure efficiency over the full range of operating input speed and input torque of the gearbox. In contrast, the energy consumption of electric vehicles is commonly measured and investigated during driving cycles.

*Corr. Author's Address: Technical University of Liberec, Department of Vehicle and Engines, Czech Republic, tomas.petr@tul.cz

By investigating energy consumption in a driving cycle the effects of individual powertrain components can also be investigated. We ask the question, what is the effect of gearbox efficiency on the energy consumption of an electric vehicle on a drive cycle? We would like to answer it using data from experimental measurement of the gearbox over the full range of input speed and input torque. We would have to simulate driving the vehicle, in which we would specify the data from the gearbox efficiency measurement as one of the simulation parameters.

Therefore, as part of the research and development of electric powertrains for electric utility vehicles, we asked the question, how would it be possible to directly measure gearbox efficiency during driving cycles? Such results could provide us with accurate and valuable data on the effect of gearbox efficiency on the energy consumption of electric vehicles during the driving cycles, while also providing valuable insights for the development of electric vehicle gearboxes. To answer the questions posed and also to provide such experimental measurement data, we experimentally measured gearbox efficiency in our power train laboratory, which allows such experimental measurements to be conducted during driving cycles, and we present this efficiency measurement method along with the results of our measurements.

1 METHODS

In this work, we investigated the efficiency of a gearbox for an electric utility vehicle during driving cycles. Gearbox efficiency is usually given either as a number or as a set of curves which show the dependence on speed or torque. Gearbox efficiency η is calculated as follows:

$$\eta = \frac{P_2}{P_1} \cdot 100\,\% = \frac{\omega_2 \cdot M_2}{\omega_1 \cdot M_1} \cdot 100\,\% = \frac{2\pi \cdot n_2 \cdot M_2}{2\pi \cdot n_1 \cdot M_1} \cdot 100\,\%, \quad (1)$$

where P_2 is the output power of the gearbox, P_1 is the input power of the gearbox, ω_2 is the output angular velocity, M_2 is the output torque, ω_1 is the input angular velocity, M_1 is the input torque of the gearbox and n_2 and n_1 are the speeds of the output and input shafts of the gearbox. The range of values of the efficiency during our experiment is $-1 \leq \eta \leq 1$. The efficiency becomes negative when the vehicle is significantly decelerating, and power is transmitted in the opposite direction to acceleration or steady-state driving.

Efficiency values for a conventional manual passenger car gearbox is typically in the range of 92 % to 97 %. Typical values for truck gearbox are 80 % to 97 %. The efficiency of the individual pairs of spur gears is approximately 97 % to 98 %. In the case of bevel gears, the efficiency is estimated at 90 % to 95 % [7]. Load-independent losses are due to gears grinding in the oil bath and grinding of bearings. This groups also consists of losses arising in the seals, and other losses [8].

To perform experimental measurements gearbox efficiency during driving cycles, we obtained input data for the experiment in the form of input and output values for gearbox speed and torque based on the driving resistance forces of the vehicle. For this purpose, we used an advanced vehicle driving simulation on the drive cycles in software Ricardo Ignite [9] to provide the input data for the experiment. This data was then used as input to the control system of the powertrain test bench where we measured the efficiency of the gearbox. During the experiment, we measured and recorded the input and output speeds and torque values of the gearbox. We then processed the measured data in Matlab software to obtain results for the efficiency and power losses of the gearbox during the driving cycles.

We performed experimental measurements on three driving cycles of vehicles designed for close operational use of an autonomous platform for which the measured gearbox is being developed.

1.1 Tested Gearbox

The gearbox for the autonomous battery electric modular platform developed at the Technical University of Liberec was selected for study. Based on our previous research and development in gearboxes for electric vehicles, we developed our own gearbox.

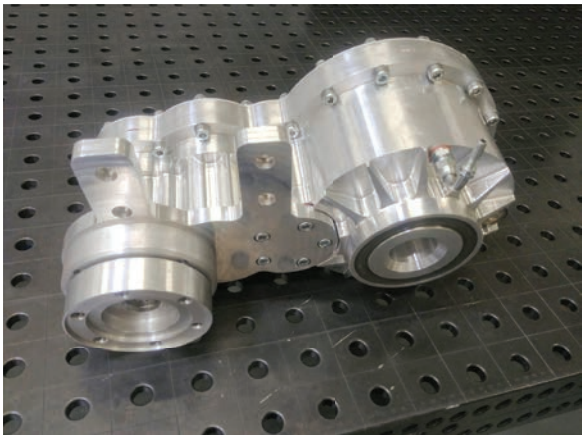

Fig. 1. *Tested gearbox for the autonomous battery electric modular platform*

The vehicle will be driven independently by four electric motors, making it possible to design the transmission without a differential and the use of advanced torque vectoring technology for steering. Because the vehicle has four motors, four identical gearboxes will be fitted, housed in two assemblies, one on each axle (Fig. 1). Each single-speed gearbox has a gear ratio of 11.447 : 1 with a maximum input torque of 60 Nm and a maximum input speed of 6000 r pm.

In designing the gearbox, we were severely limited by the requirement to make one design for all four motors. A gearbox layout is shown in Fig. 2. The gearbox consists of four shafts and six gear wheels, which are partially taken from the Skoda Auto MQ200 automotive gearbox to reduce the production cost and eight bearings produced by SKF. The specific types of bearings used on each shaft are shown in Table 1. The sealing of the oil filling in the gearbox is ensured by shaft seals on the input and output shafts. The material of the housing is aluminium alloy EN AW 6061 T6.

Table 1. *Used bearings*

Shaft	Bearings A	Bearings B
Input shaft	BK3016	6205
First counter shaft	4206 ATN9	HK 3020
Second counter shaft	32005 X	32005 X
Output shaft	6014	NK70/25

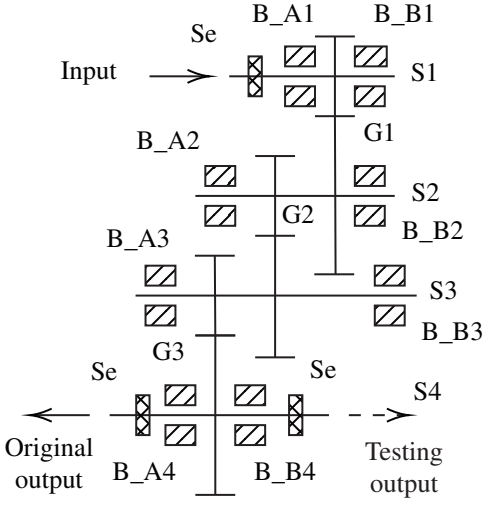

B_A - Bearings A | B_B - Bearings B
G - Gear ratio | $S1$ - Input shaft
$S2$ - 1st countershaft | $S3$ - 2nd countershaft
$S4$ - Output shaft | Se - Sealing

Fig. 2. *Tested gearbox layout*

1.1 Simulation of the Vehicle's Driving on the Driving Cycles

The torque required to move the vehicle at each instant was calculated from the parameters of the developed modular platform using Ricardo Ignite [9] simulation software. The main parameters defined in the simulation model are shown in Table 2. The other parameters required for the torque calculation were left at their default values.

Table 2. *Vehicle parameters*

Parameters	Value
Vehicle frontal area [m^2]	1.925
Aerodynamic drag coefficient	0.7
Rolling resistance coefficient	0.08
Tire size	225/65 R17, 325/80 R22.5
Vehicle mass [kg]	3000

The driving cycles for our experimental measurements were selected according to two criteria. The first criterion was a speed limit based on the maximum input speed that our dynamometer is capable of producing. The second criterion was selection of a cycle with a speed profile that would match the expected use of the autonomous modular platform, which is expected to be applied, for example, in mines, ports or warehouses. To assess the magnitude of the total efficiency in the gearbox, three types of driving cycles were selected. These are the CARB Heavy Heavy-Duty Diesel Truck (HHDDT) Creep Segment (CARB HHDDT CS), Central Business District (CBD) Segment of the Transit Coach Operating Duty Cycle (CBD SoTCODC) and NREL Port Drayage Creep Cycle (California) (NREL PDCQC) cycles. Fig. 3 and Table 3 show the basic parameters and speed profiles of the individual driving cycles which the experiment measured [10].

Table 3. *Driving cycle parameters*

Cycle	Time [s]	Distance [km]	Maximal speed [kmh^{-1}]	Avg. driving speed [kmh^{-1}]
CARB-HHDDT-CS	253	0.19	13.19	4.85
CBD-SoTCODC	560	3.29	32.18	25.65
NREL-PDCQC	1330	0.41	20.05	8.36

The data show that the CARB HHDDT CS cycle was the shortest of the lowest cycles examined, with the lowest maximum and average speeds. The CBD–SoTCODC cycle attained medium values. By contrast, the NREL PDCQC cycle attained the highest values

for cycle duration, maximum and average speed. For the CBDS oTCODC cycle, a different tire size was selected because of its maximum speed.

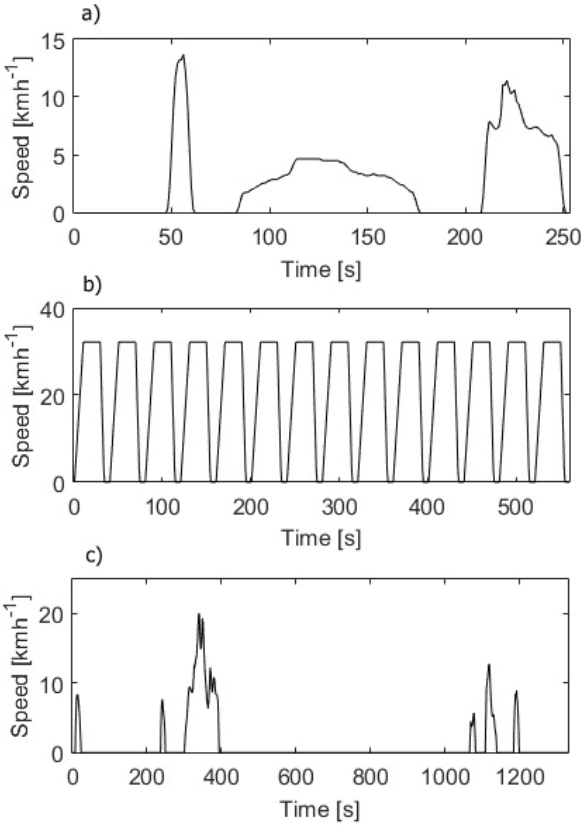

Fig. 3. *Speed profiles of investigated driving cycles, a) CARB Heavy Heavy-Duty Diesel Truck (HHDDT) Creep Segment, b) Central Business District (CBD) Segment of the Transit Coach Operating Duty Cycle, c) NREL Port Drayage Creep Queue Cycle (California)*

1.2.1 CARB Heavy Heavy-Duty Diesel Truck (HHDDT) Creep Segment

The Creep Segment contains the speed profile of the CARB HHDDT driving cycle. The test cycle on a cylindrical dynamometer developed by the California Air Resources Board (CARB) and West Virginia University measures emissions from heavy-duty diesel trucks in slow mode. This type of driving cycle corresponds to the ordinary use of a heavy-duty trucks with a total weight of around 4.000 kg. This driving cycle is used to measure vehicle emissions on a chassis dynamometer [10] and [11].

1.2.2 Central Business District (CBD) Segment of the Transit Coach Operating Duty Cycle

The Central Business District segment of the Transit Coach Operating Duty Cycle (SAE J , also known as the BusinessA rterialC ommuter Cycle. A cycle consists of 4 repetitions with an acceleration ramp, maintaining speed at 3.8 km/h, followed by deceleration. It simulates passenger boarding and alighting in a business district with frequent stops and heavy traffic [10].

1.2.3 NREL Port Drayage Creep Queue Cycle(California)

This driving cycle was developed by NREL with data from vehicles operating at the Ports of Los Angeles and Long Beach. This cycle is very similar in kinematic intensity to the driving cycle given in the Section 1.2.1.

1.3 Powertrain Test Bench

The powertrain test bench was designed to test and optimize the parameters and long-term testing of the vehicle's powertrain. The test bench is equipped with four asynchronous dynamometers. These dynamometers are divided into pairs for testing the front and rear axles of the vehicle. The first pair of Siemens ADG 2 WP dynamometers located on the front axle, achieves a maximum output of kW at 0 rpm. The second pair of Siemens 111 ADG 2 WP dynamometers representing the car's rear axle, has a maximum output of 111 kW at 0 rpm. The device is controlled by a Simatic S7 0 PLC control system and LabView programming environment. Torque measurement is performed using HBM T F strain gauge flanges with a measuring range of kN m and sensitivity of 0.1 %, which ensures the accuracy of measurement even with dynamic speed variations.

1.4 Experiment Description

The gearbox was placed between two dynamometers on a unique frame consisting of aluminum profiles and a steel weldment. The input shaft of the gearbox was connected to one dynamometer, which operated in motor mode, using a semi-axle from Skoda Auto. The output shaft of the gearbox was connected in the same way to a second dynamometer located opposite the first. The second dynamometer was operated in torque mode. The gearbox in the test bench is shown in Fig. 4. The method of connecting the input and output of the gearbox to the dynamometers using

the Skoda Auto semi-axles imposed a maximum input speed limit of 2000 rpm in our experiment. A maximum input speed of 2000 rpm corresponds approximately to a vehicle speed of 24 km/h (with tire size 225 65 R17 corresponding to off-road tires) or a speed of approximately 80 km/h (with tire size 295 80 R22.5 corresponding to truck tires). However, this limitation on the maximum vehicle speed, considering the driving cycles used, limited us to only the (NREL–PDCQC) cycle, in which the maximum input speed limit on the gearbox would be exceeded. For this cycle, we therefore chose a tire size of 328 80 R22.5 with which the input speed limit was not exceeded.

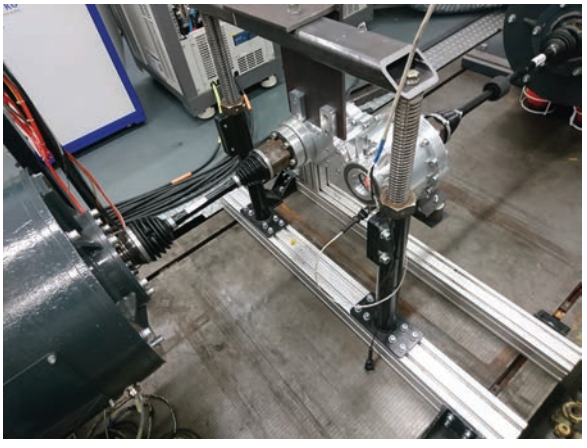

Fig. 4. *Gearbox in the test bench*

First, it was necessary to obtain input data for the control system of the powertrain test bench. As mentioned in the methods chapter, we used the advanced Ricardo Ignite [9] software tool for this purpose. With this software, for each selected driving cycle, we simulated vehicle driving with the parameters listed in Table 2. From the simulation, we obtained the input speed and the total input torque of the gearbox as if the vehicle were driven by a single motor. Since the gearbox was designed for a vehicle powertrain with four motors and four gearboxes, we divided the total input torque obtained by four. We input the obtained simulation data into the control system of the powertrain test bench. We then performed three experimental measurements with the test bench: one measurement for each selected driving cycle, in which the control system, according to the input data from the gearbox, powered the driving cycle as if the gearbox has been placed in a real vehicle.

During the experiment, the control system recorded the input and output speeds and torques of the gearbox from sensors on both dynamometers. The oil temperature in the gear box was measured by the temperature sensor in the gearbox and recorded. The ambient temperature was measured and recorded in the same manner. The speed and torque values were recorded every 0.01 s and the temperature values every 0.1 s .

Measuring the efficiency of a mechanical gearbox over a complete driving cycle is a highly complex process. As mentioned earlier, the values of each input power and output power component were logged every 0.01 s. From each sequential 100 values logged (100 values = 1 s), an average value was calculated for each input power and output power component, which is shown as a circle in the Fig. 5 for illustration purposes in the drive cycle CARB-HHDDT-CS.

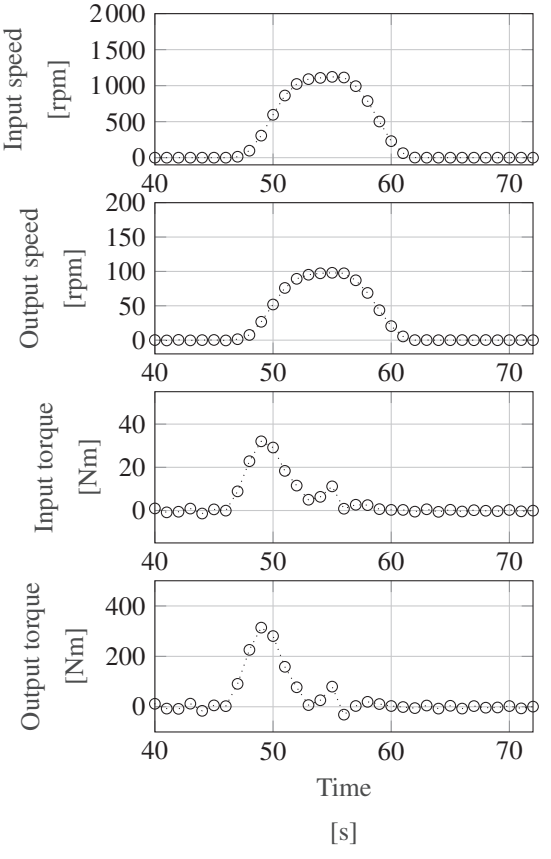

Fig. 5. Detail of parameter processing for the CARB-HHDDT-CS

Subsequently, from the obtained average values of the input and output power components, the values of input power, output power and efficiency were calculated according to the Eq. (1). For illustrative purposes, these values are similarly presented in the following CARB-HHDDT-CS driving cycle detail in Fig. 6

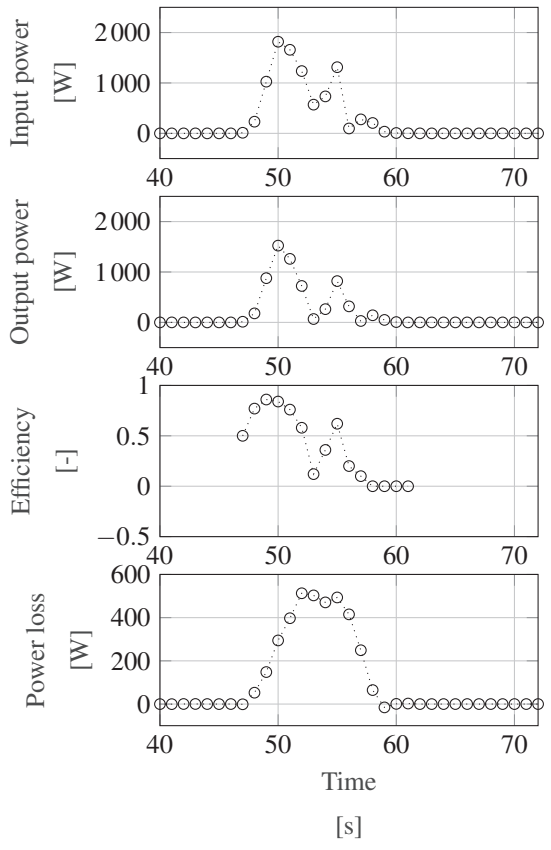

Fig. 6. *Detail of the calculated results of the CARB HHDDT Creep Segment driving cycle measurement*

The areas where the vehicle is not driving were considered as undefined areas. In this condition, the determined efficiency would correspond to the Eq. (2). For these areas, the efficiency was not defined. Simultaneously, the efficiency values in these areas are not shown in the resulting graphs.

$$\eta = \frac{P_2}{P_1} = \frac{0}{0} \Rightarrow \text{undefined.} \tag{2}$$

We would like to note here that the reported gearbox efficiency results will probably still be slightly affected by the semi-axles used to connect the gearbox to both dynamometers. According to the experiment conducted in **[12]**, we can note that the efficiency of a single shaft joint can range about 97 % to 99 %. A further note relates to oil temperature that the experiments were conducted with gearbox oil temperatures in the range of 26 °C to 28 °C and ambient temperatures around 24 °C. The gearbox was filled with gear oil with viscosity class SAE 80.

2 RESULTS

The results of the experiment are shown in the Figs. 7 to 9. The figures show the dependencies of input and output speed, input and output torque, input and output power, efficiency and power loss per unit time. We describe the results for driving cycles CARB–HHDDT Creep Segment, CBDS oTCODC and NREL Port DCQC below. Fig. 7 shows the results for the CARB–HHDDT Creep Segment driving cycle. In this driving cycle, the gearbox was operated at three speed ranges that correspond to the prescribed vehicle cycle speed profile. The first section was slightly above the 1000 rpm input speed value, the second section was at a lower speed, approximately 800 rpm to 900 rpm, and during the third section, the gearbox input speed was in the range of 900 rpm to 1000 rpm. The gearbox input torque corresponding to the torque required by the vehicle to handle the specified speed profile of the driving cycle rose briefly during the first section to a maximum value of 80 Nm. During the second section, it was fairly constant mostly around the value of 10 Nm. During the third section, three torque peaks can be observed in the range of 15 Nm to 80 Nm at changes in the vehicle's speed. The gearbox efficiency values peaked at 97 % to 98 % in all three sections, with the efficiency results varying over time during the cycle due to the relatively dynamic input torque profile. The instantaneous power loss values, which correspond to the value of dissipated power in the gearbox during the cycle, reached a maximum value of 602 W in the first section. In the second section, the values were around 100 W, and in the third section, a maximum value of 408 W was reached. The average power loss was 69 W. Fig. 8 shows the results for the CBDS oTCODC. The speed profile of this driving cycle consisted of fifteen sections, in which the input speed of the gearbox increased to 1831 rpm each time after a defined ramp and then dropped again to zero. The gearbox was loaded with a maximum input torque of 44.5 Nm in each section. The maximum gearbox efficiency value was 99 %.The maximum power loss value achieved at a steady speed of 913 W, and the average power loss value during the cycle was 48 W. Fig. 9 shows the results for NREL Port DCQC. Six relatively short speed starts and stops with different profiles were performed during this cycle. The maximum input speed of the gearbox was 657 rpm. The maximum input torque was 365 Nm. The maximum gearbox efficiency value was 99.8 %. The maximum value of power loss in the gearbox was 857 W, and the average value of power loss during the cycle was 23.8 W.

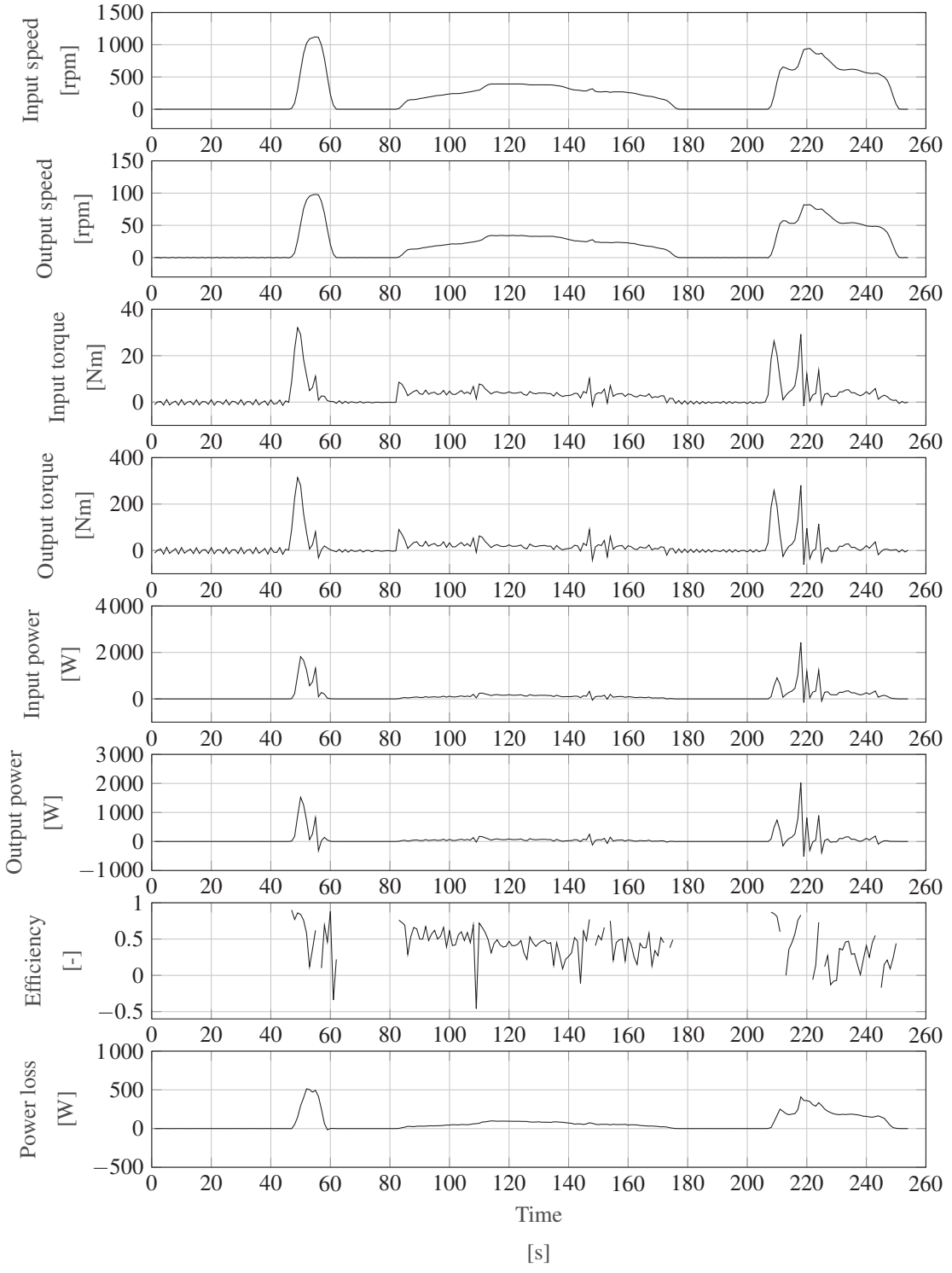

Fig. 7. *Input, output and calculated data for CARB Heavy Heavy-Duty Diesel Truck (HHDDT) Creep Segment*

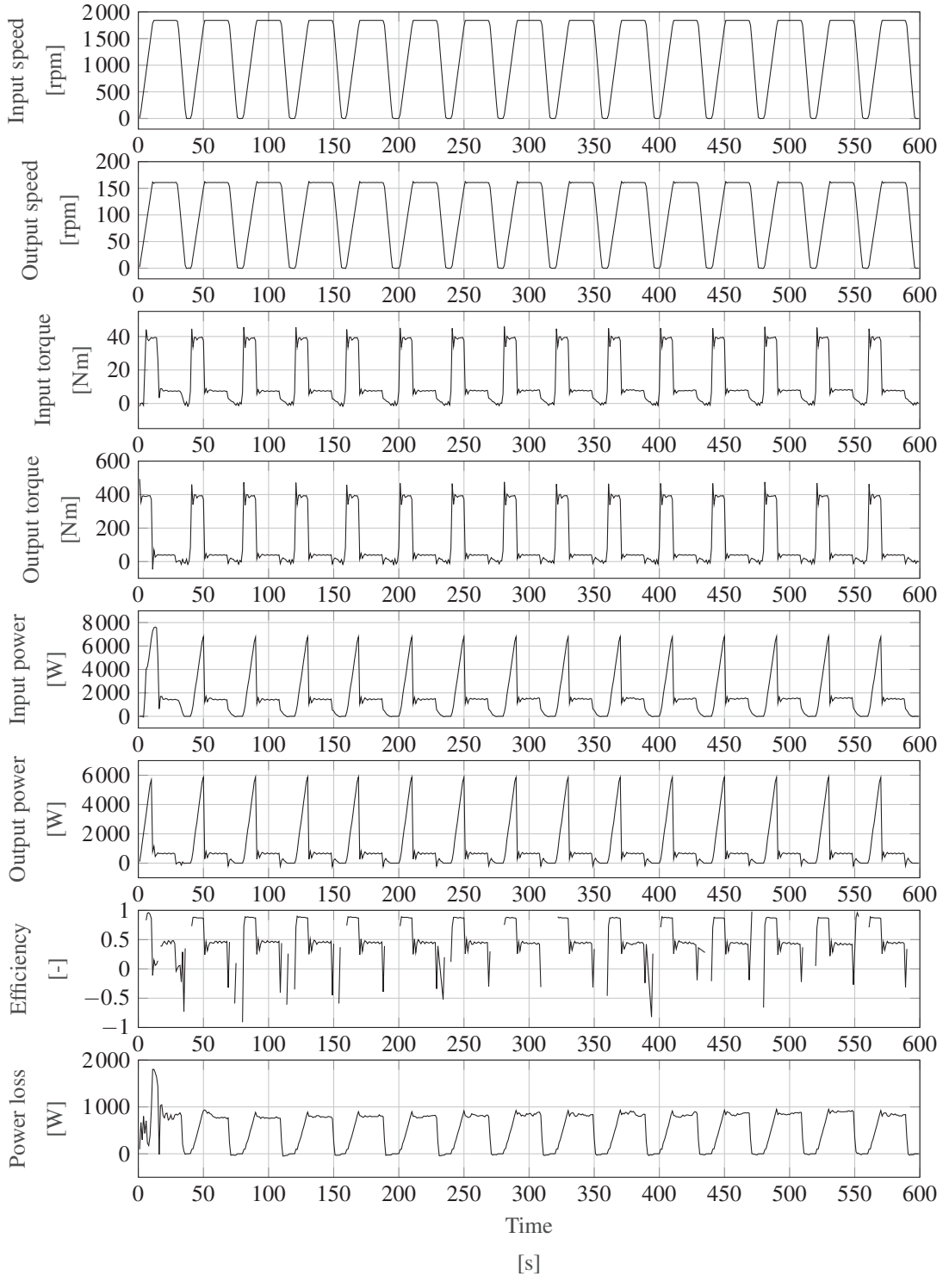

Fig. 8. *Input, output and calculated data for Central Business District (CBD) Segment of the Transit Coach Operating Duty Cycle*

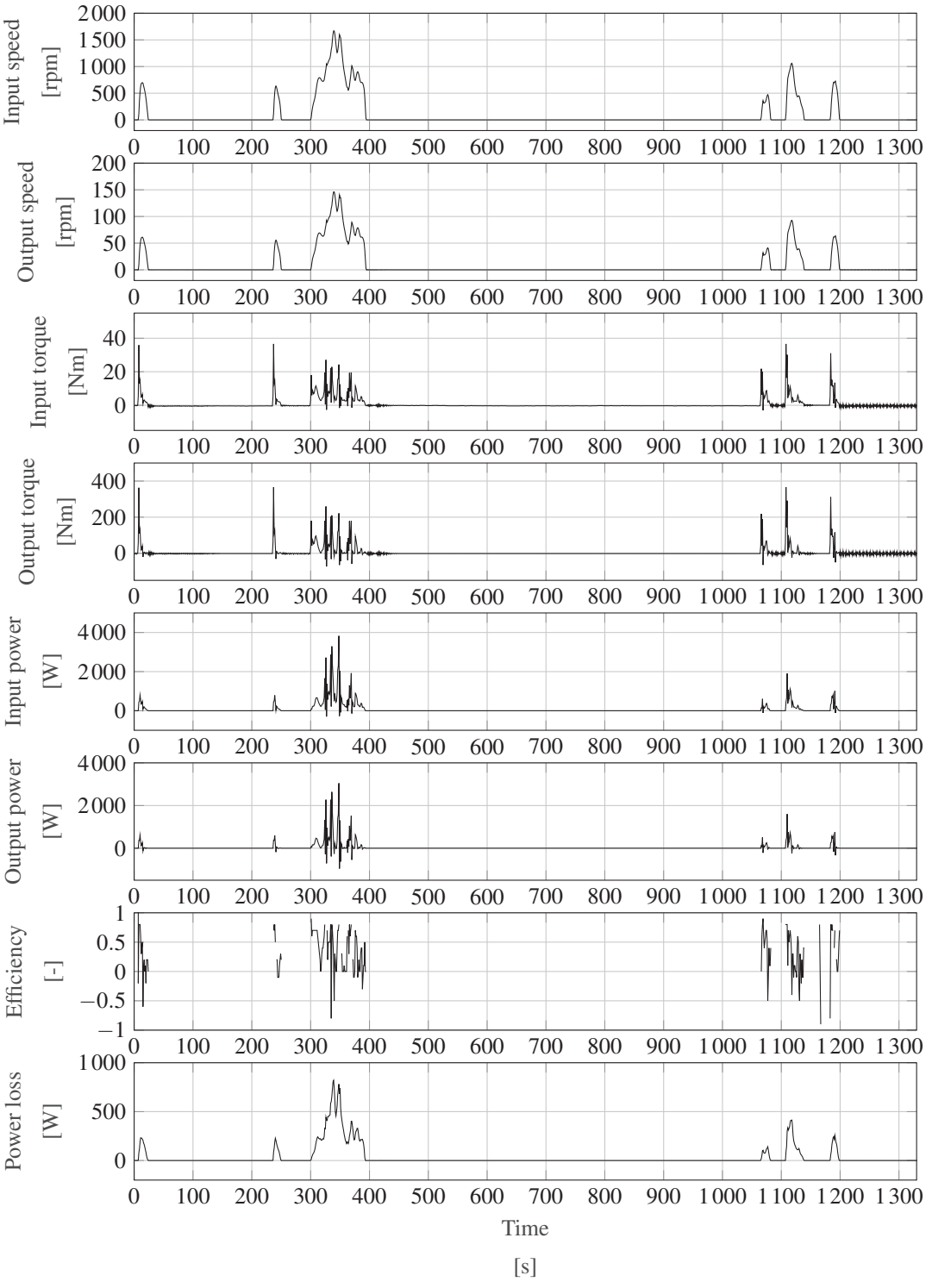

Fig. 9. *Input, output and calculated data for NREL Port Drayage Creep Queue Cycle (California)*

3 DISCUSSION

We presented a method for directly measuring the gearbox efficiency of an autonomous electric utility vehicle during driving cycles to obtain data on the effect of gearbox efficiency on the energy consumption of electric vehicles. Such data has a high potential for use in the future research and development of electric utility vehicle powertrains. Methods for measuring the overall efficiency of electric powertrains during driving cycles are already common, however, if we want to focus on research and development of separate optimisation of the efficiency of mechanical of powertrain, we should have an adequate understanding of the effect of the separate gearbox efficiencies.

To obtain data on the efficiency of the gearbox during driving cycles, we measured the efficiency of three driving cycles which simulated the driving operation of working utility vehicles using the described method. The method consists of measuring the mechanical power input to the gearbox and the mechanical power output of the gearbox during the driving cycle on a powertrain test bench.

The resulting values of achieved transmission efficiency during all measured driving cycles varied quite significantly depending on the input torque and input speed. At higher values of input torque, achieved transmission efficiencies of around 94 % could be observed from the measured data. However, in areas with lower input torque values, the achieved gearbox efficiencies were more around 60 %. These areas predominate in the measured driving cycles for the vehicle under consideration, and thus the gearbox was in areas of relatively low efficiency for the majority of the time. The achieved efficiency of around 60 % thus appears significantly low compared to the frequently reported gearbox efficiency values of 92 % to 97 % [7] sometimes reported in electric powertrain efficiency research articles. We explain such relatively low resulting gearbox efficiency values mainly for two reasons. The first reason is likely to be the characteristics and driving profiles of the driving cycles of the working vehicles used. For the assumed vehicle, the driving cycles represented relatively low load and therefore average gearbox input torque requirements on over the whole cycle. The gearbox was thus predominantly operated in areas of low input torque. The second reason may be the internal components of the gearbox are from a conventional gearbox Skoda Auto MQ200. It is likely that the gears in the gearbox are optimised predominantly for higher input torque at which the components may have the potential to achieve higher efficiencies. Both aspects can be indicated by the maximum efficiency values achieved during our measurements, with values above 90 % in areas with higher input torque values.

The low gearbox efficiency values achieved undoubtedly raise the question of the cause of such low values. We assume that detailed measurements of individual gearbox subsystems will be required to obtain an adequate answer. Nevertheless, it might still be feasible to estimate some approximation of the cause. The main sources of gearbox losses are generally oil churning, seal friction, gear mesh and bearing friction [13]. Generally, the losses can be split into two groups: load-dependent losses and load-independent losses [14]. Given the possible observation of significant changes in the achieved efficiency with changes in input torque, our results could suggest that some of the load-dependent losses are more likely to cause the relatively low gearbox efficiency achieved. Among the main sources of gearbox losses mentioned above, gear mesh and bearing friction could be considered.

From the resulting instantaneous power loss values, we conclude that the efficiency of electric vehicle gearbox can have a significant effect on the energy consumption results of electric powertrains measured during driving cycles. This is particularly the case in situations similar to the one we measured for the electric utility vehicle gearbox on drive cycles for specialized work vehicles, in which the vehicles moved at very low speeds with low loads.

By comparing the instantaneous gearbox efficiency curves of the individual driving cycles, it can be observed that the instantaneous efficiency measurements during driving cycles required frequent dynamic changes in input torque (in our case, CARB–HHDDTC S and NRELP DCQC cycles).

Consequently, the resulting gearbox efficiency data show oscillations and are challenging to evaluate adequately. In contrast, the results from the driving cycle CBDS oTCODC, which has a relatively straightforward speed and input torque profile, were relatively coherent and more beneficial.

4 CONCLUSIONS

We asked the question of how the efficiency of the gearbox could be directly measured during driving cycles and considered how gearbox efficiency affects the energy consumption of electric vehicles during these driving cycles. We investigated the effect of gearbox efficiency on the driving cycle through experimental measurements in a dedicated

powertrain laboratory using a gearbox designed for an autonomous electric utility vehicle.

In conclusion, the method of measuring gearbox efficiency on the driving cycles presented here provide an adequate basis for further research and development of electric vehicle gearboxes. Moreover, the resulting instantaneous gearbox efficiency values of driving cycles presented for specialized work vehicles, which can often be operated at low speeds with low loads, highlight the perhaps sometimes overlooked fact that in certain cases, it is the gearbox efficiency component which can have a significant effect on the overall efficiency of an electric powertrain, and as a consequence, on the energy consumption of electric vehicles. This method can be further developed with more detailed efficiency measurements based on input speed and input torque and parallel design modifications in the gearbox to maximize its efficiency during the driving cycles of specialized electric utility vehicles, with consequent results of lower energy consumption in real working operation.

5 ACKNOWLEDGEMENTS

This work was [partly] supported by the Student Grant Competition of the Technical University of Liberec under the project No. SGS-2019-6003

The result was obtained through the financial support of the Ministry of Education, Youth and Sports of the Czech Republic and the European Union (European Structural and Investment Funds - Operational Programme Research, Development and Education) in the frames of the project Modular platform for autonomous chassis of specialized electric vehicles for freight and equipment transportation, Reg. No.CZ.02.1.01/0.0/0.0/16_025/0007293

6 REFERENCES

[1] Laitinen, H., Lajunen, A., Tammi, K. (2017). Improving electric vehicle energy efficiency with two-speed gearbox. *IEEE Vehicle Power and Propulsion Conference (VPPC)*, p. 1-5, **DOI:10.1109/VPPC.2017.8330889**.

[2] Sayed, K., Kassem, A., Saleeb, H., Alghamdi, A.S., Abo-Khalil, A.G. (2020). Energy-saving of battery electric vehicle powertrain and efficiency improvement during different standard driving cycles. *Sustainability*, vol. 12, no. 24, art. ID 10466, **DOI:10.3390/su122410466**.

[3] McGuiness, P. (2008). Fuelling the car of the future. *Strojniški vestnik - Journal of Mechanical Engineering*, vol. 54, no. 5, p. 356-363.

[4] Thomas, J. (2014). Drive cycle powertrain efficiencies and trends derived from EPAvehicle dynamometer results. *SAE International Journal of Passenger Cars - Mechanical Systems*, vol. 7, no. 4, p. 1374-1384, **DOI:10.4271/2014-01-2562**.

[5] Davis, S.C., Diegel, S.W., Moore, S.A., Boundy, R.G. (2016). Vehicle Technologies Fact of the Week 2015, *Report No. ORNL/TM-2016/224*, **DOI:10.2172/1259430**.

[6] Albatayneh, A., Assaf, M.N., Alterman, D.,Jaradat, M. (2020). Comparison of the overall energy efficiency for internal combustion engine vehicles and electric vehicles. *Environmental and Climate Technologies*, vol. 24, no. 1, p. 669-680, **DOI:10.2478/rtuect-2020-0041**.

[7] Naunheimer, H., Bertsche, B., Ryborz, J. Novak, W. (2011). *Automotive Transmissions: Fundamentals, Selection, Design, and Application,* 2nd ed. Springer, Berlin, Heidelberg, **DOI:10.1007/978-3-642-16214-5**.

[8] Shen, Y., Rinderknecht, S., Hoppert, M. (2017). General modelling method of power losses in transmission with parameter identification. *Forschung im Ingenieurwesen*, vol. 81, p. 117-123, **DOI:10.1007/s10010-017-0241-1**.

[9] Ricardo IGNITE (2018). Ricardo Software 2018.1, *from www.software.ricardo.com*, accessed on 2021-07-14.

[10] DriveCAT: Drive Cycle Analysis Tool (2021). from *https://www.nrel.gov/transportation/drive-cycle-tool/index.html*, accessed on 2018-07-19.

[11] Zhen, F., Clark, N.N., Bedick, C.R., Gautam, M., Wayne, W.S., Thompson, G.J., Lyons, D.W. (2009). Development of a heavy heavy-duty diesel engine schedule for representative measurement of emissions. *Journal of the Air Waste Management Association*, vol. 59, no. 8, p. 950-959, **DOI:10.3155/1047-3289.59.8.950**.

[12] Biermann, J. (1999). Measurement system for cv joint efficiency. *SAE Technical Paper*, no. 1999-01-0936, **DOI:10.4271/1999-01-0936**.

[13] Zhang, W., Guo, X. (2014). Analysis and modeling of transmission efficiency of vehicle driveline. *SAE Technical Paper*, no. 2014-01-1779, **DOI:10.4271/2014-01-1779**.

[14] Achtenova, G., Pakosta, J. (2016). Estimation of the gearbox no-load losses. *SAE Technical Paper*, no. 2016-01-1092, **DOI:10.4271/2016-01-1092**.

Strojniški vestnik - Journal of Mechanical Engineering 68(2022)5, 314-324
DOI:10.5545/sv-jme.2021.7271
Original Scientific Paper
Received for review: 2021-05-29
Received revised form: 2022-01-10
Accepted for publication: 2022-03-08

Switch Semi-Active Control of the Floating Raft Vibration Isolation Sy tem

Zeyu Weng* – S hengli Liu – Teqi Xu – X iaoyu Wu – Z he Wang – J ie Tang
Zhejiang University of Technology, College of Mechanical Engineering, China

Switch semi-active control is introduced to improve the performance of the floating raft vibration isolation system on isolating vibration in the vicinity of the resonance frequency. A switch-controllable linear damper based on the electromagnetic damping principle is developed, whose characteristic parameters are obtained by experiment. The dynamic model of a semi-active control floating raft vibration isolation system is established, and two switch control algorithms are proposed. Algorithm 1 aims to minimize the kinetic energy of the raft, and Algorithm 2 balances minimizing the kinetic energy of the raft and minimizing the input energy of the system. The simulations of the original system, the system with the controllable damper, and the system with the damper controlled by the algorithms are carried out. The vibration acceleration responses of the foundation of the systems are used to evaluate the vibration isolation effect. The results show that the switching semi-active control using Algorithms 1 and 2 can significantly suppress the vibration of the system near the resonance frequency. Finally, the test platform of the switch's semi-active controlled floating raft vibration isolation system is built, and the simulation results are verified by the experimental result.

Keywords: floating raft, semi-active control, vibration isolation, switch algorithm

Highlights

- *Two semi-active control algorithms for floating raft vibration isolation systems are proposed.*
- *Applying these two semi-active control algorithms can improve the vibration isolation performance of the floating raft isolation system.*
- *Two algorithms have different effects at different external excitation frequencies.*

0 INTRODUCTION

As an extension of the double-layer vibration isolation system with multiple vibration sources, the floating raft vibration isolation system is widely used in the vibration isolation design of ship power units due to its good overall performance on vibration isolation [1]. However, the system has a poor isolation effect at low frequencies, especially near the system's resonance frequency, which may even amplify the vibration. Increasing the damping of the system is an effective method of suppressing resonance, and larger damping leads to a better suppression effect, but it affects the vibration isolation effect at middle and high frequencies. Using a switch-controllable damper and applying switch semi-active control technology on a floating raft vibration isolation system can effectively solve this problem.

The basic modes of vibration control include passive control, active control, and semi-active control. Compared with passive control, active control generally has a better effect and better adaptability [2] to [5]. However, it has higher requirements on the controllers and a limited effective control frequency band. Moreover, the stability and reliability of the system are difficult to guarantee. Once the vibration isolation system fails, the active control may amplify the vibration and even destroy the entire system. As a result, the active control technology cannot be widely used in engineering applications. Alternatively, semi-active control is used since it has a control effect close to that of active control, as well as advantages of lower energy consumption and better system stability and reliability. After failure, the system will degenerate into an ordinary floating raft vibration isolation system, which still isolates the vibration to some extent during the normal operation of the whole system.

Semi-active control on the vibration isolation system is essentially a kind of parameter control. According to the change of system input and the requirements of system output, the stiffness and damping of the system are adjusted by an appropriate control algorithm in real-time so that the vibration characteristics of the system can be improved. At present, semi-active control technology has been widely used in vehicle suspensions and seismic resistance of buildings [6] and [7]. For the floating raft vibration isolation system, Sun [8] studied the isolation performance of a semi-active dynamic vibration absorber in a floating raft system under multi-frequency excitation. Chen Dayue's team [9] and [10] studied the vibration isolation characteristics of the floating raft isolation system under fuzzy control

*Corr. Author's Address: Zhejiang University of Technology, Hangzhou, China, wengzy8888@163.com

and a synovial-film variable structure algorithm based on the ER damper. The results showed that different control algorithms could effectively improve the vibration isolation performance of the floating raft isolation system. The damper of the floating raft isolation system can be adjusted according to different requirements by using the methods of continuous semi-active control. This method has great potential. However, the adjustment range of the damper is only up to several times (generally no more than 10 times), and it is challenging to design an ideal control strategy due to the nonlinear damping characteristic; these factors limit its more comprehensive application. Switch semi-active control switches the state of a controllable damper on and off to improve the performance of vibration isolation. The control algorithm is simple and easy to operate, so the control system has high reliability. More importantly, the damping of the switch-controllable damper developed by our institute has strictly linear characteristics, the response time is down to milliseconds, and the damping can be adjusted up to tens of times. The experiments show that these characteristics and technical specifications are far superior to the existing dampers or controllable dampers that have been developed by some scholars, which guarantees the performance and reliability of semi-active control.

To summarize, it is of great significance to apply the switch semi-active control technology on the floating raft vibration isolation system with the self-developed switch-controllable damper. In this paper, we first characterize the damping properties of the developed controllable damper. Then, two switching-control algorithms are proposed to suppress the transmission of vibration from the unit to the foundation. Finally, using the acceleration response of the foundation as evaluation parameters, the effectiveness of the two algorithms is proved by simulation and experiment.

1 EXPERIMENTAL STUDY ON THE PERFORMANCE OF SWITCH-CONTROLLABLE LINEAR DAMPER

Properties characterizing the damping performance of the switch-controllable damper include the indicator, velocity, and response time, which is the key component to realize the semi-active control of the floating raft isolation system, and its performance determines the control effect. We independently developed the switch-controllable damper based on the electromagnetic damping principle. The control voltage is 24 V, direct current (DC). It has two states (on and off) corresponding to whether it is powered or not. When powered, the moving conductor and magnetic pole of the damper produce electromagnetic resistance and maintain a high damping value. Otherwise, it does not produce electromagnetic resistance, and the damper maintains a low damping value.

We carried out these tests on MTS849 Shock Absorber Test System (MTS Industrial Systems CO.LTD, USA) as shown in Fig. 1

Fig. 1. *MTS849 shock absorber performance test device used in the performance test*

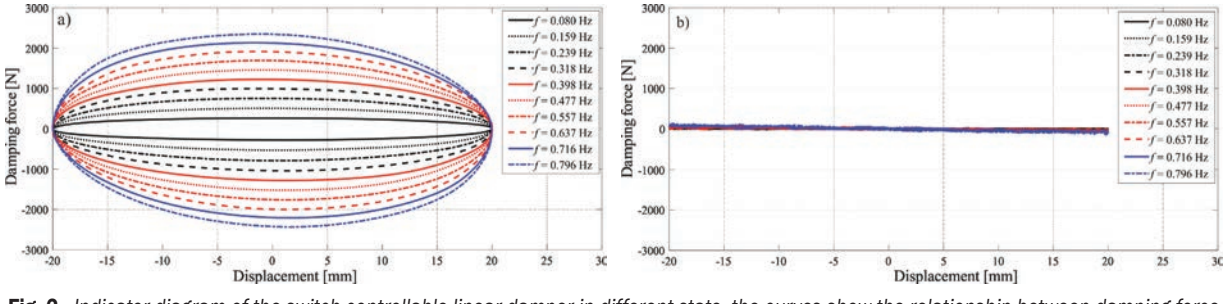

Fig. 2. *Indicator diagram of the switch-controllable linear damper in different state, the curves show the relationship between damping force and displacement, the f in the tag represents the frequency at which the damper operates; a) on state, and b) off state*

The indicator diagrams of the on and off states of controllable damper are shown in Fig. 2, where Fig 2a is for the on state and Fig. 2b is for off state. The curve family in Fig. 2 shows the relationship between the damping force generated by the damper and the motion displacement under different working frequencies. The curves in Fig. 2a are smooth, and the enclosed area is full, indicating that the damper can effectively absorb vibration energy when it is powered. The area enclosed by the curves in Fig. 2b is close to zero, indicating that the damper absorbs little vibration energy when it is not powered.

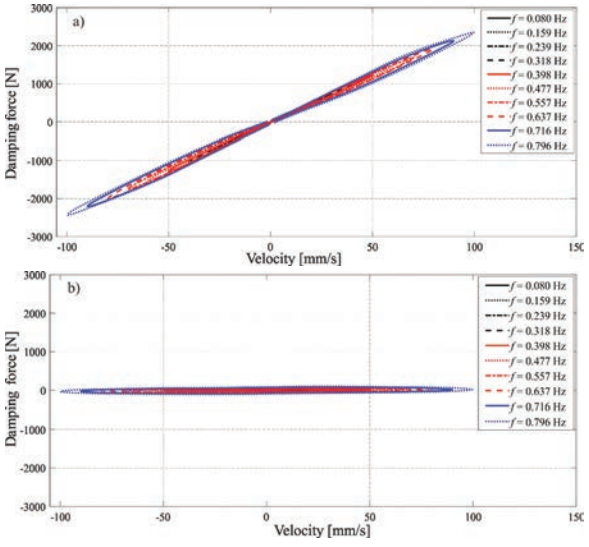

Fig. 3. *Velocity characteristic curve of the switching-controllable linear damper in different state, the curves show the relationship between damping force and velocity, the f in the tag represents the frequency at which the damper operates; a) on state, and b) off state*

The curves of the velocity characteristics of controllable damper are shown in Fig. 3, Fig. 3a is for the on state and Fig. 3b for off state. In Fig. 3, the curves show the relationship between the damping force generated by the damper and the motion velocity under different working frequency of the damper. The on state of the switch-controllable damper has great linear damping force velocity characteristics, meaning that the damper behaves as the pure viscous damper, and its damping coefficient is the slope of the curve. At the same time, the damping in the off state of the switch-controllable damper approaches a small constant.

It can be seen from the damper velocity characteristic curve that the damping characteristic of the controllable damper has obvious linear properties. We perform linear fitting on the speed characteristic data of the controllable damper in different states, and obtain that the damping coefficient of the controllable damper in the on state is 2405 N·m⁻¹·s, and the damping coefficient in the off state is 1050 N·m⁻¹·s.

In addition, the response time of the switch-controllable damper can be obtained by comparing the electrical signals controlling the damper and damping force output responses.

The characterizing parameters of the controllable damper obtained through the tests are shown in Table 1

Table 1. *Performance parameters of switch damper*

Parameter	Numerical value	
	On state	Off state
Damping coefficient [N·m⁻¹·s]	2.405×10^4	1050
Power consumption [W]	9.12	0
Response time [ms]	22	18
Working voltage DC [V]	24	
Quality [kg]	6.3	
Working distance [mm]	±32	

2 DYNAMIC MODEL

According to the magnitude of the foundation stiffness, two kinds of dynamic models of vibration isolation systems are commonly used: one with rigid foundation and the other with flexible foundation. In the analysis of the vibration isolation system, some scholars neglected the flexibility of the foundation and assumed infinite stiffness, thus established the rigid foundation model as shown in Fig. 4.

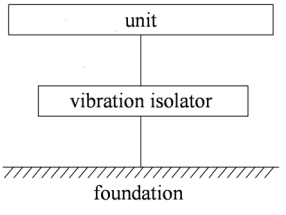

Fig. 4. *Simplified model of rigid foundation isolation system, here the stiffness of the foundation is assumed to be infinite*

However, from the research of Hamme [11] and Sykes [12], we know this simplification usually leads to some error. In addition, the vibration response on the foundation cannot be reflected in the model of rigid foundation, it is impossible to evaluate the isolation effect by foundation acceleration response. In conclusion, it is crucial to establish an analytical model of the floating raft isolation system with flexible foundation, as shown in Fig. 5

The semi-active controlled floating raft vibration isolation system consists of four parts: a unit, an elastic element, a controllable damper, a raft, and the foundation. As shown in Fig. 5 F represents the excitation force applied on the unit; m_1, m_2 and m_3 are the equivalent mass of the unit, raft and foundation respectively; c_1 and k_1 are the equivalent damping and stiffness between the unit and raft; c_2 and k_2 are the equivalent damping and stiffness between the raft and foundation; c_3 and k_3 and are the equivalent damping and stiffness of foundation; c_4 is the damping of the controllable damper, c_{on} is the high damping at on state while c_{off} is low damping at off state; x_1, x_2 and x_3 are the displacement responses of the unit, raft and foundation respectively, v_1, v_2 and v_3 are the velocity responses, a_1, a_2 and a_3 are the acceleration responses.

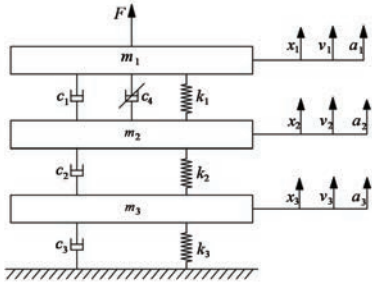

Fig. 5. *Dynamic model of semi-active control floating raft isolation system*

The dynamical equation corresponding to the model can be expressed as Eq. (1).

$$\begin{bmatrix} m_1 & 0 & 0 \\ 0 & m_2 & 0 \\ 0 & 0 & m_3 \end{bmatrix} \begin{bmatrix} a_1 \\ a_2 \\ a_3 \end{bmatrix} + \begin{bmatrix} c_1 + c_4 & -c_1 & 0 \\ -c_1 - c_4 & c_2 & -c_2 \\ 0 & -c_2 & c_3 \end{bmatrix} \begin{bmatrix} v_1 \\ v_2 \\ v_3 \end{bmatrix} + \begin{bmatrix} k_1 & -k_1 & 0 \\ -k_1 & k_1 + k_2 & -k_2 \\ 0 & -k_2 & k_2 + k_3 \end{bmatrix} \begin{bmatrix} x_1 \\ x_2 \\ x_3 \end{bmatrix} = \begin{bmatrix} F \\ 0 \\ 0 \end{bmatrix}, \quad (1)$$

which shows that the damping matrix of the system can be changed by adjusting the damping of the controllable damper c_4, thus makes effect on the vibration response of the floating raft vibration isolation system.

3 ALGORITHMS

To realize switch semi-active control of the floating raft vibration isolation system and improve its effect, two switch control algorithms named Algorithms 1 and 2 are proposed in this paper.

3.1 Algorithm 1

The goal of Algorithm 1 is to minimize the kinetic energy transmitted to the raft by adjusting the elastic energy absorbed or released by the elastic element.

The vibrational energy transited to the system by the excitation force transforms into the kinetic energy of the mass element, the potential energy of the elastic element, and the energy consumed by the damping element. The damping element consumes the energy, while the kinetic energy of the mass element and the potential energy of the elastic element are transformed mutually. More specifically, the vibration energy transmitted to the system is simultaneously converted into the kinetic energy of unit, the potential energy of the elastic element between unit and raft, the energy consumed by the damping element between unit and raft, and the kinetic energy of raft. Among them, the increase of kinetic energy of raft leads to the increase of the energy transmitted to the foundation, which exacerbates the vibration of the foundation. The kinetic energy of the raft can be reduced as much as possible by controlling the damping force. When the elastic element absorbs energy, the controllable damper is switched to the off state to minimize the damping value, which makes the elastic element absorb more energy and thus reduces the energy transited to the raft. When the elastic element releases energy, the controllable damper is switched to the on state to maximize the damping value, which makes the damper consume more energy and thus reduces the energy released from the spring to the raft.

According to the displacement and velocity differences between the unit and raft, the motion of the floating raft vibration isolation system can be divided into four states as shown in Fig. 6 where dotted lines are the equilibrium positions of the unit and raft.

In Fig. 6a, the displacement difference between the unit and raft is positive ($x_1 - x_2 > 0$), which means the spring element between unit and raft is elastically restored; the velocity difference is positive ($v_1 - v_2 > 0$), which means the displacement difference between the two will increase. In this state, the elastic element absorbs energy and the controllable damper should be in the off state.

In Fig. 6b, the displacement difference between the unit and the raft is positive ($x_1 - x_2 > 0$), which means the spring element between the unit and raft is elastically restored; the velocity difference is negative ($v_1 - v_2 < 0$), which means the displacement difference between the two will decrease. In this state, the elastic element releases energy and the controllable damper should be in the on state.

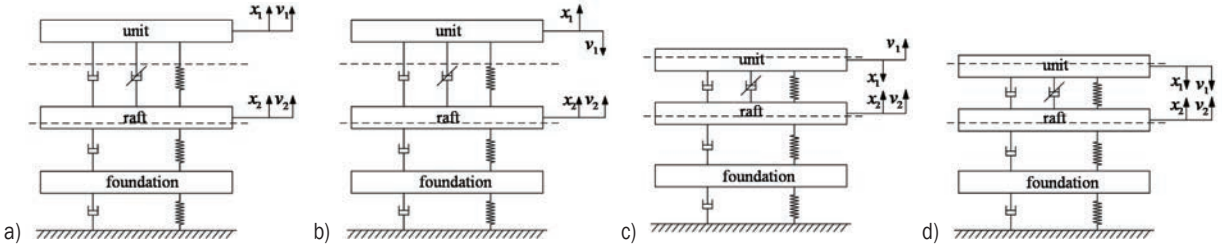

Fig. 6. *System state decided by the displacement difference and velocity difference; a), b), c) and d) are explained in the article*

In Fig. 6 , the displacement difference between the unit and the raft is negative ($x_1 - x_2 < 0$), which means the spring element between unit and raft is compressed; the velocity difference is positive ($v_1 - v_2 > 0$), which means the displacement difference between the two will increase. In this state, the elastic element releases energy and the controllable damper should be in the on state.

In Fig. 6, the displacement difference between the unit and the raft is negative ($x_1 - x_2 < 0$), which means the spring element between unit and raft is compressed; the velocity difference is negative ($v_1 - v_2 < 0$), which means the displacement difference between the two will decrease. In this state, the elastic element absorbs energy and the controllable damper should be in the off state.

Based on the analysis of each state above, the control law of Algorithm 1 can be expressed as

$$c_4 = \begin{cases} c_{off} & (x_1 - x_2) > 0, (v_1 - v_2) > 0 \\ c_{on} & (x_1 - x_2) > 0, (v_1 - v_2) < 0 \\ c_{on} & (x_1 - x_2) < 0, (v_1 - v_2) < 0 \\ c_{off} & (x_1 - x_2) < 0, (v_1 - v_2) > 0 \end{cases} P_F = F \cdot v_1, \quad (2)$$

which can be simplified as

$$c_4 = \begin{cases} c_{off} & (x_1 - x_2) \cdot (v_1 - v_2) \geq 0 \\ c_{on} & (x_1 - x_2) \cdot (v_1 - v_2) < 0 \end{cases}. \quad (3)$$

3.2 Algorithm 2

Algorithm 2 aims to makes the balance on minimizing the input energy of the system and minimizing the kinetic energy of the raft.

The power of the excitation force on the unit can be expressed as

$$P_F = F \cdot v_1, \quad (4)$$

the controllable damping force also works on the unit and its power can be expressed as

$$P_{c1} = c_4 \cdot (v_2 - v_1) \cdot v_1. \quad (5)$$

If both P_F and P_{c1} are positive, then

$$P_F \cdot P_{c1} = F \cdot c_4 \cdot (v_2 - v_1) \cdot v_1^2 \geq 0, \quad (6)$$

that is

$$F \cdot (v_2 - v_1) \geq 0. \quad (7)$$

The excitation force inputs energy to the system and the controllable damping force will exacerbate this input, the controllable damper should be in the off state to reduce the input energy. If P_F is positive while P_{c1} is negative then

$$F \cdot c_4 \cdot (v_2 - v_1) < 0, \quad (8)$$

that is

$$F \cdot (v_2 - v_1) < 0. \quad (9)$$

The excitation force inputs energy to the system and the controllable damping force will attenuate this input, so the controllable damper should be in the on state to reduce the input energy. If P_F is negative while P_{c1} is positive then

$$F \cdot c_4 \cdot (v_2 - v_1) < 0, \quad (10)$$

that is

$$F \cdot (v_2 - v_1) < 0. \quad (11)$$

The excitation force absorbs energy from the system and the controllable damping force will enhance the absorption, so the controllable damper should be in the on state to increase the energy absorption. If both P_F and P_{c1} are negative then

$$F \cdot c_4 \cdot (v_2 - v_1) \geq 0, \quad (12)$$

that is

$$F \cdot (v_2 - v_1) \geq 0. \quad (13)$$

The excitation force absorbs energy from the system and the controllable damping force will attenuate the absorption, so the controllable damper

should be in the off state to increase the energy absorption.

In short, when the excitation force and the controllable damping force are in the same direction, the controllable damper should be in a low damping state; while in the opposite direction, the controllable damper should be in a high damping state. The damping expression of the controllable damper is

$$c_4 = \begin{cases} c_{off} & F \cdot (v_2 - v_1) \geq 0 \\ c_{on} & F \cdot (v_2 - v_1) < 0 \end{cases}. \quad (4)$$

Both Algorithm 1 and Eq. (4) give the expressions of the controllable dampers, which are incompatible. Algorithm 2 combines Algorithm 1 with Eq. (4) . That is: if the control results of Algorithm 1 and Eq. (4) are consistent, then take the common result as the criterion and set the state of the controllable damper accordingly. Otherwise, the controllable damper is set to the active mode to consume more energy. In conclusion, the control law of Algorithm 2 can be expressed as

$$c_4 = \begin{cases} c_{off} & F \cdot (v_2 - v_1) \geq 0, (x_1 - x_2) \cdot (v_1 - v_2) \geq 0 \\ c_{on} & F \cdot (v_2 - v_1) < 0, (x_1 - x_2) \cdot (v_1 - v_2) < 0 \\ c_{on} & F \cdot (v_2 - v_1) \geq 0, (x_1 - x_2) \cdot (v_1 - v_2) < 0 \\ c_{off} & F \cdot (v_2 - v_1) < 0, (x_1 - x_2) \cdot (v_1 - v_2) \geq 0 \end{cases}, \quad (5)$$

which can be simplified as

$$c_4 = \begin{cases} c_{off} & F \cdot (v_2 - v_1) \geq 0 \bigcap (x_1 - x_2) \cdot (v_1 - v_2) \geq 0 \\ c_{on} & F \cdot (v_2 - v_1) < 0 \bigcup (x_1 - x_2) \cdot (v_1 - v_2) < 0 \end{cases}. \quad (6)$$

These two algorithms have different emphasis and both have its own advantages and disadvantages. Algorithm 1 only considers the energy changes of the elastic elements and damping elements between raft and unit, but doesn't take the change of the system total energy into account. Algorithm 2 concerns not only the absorption, release, and consumption of local energy, but also considers the change of the total energy of the system.

4 SIMULATIONS AND ANALYSES

To verify the switch semi-active control algorithms, we simulated the floating raft vibration isolation system in MATLAB Simulink as shown in Fig. 7 and applied the control algorithms.

For comparison, the acceleration response of the foundation without control (including the off-state and the on state system) is also studied both in time domain and frequency domain analysis. The simulation parameters of the model are shown in Table 2, which is determined by the floating raft vibration isolation system used for tests.

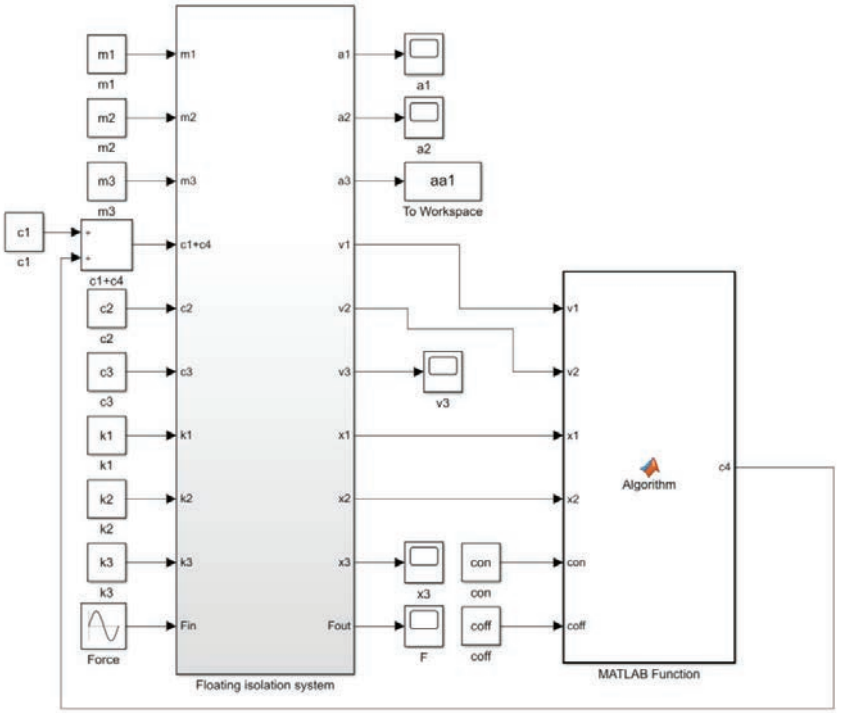

Fig. 7. *Simulink model of the semi-active controlled floating raft isolation system*

Table 2. *Model parameters for semi-active controlled floating raft isolation system*

Parameters		Value
Equivalent mass [kg]	m_1	238.8
	m_2	175.1
	m_3	216
Equivalent damping [N·m^{-1}·s]	c_1	70
	c_2	50
	c_3	5000
Controllable damper [N·m^{-1}·s]	c_{off}	2100
	c_{on}	4.81×10^4
Equivalent stiffness [N·m^{-1}]	k_1	3.707×10^5
	k_2	3.468×10^5
	k_3	2.809×10^7

4.1 Time Domain Comparison of Foundation Responses

The amplitude of the excitation force acting on the unit in the simulation model is determined to be 60 N referring to the magnitude of the excitation force in the test device used in this study, and its frequency range is from 0.1 Hz to 20 Hz. As shown in Fig. 8, four typical frequencies were selected from the simulation results for analysis.

The first frequency (3.9 Hz) is the first resonance frequency of the non-controlled system. Fig. 8a shows that under the harmonic excitation of 3.9 Hz, the foundations of the systems controlled by Algorithms 1 and 2 both have acceleration response amplitudes distinctly lower than that of the off-state system, higher than that of the on-state system and that from Algorithm 2 is even lower than Algorithm 1. These indicate that the vibration isolation effect of Algorithms 1 and 2 is obviously superior to that of the off-state system and is worse than that of the off-state system. The effect of Algorithm 2 is better than Algorithm 1 at this frequency.

The second frequency (4.7 Hz) is the frequency near the first resonance frequency under the control of the algorithms. Fig. 8b shows that under the harmonic excitation of 4.7 Hz, the foundations of the systems controlled by Algorithms 1 and 2 both have acceleration response amplitudes distinctly higher than that of the off-state system. These indicate that the isolation effect of the off-state system is superior to the Algorithms 1 and 2 at this frequency.

The third frequency (6.0 Hz) is the frequency where the effect with and without control are close. Fig. 8c shows that, under the harmonic excitation of 6 Hz, the foundations of the systems controlled by Algorithms 1 and 2 both have acceleration response amplitudes close to non-controlled system. These indicate that the isolation effect of non-control, Algorithms 1 and 2 is approximately equivalent at this frequency.

The last frequency (11 Hz) is the second resonance frequency of the non-controlled system. Fig. 8d shows that, under the harmonic excitation of

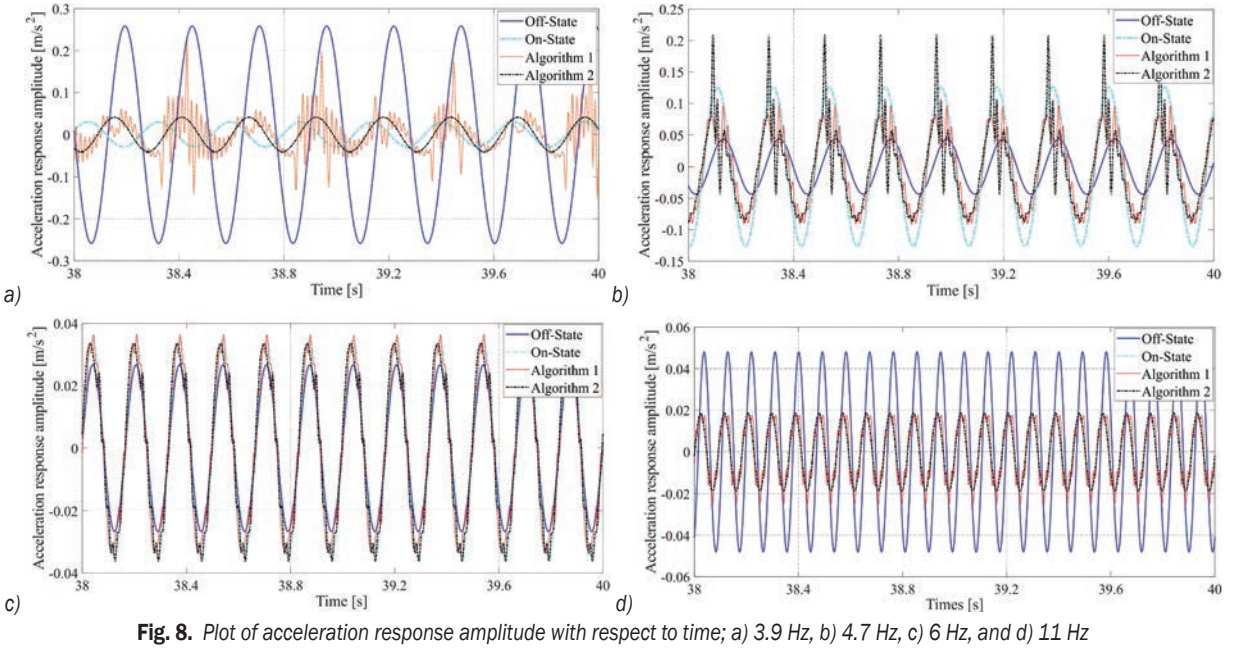

Fig. 8. *Plot of acceleration response amplitude with respect to time; a) 3.9 Hz, b) 4.7 Hz, c) 6 Hz, and d) 11 Hz*

11 Hz, the foundations of the systems controlled by Algorithms 1 and 2 both have acceleration response amplitudes distinctly lower than that of the off-state system. These indicate that the isolation effect of the off-state system is inferior to Algorithms 1 and 2; and there is little difference between the results of the on-state system, Algorithms 1 and 2, which suggest that the Algorithm 1 is basically in line with Algorithm 2 at this frequency.

4.2 Frequency Domain Comparison of Foundation Responses

For the goal of comparison with the original system which has no switch-controllable damper, we carried out the frequency domain analysis of this case in additional. Continuously changing the frequency of the excitation force on the system and recording the foundation's acceleration response yields the variation curve of the acceleration response amplitude on the foundation of the system in the excitation frequency range from 0.1 Hz to 20 Hz, as shown in Fig. 9. There are two obvious resonance peaks in the response amplitude curve of the foundation acceleration of the original system.

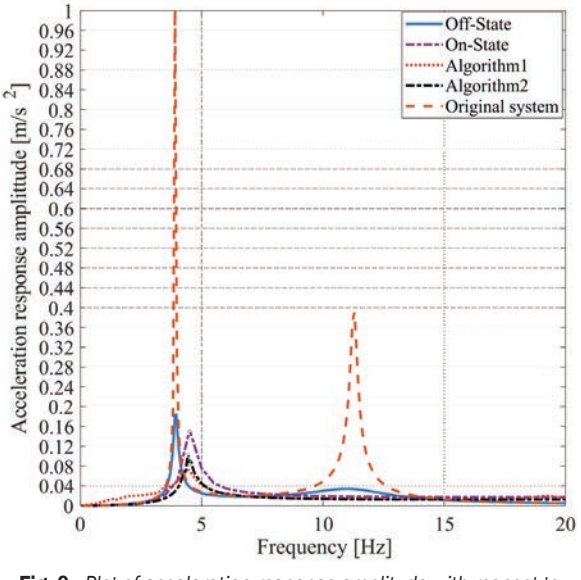

Fig. 9. *Plot of acceleration response amplitude with respect to frequency obtained by simulation*

According to Fig. 9, it can be seen that the trends of acceleration responses of the foundation of the four cases are basically similar, all of which reach the maximum at the resonance frequency. It is obvious that the acceleration response amplitude of the foundation of the original system is greatly reduced after the installation of controllable damper. Comparing between systems using the controllable damper, the amplitudes of acceleration response on the foundation of the systems using two algorithms are significantly smaller than that of non-controlled system around the resonance frequency. Before reaching to the resonance frequency, the vibration isolation effect of Algorithm 1 is the worst while Algorithm 2 is the best; after the resonant frequency, the effect of these two algorithms are close to that of the non-controlled system. Compared with Algorithm 2, Algorithm 1 performs better around the resonance frequency but is inferior to Algorithm 2 in the low frequency band; in the following frequency band, the performance of two algorithms is approximately the same.

From the amplitude value of the foundation's acceleration response curve, the maximum values of the original system, the off-state system, the on-state system and the system using Algorithms 1 and 2 are shown in Table 3. The amplitude of the Original system is much larger and thus the vibration isolation effect is poorer; and the vibration isolation effect gets better when the controllable damper is used. Compared with non-controlled system, the amplitude of the system using Algorithm 1 is reduced by 80.4 %, and using Algorithm 2 is reduced by 43.3 %; the amplitude using Algorithm 1 is reduced by 30.1 % compared with that using Algorithm 2.

Table 3. *Acceleration response maximum of five states (simulation)*

State	Maximum [m/s²]
Original system	1.012
Off-State	0.1844
On-State	0.1526
Algorithm 1	0.07296
Algorithm 2	0.1045

It can be concluded that using controllable damper can improve the isolation effect of the floating raft isolation system in the low frequency segment; furthermore, using the algorithms to control the controllable damper can further improve the vibration isolation effect.

5 EXPERIMENTS

5.1 Test System and Scheme

We built the experiment setup for the semi-active controlled floating raft vibration isolation system, which consists of a floating raft vibration test bench, a

switch-controller system, and a test evaluation system. The block diagram is shown in Fig. 10.

The floating raft vibration test bench is composed of a unit, a variable-frequency drive (VFD), upper isolation springs, a raft, lower isolation springs, foundation, and controllable dampers. The switch-controller system is composed of acceleration sensors, conditioning amplifier, PCI DAQ, Industrial Personal Computer (IPC) and a relay. The velocities and displacements needed in the algorithms can be

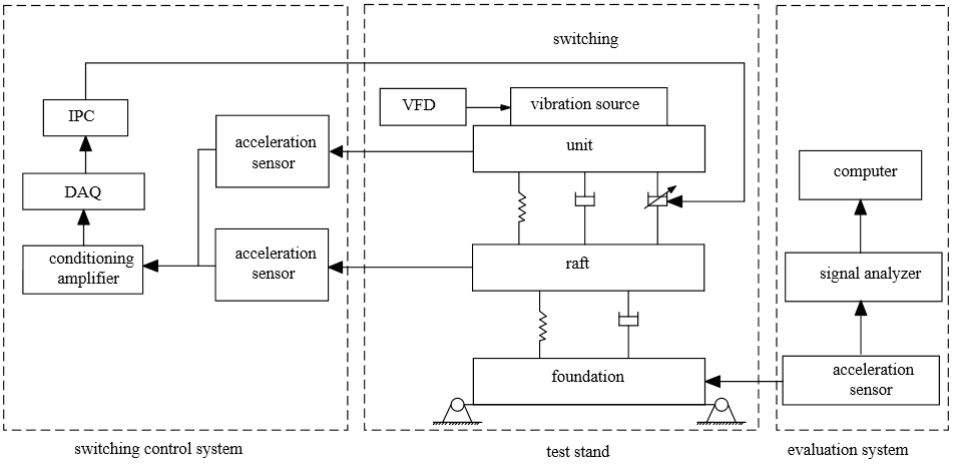

Fig.10. *Test block diagram of semi-active control of floating raft isolation system*

obtained from integration. The test evaluation system has composed of 3B 0 acceleration sensors (PCB Piezotronics, Inc., USA) and a Siglab20-42 signal analyser (Spectral Dynamic, Inc., USA), Siglab analysis software is installed on the computer.

The variable-frequency drive controls the excitation force on the unit to generate harmonic excitation at different frequencies. The switch semi-active control algorithms are implemented by running the control program of LabVIEW. It switches the controllable damper by controlling the relay. The test evaluation system collects the acceleration response signals on the foundation for analysis. This setup of the experiment is shown in Fig. 11

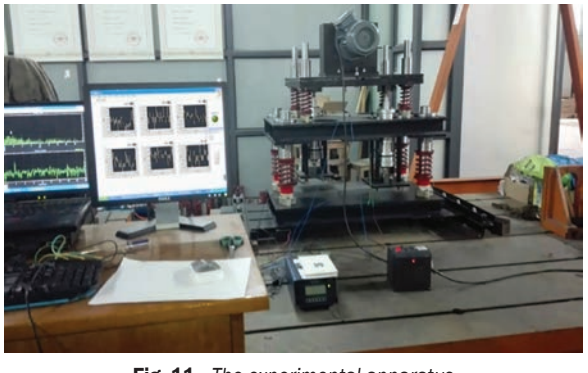

Fig. 11. *The experimental apparatus*

5.2 Results and Analysis

We tested the original system, the non-controlled system (the On-State or Off-State system), and the semi-active switch-controlled systems using Algorithms 1 and 2, respectively, from which the variation curves of the acceleration response amplitudes of the foundations at the excitation frequency range from 15 Hz to 3 Hz are obtained, as shown in Fig. 12.

From the amplitude value of the foundation's acceleration response curve, the maximum values of the original system, Off-state system, On-state system, Algorithms 1 and 2 are obtained and shown in Table 4. The vibration isolation effect of the original system is not obvious. Acceleration response amplitudes of the original system, the off-state system, the on-state system, the semi-active switch-controlled systems using Algorithms 1 and 2, respectively, are 0.03 0.0224,30.8660.01 27a nd 0.031

Comparing Figs. 9 and 12, it can be seen that the simulation results are in good agreement with the experimental results. Around the resonance frequency, the vibration isolation effect of semi-active control using Algorithms 1 and 2 is clearly better than that of non-controlled system, and they are roughly the same at other frequencies, which shows that Algorithms 1 and 2 can effectively improve the vibration isolation

performance of floating raft system around the resonance frequency.

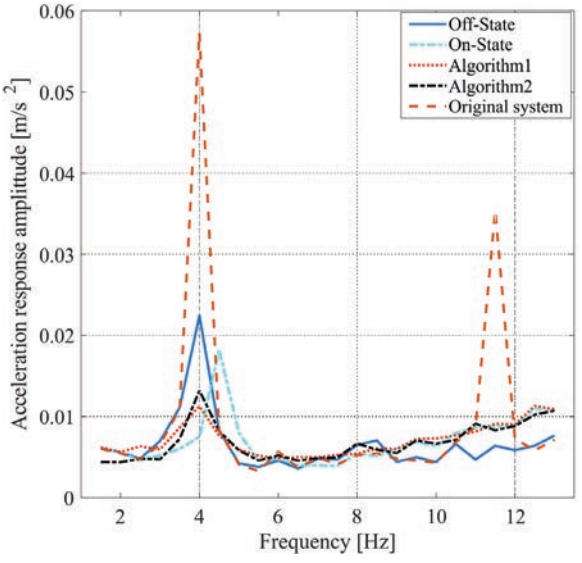

Fig. 12. *Plot of acceleration response amplitude with respect to frequency obtained by experiment test*

Table 4. *Acceleration response maximum of three states (test)*

State	Maximum [m/s²]
Original system	0.0573
Off-State	0.02243
On-State	0.01826
Algorithm 1	0.01127
Algorithm 2	0.01321

It is worth mentioning that there are some discrepancies in the magnitude of the underlying acceleration between simulation and testing.

(a) Compared with the simulation results, the basic acceleration amplitude of the test generally increases gradually with the increase of the frequency. The reason for this is that the test system adopts an inertial rotation excitation device, and the amplitude of the excitation force gradually increases with the increase of the frequency (i.e., the rotation speed), while the constant amplitude excitation force is used in the simulation model.

(b) In the test results, the frequencies corresponding to the first-order peaks are basically the same except for the open state of the damper. In the open state of the damper, the frequency increases slightly. In the simulation results, however, the frequency increases in the on state and two control algorithm states compared to the off and original system states. The main reason for this discrepancy is that the properties and values of all damping of the actual floating raft vibration isolation system are very complex, and the damping force can be understood as the superposition of damping forces of various properties. In the simulation model, only the viscous damping of the system is considered, which makes the damping in the simulation model relatively small. The main influencing factor of the frequency corresponding to the first-order peak is the system damping (c_1+c_4). When (c_1+c_4) is larger, the frequency corresponding to the first-order peak is also larger. Since the parameter c_1 in the test system is larger than the parameter in the simulation model, in the vicinity of the first-order peak frequency, after the algorithm is applied to the test system, the larger c_1 makes c_4 do not need to be turned on frequently, and the switch damper c_4 is in the off state as the dominant factor. The damping (c_1+c_4) in the test system is more in a less damped state and the frequency corresponding to the first-order peak barely increases. After the simulation model applies the algorithm, the smaller c_1 makes c_4 need to be turned on frequently, and the switch damper c_4 is in the on state as the dominant factor. The damping (c_1+c_4) in the simulation model is more in the larger damping state and the frequency corresponding to the order peak increases slightly.

In addition, we only consider the viscous damping of the floating raft system in the simulation model and the amplitude of the second peak in the simulation results decreases as the damping increases. In the actual test system, when the controllable damper is in the off state, the characteristics of damping (c_1+c_4) mainly depend on c_1, and the non-viscous damping characteristics become obvious, which leads to the discrepancies between the experimental results (the amplitude of the second peak is small) and the simulation results.

6 CONCLUSIONS

To solve the problem that the vibration isolation effect of the floating raft vibration isolation system is poor near the resonance frequency and even has a vibration amplification effect, we developed a switch-controllable damper and introduced semi-active switch control technology. Two switch control algorithms, Algorithms 1 and 2, are proposed. Based on the simulation and experiments, the following conclusions can be drawn:

(1) The controllable damper can improve the isolation effect of the vibration isolation system near the resonance frequency. Built on that, the vibration isolation effect of the system can be further greatly improved by using the proposed semi-control algorithms.
(2) The two control algorithms have their own advantages and disadvantages. In the low frequency band, the overall isolation effect of Algorithm 2 is better than that of Algorithm 1 However, near resonance frequency, using Algorithm 1 in the vibration isolation effect is more superior near the resonance frequency.
(3) Future work on this can be carried out in the direction of multi-frequency excitation, which is closer to the practical engineering application.

7 REFERENCES

[1] He, L., Xu, W. (2013). Naval vessel machinery mounting technology and its recent advances. *Acta Acustica*, vol. 38, no. 2, p. 128-136, **DOI:10.15949/j.cnki.0371-0025.2013.02.001**. (in Chinese)

[2] Niu, J., Song, K., Lim, C.W. (2005). On active vibration isolation of floating raft system. *Journal of Sound and Vibration*, vol. 285, no. 1-2, p. 391-406, **DOI:10.1016/j.jsv.2004.08.013**.

[3] Wang, Z., Mak, C.M. (2018). Application of a movable active vibration control system on a floating raft. *Journal of Sound and Vibration*, vol. 414, p. 233-244, **DOI:10.1016/j.jsv.2017.11.026**.

[4] Fuller, C.R., Elliott, S.J., Nelson, P.A. (1997). Active control of vibration. *Physics Today*, vol. 50, no. 5, p. 64, **DOI:10.1063/1.881838**.

[5] Liu, Y., Shu, Y., Hu, W., Zhao, X., Xu, Z. (2021). Active vibration control of a mechanical servo high-speed fine-blanking press. *Strojniški vestnik - Journal of Mechanical Engineering*, vol. 67, no. 9, p. 445-457, **DOI:10.5545/sv-jme.2020.6959**.

[6] Ghiringhelli, G.L. (2000). Testing of semiactive landing gear control for a general aviation aircraft. *Journal of Aircraft*, vol. 37, no. 4, p. 606-616, **DOI:10.2514/2.2672**.

[7] Jung, H.-J., Park, K.-S., Spencer, B.F.Jr, Lee, I.-W. (2010). Hybrid seismic protection of cable-stayed bridges. *Earthquake Engineering & Structural Dynamic*s, vol. 33, no. 7, p. 795-820, **DOI:10.1002/eqe.374**.

[8] Sun, H.L., Zhang, K., Zhang, P.Q., Chen, H.B. (2010). Application of dynamic vibration absorbers in floating raft system. *Applied Acoustic*s, vol. 71, no. 3, p. 250-257, **DOI:10.1016/j.apacoust.2009.09.005**.

[9] Gao, X., Fan, G., Jin, C., Dong, G. (2016). Double-layer vibration suppression bilinear system featuring electro-rheological damper with optimal damping and semi-active control. *Journal of Vibroengineering*, vol. 18, no. 6, p. 3891-3914, **DOI:10.21595/jve.2016.16577**.

[10] Zhao, C., Chen, D. (2008). A two-stage floating raft isolation system featuring electrorheological damper with semi-active fuzzy sliding mode control. *Journal of Intelligent Material Systems and Structure*s, vol. 19, no. 9, p. 1041-1051, **DOI:10.1177/1045389X07083141**.

[11] Hamme, R.N. (1956). Acoustical materials problems posed by low-frequency sound control. *Noise Control*, vol. 2, no. 5, p. 10, **DOI:10.1121/1.2369224**.

[12] Sykes, A.O. (1960). Isolation of vibration when machine and foundation are resilient and when wave effects occur in the mount. *Noise Control*, vol. 6, p. 23-38, **DOI:10.1121/1.2369414**.

Strojniški vestnik - Journal of Mechanical Engineering 68(2022)5, 325-338
DOI:10.5545/sv-jme.2022.59
Original Scientific Paper
Received for review: 2022-02-09
Received revised form: 2022-03-10
Accepted for publication: 2022-04-13

Effect of Vibration and Noise Measuring Points Distribution on the Sensitivity of Pump Cavitation Diagnosis

Runze Zhou[1*] – Hui Chen[2, 3] – Liang Dong[4] – Houlin Liu[4] – Zeyu Chen[1] – Yuhang Zhang[1] – Zhiming Cheng[1]

[1] Jiangsu University, Research Center of Fluid Machinery Engineering and Technology, China
[2] Science and Technology Laboratory on Liquid Rocket Engine, China
[3] Xi'an Aerospace Propulsion Institute, China
[4] Jiangsu University, National Research Center of Pumps, China

Cavitation is an essential factor in the deterioration of the hydraulic performance of centrifugal pumps. The study of cavitation fault diagnosis can help prevent or reduce the damage it causes. The vibration and noise analysis method can predict the incipient cavitation more accurately. In order to improve the accuracy of cavitation fault diagnosis, this paper studied the sensitivity of measuring points distribution for centrifugal pump cavitation diagnosis. The research object is a centrifugal pump with an inducer and splitter blades. Vibration acceleration sensors and hydrophones were used to collect structural vibration and liquid-borne noise signals at different positions of the pump unit. Root-mean-square (RMS) and fast Fourier transform (FFT) methods were used to construct spectrums of vibration and noise signals with different NPSHa and compare the sensitivity of different measuring points to the inception and development of cavitation. In addition, the SST k-ω turbulence model and Zwart cavitation model were used to study the cavitation volume distribution in the pump under different cavitation stages. By setting monitoring points at the impeller outlet, the frequency domain signal distribution of pressure pulsation was studied. The results show that the vibration measuring points at the inlet flange and pump axial position (increased by about 0.6 % at NPSHr) and liquid-borne noise measuring point at the inlet position (reduced by about 14 % at NPSHr) are more sensitive to the diagnosis of cavitation fault. Motor current is also the basis for judging the inception of cavitation. When severe cavitation occurs, the current drops sharply by approximately 12 %. Moreover, the pressure pulsation intensity at the inlet decreases by 66.3 % and by increases 13.9 % at the outlet, respectively, with a 3 % drop in head. As the cavitation intensifies, the dominant frequency of the pressure pulsation in the pump is partially shifted. The presented results indicate the distribution of measuring points with good sensitivity, providing a reference for improving the accuracy and efficiency of cavitation predictions for centrifugal pumps.

Keywords: cavitation diagnosis, centrifugal pump, vibration and noise, sensitivity of measuring points, spectral analysis

Highlights

- *The spectral characteristics of centrifugal pump vibration and noise with the development of cavitation were revealed.*
- *The variations of pressure pulsation RMS and frequency domain with NPSHa were studied.*
- *The sensitivities of the cavitation diagnosis methods were verified, and the optimal measuring point layout scheme was proposed.*
- *The relationship between vapour volume evolution and noise frequency features was studied.*

0 INTRODUCTION

Cavitation affects the operational stability and efficiency of the pump and is an essential indicator of pump performance. Generally, cavitation occurs when the absolute static pressure at the pump inlet is below the saturation vapor pressure, resulting in a disturbance and disruption of the energy exchange between the impeller and the liquid, and a significant reduction in the external characteristic curve. In severe cases, the liquid flow in the pump can be interrupted, causing the pump not to operate properly. The bubbles are transported to the high-pressure area and ruptured in a very short time, generating massive shock waves. The rupture of the bubbles causes severe damage to the impeller surface material in the form of by pitting and erosion, resulting in the pump producing vibration and noise [1]. It is not possible to suppress cavitation completely. Therefore, to ensure the reliability of pump operation, it is necessary to accurately detect the onset and development of cavitation, and control the operating conditions to prevent cavitation.

The development of cavitation is mainly divided into the inception, development, and degradation stages [2] to [5]. During the different stages of cavitation, there are variations in the quantities of pressure, flow rate and motor power. These features can be used to diagnose the severity of cavitation. The net positive suction head (*NPSH*) is commonly used in engineering to determine the operating conditions and suction performance. According to the ISO 3 standard [6], the *NPSH* value for a 3 % drop in the total delivery head is defined as *NPSH* -required (*NPSHr*), representing cavitation that has fully developed. When

*Corr. Author's Address: Research Center of Fluid Machinery Engineering and Technology, Jiangsu University, Zhenjiang, China, 798917967@qq.com

the cavitation occurs, it causes a change in pump load torque. The electric signal in the motor can evaluate the impeller torque, which can detect the beginning of cavitation. Meanwhile, cavitation can be predicted by measuring the line voltage and phase current on the power transformer [7] and [8]. The normalized amplitude at the third-order rotational speed obtained by measuring the instantaneous angular velocity of the pump and the order spectrum analysis can also be used for characteristic monitoring [9]. Vibration and noise are generated due to the continuous rupture of the bubbles in the high-pressure region accompanied by strong water shock during vapourization inside the pump. There is a discrete frequency or broadband peak in the audible noise spectrum, which is closely related to the development of cavitation. The discrete frequencies are consistent with the *NPSH r*, and both can correspond to a 3 % drop in the total delivery head. The characteristic discrete frequency tones closely associated with cavitation are the resonance caused by structural vibrations or the rupture of bubbles on the inner wall surface of the pump, so the discrete frequency tones can detect the intensity of cavitation. The measurement methods are mainly divided into three types: sound pressure level in air, underwater acoustics and structural vibration [10] to [12]. Černetič [13] and Černetič and Čudina [14] evaluated the uncertainty of cavitation prediction for vibration and noise signals from centrifugal pumps in broad frequency range and at discrete frequencies, verifying that vibration and noise in the audible frequency range are capable of predicting and diagnosing cavitation. Chini et al. [15] analysed the noise spectrum of centrifugal pumps to find the feature of cavitation initiation and found that sound pressure levels at some frequencies can detect the inception of cavitation and quantify the severity of cavitation. Wang et al. [16] found that as cavitation intensifies, the vibration acceleration and noise stabilize at first and then increase apparently, which can determine the *NPSH* -inception of the pump. Zhang et al. [17] found that the cavitation critical point inferred from the vibration level is higher than the *NPSH r* when the head drops by 3 %, indicating the actual cavitation time is earlier than that reflected by the head curve. Dong et al. [18] found that with the decrease of *NPSH* , the total sound pressure level of liquid-borne noise first increase and then decreases, and the sound pressure level of liquid-borne noise in the 2 kHz to 3 kHz frequency range can better predict the initiation of cavitation, with a threshold value of 1 %. Al-Obaidi [19] to [22] used time-domain analysis (TDA) and fast Fourier transform (FFT) techniques for frequency domain analysis (FDA) based on vibration and acoustic analysis methods. The ability of the different methods to diagnose pump cavitation under different operating conditions was compared and evaluated, proposing that peak and peak-to-peak values are more sensitive to cavitation detection in pumps than the RMS and variance feature. Mousmoulis et al. [23] concluded that the impeller's geometric parameters affect the development of cavitation, and that acoustic and vibration measurements can effectively predict cavitation.

Many researchers have asserted that the signal features of vibration, noise, and pressure pulsation can effectively predict the initiation and development of pump cavitation, and proposed signal processing and analysis methods to detect cavitation. However, there is a lack of studies on the sensitivity of measuring point distribution for cavitation prediction. In practice, the characteristics of the vibration signal at different positions are dissimilar. And the liquid-borne noise and pressure pulsation characteristics of the inlet and outlet have different sensitivities to cavitation prediction. Therefore, the location of the measuring points has a crucial influence on the accuracy of cavitation fault diagnosis. To improve the prediction of cavitation and reduce the damage to the pump, it is necessary to research the effect of measuring point distribution on cavitation fault diagnosis.

In the actual operation of the pump, the flow rate is reduced due to the influence of cavitation. In some special applications, there are high demands on the stability of the pump flow rate, for example, fuel pumps for the liquid rocket engine. The cavitation test is usually carried out by keeping the flow rate at a constant value [24], which can intuitively evaluate the cavitation performance of the centrifugal pump. However, it cannot restore the actual situation properly. This paper took a small flow rate and high head centrifugal pump with an inducer and splitter blades as the research object. The valve opening was constant during the cavitation test so that the flow rate varied continuously with the development of cavitation. In addition, hydrophones and high-frequency pressure sensors were installed at the inlet and outlet, and eight vibration sensors were installed at the inlet and outlet flanges, the pump axial and radial, the pump foot, and the bearing housing. The signal characteristics at different locations under different cavitation conditions were measured. The sensitivity of different measuring points was analysed to obtain the optimum method for detecting the onset and development of cavitation in centrifugal pumps and improving the accuracy of cavitation fault diagnosis in centrifugal pumps.

1 TEST AND SIMULATION METHODS

1.1 Research Object

The test bench comprises a vibration and noise high-frequency signal test system, an external characteristic test system and a data acquisition system. Fig. 1a shows that the test equipment includes a cavitation tank, a vacuum pump, pipelines, valves, an electromagnetic flowmeter, test pumps, motors, pressure transmitters, hydrophones, vibration acceleration sensors, and pressure pulsation sensors. The pressure transmitters are located at two times the pipe diameter of the pump inlet and outlet flange. The hydrophones and pressure pulsation sensors are installed eight times the pipe diameter. Moreover, the vibration acceleration sensors are installed in eight positions: inlet flange vertical and horizontal, outlet flange vertical and axial, pump body radial, axial and foot, and the bearing house, as shown in Fig. 1b.

A small flow rate and high head centrifugal pump with a specific speed of 25 was used as the research object, and the equation for the specific speed is as follows [1]:

$$n_s = \frac{3.65n\sqrt{Q}}{H^{3/4}}. \quad (1)$$

The design parameters of the pump are flow rate $Q_d = 5$ m³/h, head $H_d = 9$ m, and rotational speed $n = 2900$ r/min. The centrifugal pump impeller has four main blades and four splitter blades, the diameter of the impeller $D_j = 60$ mm, the outlet width of the impeller $b_2 = 6.5$ mm, and the blade wrap angle $\varphi = 80°$. The inducer has a tapered hub with equal pitch double blades. The axial length of the hub is $h_h = 40$ mm, the axial length of the rim $h_y = 30$ mm, and the inlet sweep angle $\theta_1 = 40°$. The structure of the test pump is shown in Fig. 2.

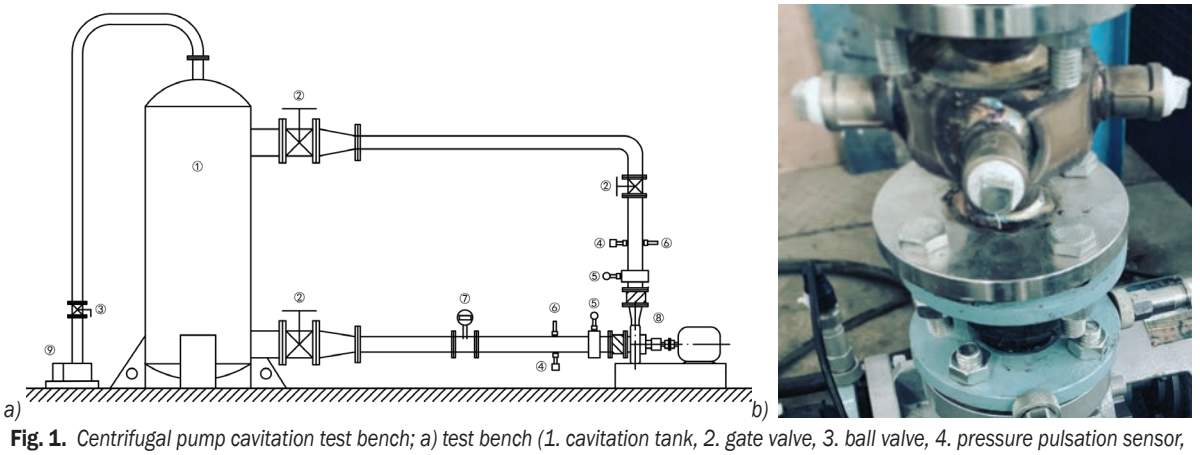

Fig. 1. *Centrifugal pump cavitation test bench; a) test bench (1. cavitation tank, 2. gate valve, 3. ball valve, 4. pressure pulsation sensor, 5. pressure transmitter, 6. hydrophone, 7. electromagnetic flowmeters, 8. pump set, 9. vacuum pump), and b) vibration measuring points*

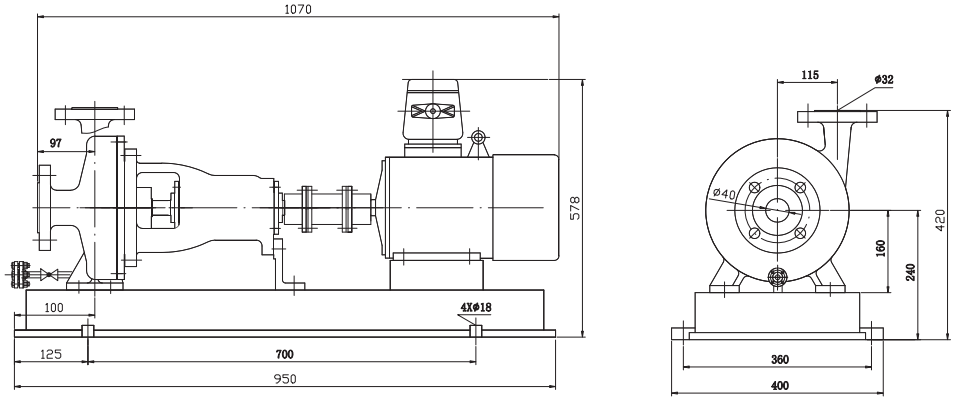

Fig. 2. *Two-dimensional structure of test pump*

1.2 Test Method

The centrifugal pump cavitation tests are usually carried out at a constant flow rate [1], which means that the outlet valve is controlled to keep the flow rate unchanged. The pressure at the inlet is reduced by a vacuum pump, causing the pump to cavitate. This method can effectively obtain the cavitation performance curve of the pump at a fixed flow rate. However, in many practical applications, it is impossible to adjust the valve in time to keep the flow rate constant. The flow rate decreases with the intensification of cavitation and even breaks down. For example, the heavy drop in flow rate caused by cavitation can result in the turbopump being unable to supply oxidizer to the liquid rocket engine in time, leading to severe operational failure of the rocket. Very few cavitation tests with a fixed valve have been carried out, specifically with the flow rate changes as cavitation. Therefore, this paper used this method to conduct cavitation tests and measured pressure pulsation, vibration and noise signals.

The vibration and noise signal under cavitation is significantly different from other mechanical faults in terms of spectral distribution. The broadband character of cavitation has an effect not only on low-frequency signals but also on the higher frequency bands [25]. According to the Nyquist-Shannon sampling theorem, the sampling frequency is more than twice the highest frequency in the signal, so that the information in the original signal is not lost from the acquired digital signal. In order to make the acquired signal reflect the trend in the high-frequency band and ensure the accuracy in the low-frequency band, a sampling frequency of 0 kHz is used to acquire the signal, considering the sensors' operating range and each sampling time is 3s . And the test steps are as follows.

1 Adjust the pump motor speed to 2900 rpm by frequency converter.
2. Control the outlet valve to stabilise the initial flow rate at 5m 3/h.
3 Turn on the vacuum pump and reduce the inlet pressure of the centrifugal pump.
4. Obtain signals for flow rate, pressure pulsation, liquid load noise and structural vibration at different *NPSH a*.

The data were processed and analysed using MATLAB software. The vibration and noise signals are processed as follows:

(1) Vibration acceleration levels

The intensity of vibration (i.e. the energy of vibration), is commonly expressed by physical quantities such as velocity, acceleration and displacement. In contrast, acceleration can better reflect the impact of vibration on the structure. Therefore, the RMS value of acceleration is generally used to express the intensity of the vibration. In practice, the vibration is compound: not a single frequency vibration but superimposed vibrations of multiple frequencies. For evaluating vibration energy, one of the commonly used evaluation indicators is vibration acceleration level. The vibration acceleration level *VAL* is defined as [26]:

$$VAL = 20\lg\left(a_r / a_0\right), \tag{2}$$

where a_r is the RMS of acceleration, and a_0 is the reference acceleration, generally a_0 = 0 6 m/s^2. The unit of vibration acceleration level is decibel, [dB]. And the RMS of vibration acceleration a_r defined as follows [26]:

$$a_r = \sqrt{\frac{1}{T}\int_0^T a_i^2(t)\,d(t)}, \tag{3}$$

where $a_i(t)$ is the acceleration at some point, and T is the total number of samples.

(2) Sound pressure level

The hydrophone is affected by the hydroacoustic sound pressure P in the sound field, which generates an open-circuit voltage U. The open-circuit voltage U is proportional to the sound pressure P. Therefore, the hydrophone sensitivity M can be obtained as [27]:

$$M = U / P, \tag{4}$$

where U is usually defined as the open-circuit voltage generated when the hydrophone is subjected to 1 Pa liquid-borne sound pressure in the sound field.

The sensitivity is compared with the reference value and then taken logarithmically to obtain its corresponding decibel value. In hydroacoustics, 1 μPa is usually used as the sensitivity reference. The output voltage signal of the hydrophone is processed by the FFT method to obtain the voltage spectrum and logarithmically transform the voltage spectrum to obtain the voltage decibel [27]:

$$U_{dB}(f) = 10\lg\left(U_{FFT}(f)\right), \tag{5}$$

where $U_{FFT}(f)$ is the amplitude of the hydrophone's voltage spectrum at some frequency.

The sound pressure level of the liquid-borne noise at this frequency is obtained by subtracting the voltage decibel from the sensitivity of the hydrophone [27]:

$$SPL = U_{dB}(f) - M(f). \tag{6}$$

Similar to the total vibration level calculation, the total sound pressure level of liquid-borne noise is calculated as follows [27]:

$$SPL_t = 20\lg\left(p / p_{ref}\right), \qquad (7$$

where p is the RMS of sound pressure, and p_{ref} is the reference value of underwater sound pressure, 1 μPa.

1.3 Numerical Simulation Method

Creo 5.0 was used to build the 3D model of the pump. The entire model was divided into five parts: the inlet pipe, the inducer, the impeller, the volute and the outlet pipe. ANSYS-ICEM 19.0 was adopted to generate tetrahedral grids, as shown in Fig. 3. To meet the requirements of numerical simulation on grid quality, the grids around the volute tongue and blades are improved and smoothed. The average $y+$ of the grid model is less than 60. Five sets of grids with different cell numbers were generated to verify the grid independence, as listed in Table 1. The judgment basis was that head error of less than 1 % and the time cost of the calculation is as short as possible. The second grid set is closer to the actual parameters in terms of head and has fewer cells than the other sets. Therefore, this paper used this grid for numerical simulation.

Fig. 4 compares the external characteristic results of the numerical simulation with the test. The trend of the numerical simulation and the test result is the same. As the flow rate increases, the head of the centrifugal pump trends to decrease, and the efficiency increase significantly. The head and efficiency at each operating point obtained by the numerical simulation are consistent with the test results, and the maximum error does not exceed 3 %. Therefore, the numerical simulation results have good accuracy.

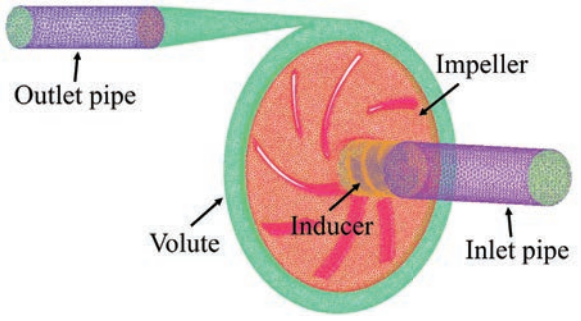

Fig. 3. *Grid model*

The ANSYS-CFX 19.0 software was applied to numerically simulate the cavitation of a centrifugal pump at different inlet pressures. The pump's inlet and outlet boundary conditions were set according to the inlet pressure and the flow rate results obtained by the test at different *NPSH a*. The evolutions of the internal flow field and vapour volume under different cavitation stages were obtained through numerical

Table 1. *Grid independence verification*

Program	Inlet and outlet section	Volute	Inducer	Impeller	Total	Head [m]	Error [%]
1			1.18×10^6	1.53×10^6	4.11×10^6	39.18	0.46
2			9.22×10^5	1.04×10^6	3.37×10^6	39.14	0.35
3	6.42×10^5	7.61×10^5	7.81×10^5	9.43×10^5	3.13×10^6	39.31	0.79
4			6.21×10^5	8.21×10^5	2.85×10^6	40.26	3.23
5			5.35×10^5	7.43×10^5	2.68×10^6	40.32	3.49

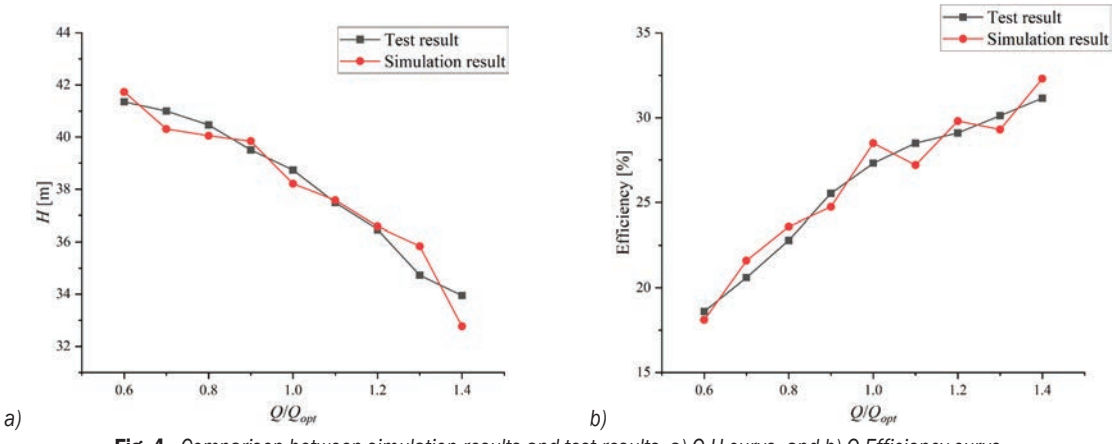

Fig. 4. *Comparison between simulation results and test results, a) Q-H curve, and b) Q-Efficiency curve*

simulation. The turbulence model uses the shear stress transport $k-\omega$ (SST $k-\omega$). This model is widely used in rotating machinery [28]. The SST $k-\omega$ can better calculate the adverse pressure gradient and separation flow. It predicts the pump's performance more accurately [5]. The rotor-stator interfaces use the transient rotor-stator. The pitch change is specified pitch angles with a value of 0°, and the interface between the impeller and the inducer is relatively stationary. The grid connection between the interfaces is set as the general grid interface (GGI). The fixed wall adopts no-slip, and the rotating walls on the impeller and inducer are moving walls. The advection scheme adopts the high resolution, and the transient scheme adopts the second-order backward Euler. The maximum number of inner iteration loops is set to 20. The residual accuracy was 1e -4. The rotational speed is 2900 rpm. The time step is the time taken for each 2° rotation of the impeller, i.e. 0.0001149 s. The total time step is the time taken for five cycles of the impeller. The steady-state results are taken as the initial values for the unsteady-state calculations.

The fluid medium is water at 25 °C. The gas medium is set to water vapour at 25 °C, the Saturation Pressure of the fluid is 0 Pa, the reference pressure is 0 Pa, the volume fraction of the inlet vapour is set to 0, and the volume fraction of the liquid is set to 1. The Zwart cavitation model is used. The net positive suction head available (*NPSH a*) of the pump is calculated as [1]:

$$NPSHa = \frac{P_s - P_v}{\rho g} + \frac{v_s^2}{2g}, \quad (8)$$

where P_s is the pump inlet pressure; P_v is the saturated vapour pressure of the fluid at operating temperature; v_s is the flow rate at the pump inlet.

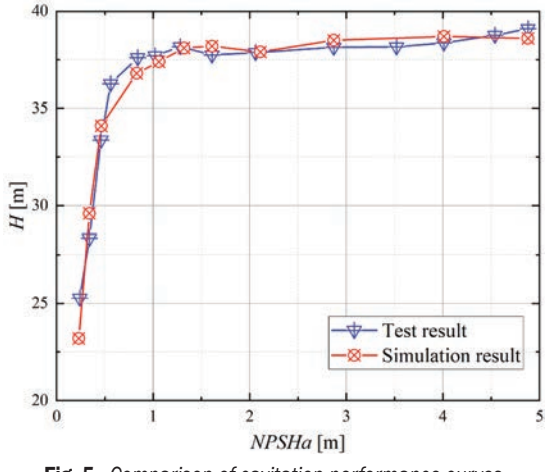

Fig. 5. *Comparison of cavitation performance curves*

Fig. 5 shows the cavitation performance curves obtained from the tests and numerical simulations. The trends in the cavitation performance curves are generally consistent, although there are some errors between the simulation and test results. The inception points of cavitation in test and simulation are almost the same. The *NPSH r* measured by the test is 1.03 m, while the simulation result is 1.06 m, with an error of about 3 %. When the head drops by 1 %, the *NPSH a* values of both are also very close. Therefore, the simulation results can more accurately reflect the evolution of cavitation.

2 ANALYSIS OF CAVITATION PREDICTION METHODS

2.1 External Characteristics

Fig. 6 shows the flow rate and head variation curves for different *NPSH a* obtained from cavitation test with fixed valve. A slight drop in the head occurs as the *NPSH a* decreases from 5 m to 2 m. At *NPSH a* = 3.3 m, the head drops by approximately 1 %. There is some fluctuation in flow rate but no significant drop. When *NPSH a* reduces from 2 m to 1.5 m, the head and flow rate both decrease first and then rise. With the decrease of *NPSH a* (1.5 m to 0.5 m), cavitation in the pump begins to develop continuously, and the head and flow rate decrease again. When *NPSH a* = 1.02 m, the head drops by 3 %, which is the net positive suction head required (*NPSH r*), meaning that full cavitation has occurred at this time [6]. Cavitation continues to intensify after the *NPSH a* falls below 0.5 m. The flow rate and head drop drastically, and the pump has a significant loss of hydraulic performance.

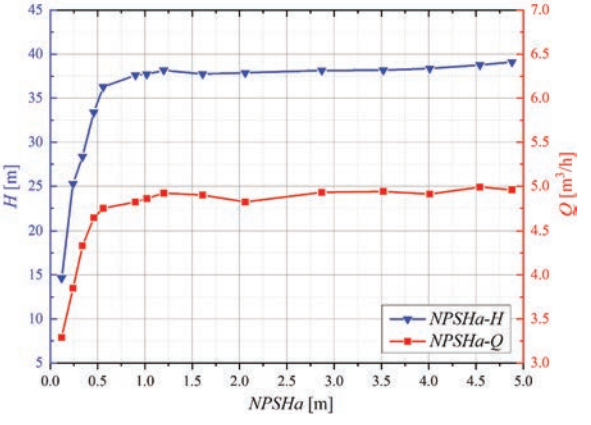

Fig. 6. *Variation of head and flow rate with NPSHa*

At the same time, with the decrease of inlet pressure, the current affected by cavitation also changes obviously, and it has regularity. As shown in

Fig. 7 during the process of *NPSH a* falling from 5 m to 2 m, the overall current shows a downward trend. When *NPSH a* = 2 m, the current decreases by 2 %, then there is a rebound. After the *NPSH a* drops below 1.2 m, the current decreases continuously. And when *NPSH a* is less than 0.5 m, the current drops sharply, by about 12 %. Therefore, consistent with the method proposed in [8], the onset of pump cavitation can be detected by the motor phase currents.

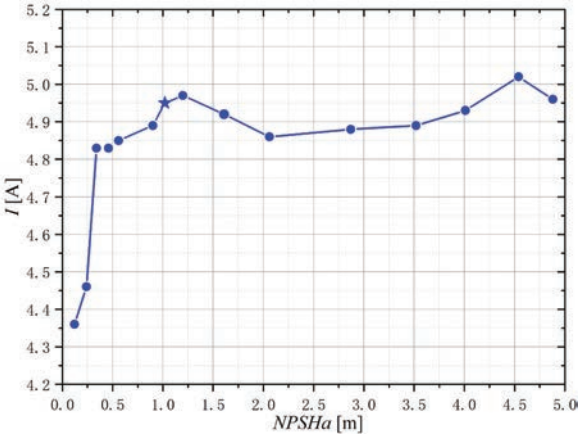

Fig. 7. *Variation of motor current with NPSHa*

2.2 Structural Vibration Signals

The variation curves of vibration acceleration levels for each measuring point at different *NPSH a* as shown in Fig. 8 The vibration acceleration level at each measuring point fluctuates slightly during the non-cavitation stage but remains low. As the *NPSH a* reach the onset of cavitation, the vibration acceleration levels increase significantly, and as the degree of cavitation increases, the vibration acceleration levels rise rapidly after reaching the peak, and then decline. The results are close to the trend of the vibration acceleration on the pump casing in [10], and the rise rate of the vibration acceleration level at *NPSH r* is also similar. Comparing the eight measuring points, the vibration acceleration level at the Bearing house is the highest. However, the overall curve change rate is relatively small, while the vibration acceleration levels of the other measuring points increase significantly during the cavitation development phase. The point marked by the star symbol in the figure is the head drop of 3 %, that is, the vibration acceleration level of each monitoring point at the *NPSH r*. The vibration acceleration level at the outlet flange is higher than that of the inlet flange. However, the amplitude change at the inlet flange is more pronounced, rising by approximately 0.6 % at *NPSH r*. In the non-cavitation stage, the vibration acceleration of the pump radially is larger than the pump axially. With the intensification of cavitation, the vibration acceleration level at the pump axial significantly exceeds that at the pump radial, and increases by about 0.5% at *NPSH r*.

Fig. 9 shows the vibration acceleration levels spectrum with cavitation development at different measuring points. The trend of each measuring point shows that as the cavitation continues to increase, there is an evident broadband characteristic. The inlet flange horizontal and vertical measuring points have a strong signal distribution in all frequency bands during the non-cavitation phase, but the overall distribution is dispersed. After the onset of cavitation, the vibration signal in the 600 Hz to 4000 Hz frequency band enhances significantly. The outlet flange measuring point is mainly concentrated below 1000 Hz and in the band of 2000 Hz to 6000 Hz. With the *NPSH a* decreasing, the signal change in the range

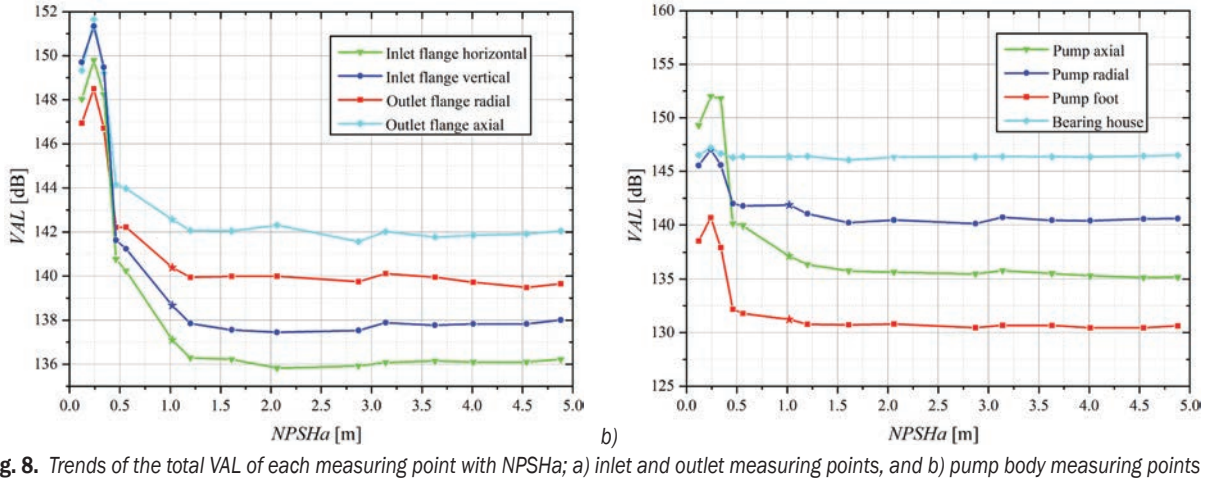

a) b)

Fig. 8. *Trends of the total VAL of each measuring point with NPSHa; a) inlet and outlet measuring points, and b) pump body measuring points*

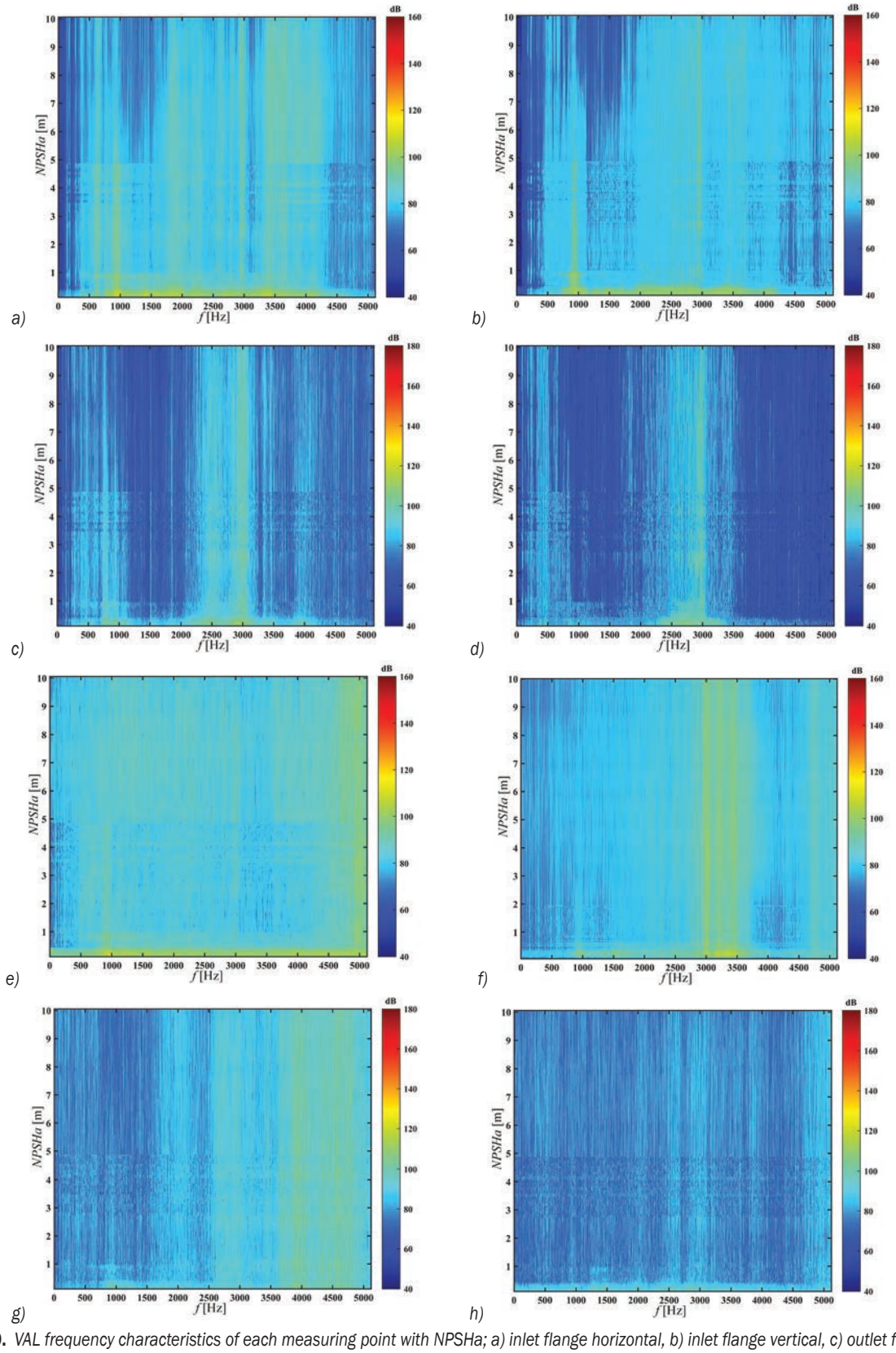

Fig. 9. *VAL frequency characteristics of each measuring point with NPSHa; a) inlet flange horizontal, b) inlet flange vertical, c) outlet flange radial, d) outlet flange axial, e) pump axial, f) pump radial, g) pump foot, and h) bearing house*

of 2000 Hz to 0 Hz is more obvious. In contrast, the inlet measuring point is more sensitive to the onset of cavitation. The pump body axial measuring point shows a strong vibration signal appears in all frequency bands. The spectrum distribution at the pump body radial is also broader, and the vibration acceleration level signal in 0 Hz to 3 Hz is intense. However, with the development of cavitation, the variation of the vibration acceleration level signal in the whole frequency range is not as pronounced as that of pump body axial. The bearing house measuring point has a relatively strong amplitude in the high-frequency band, while the overall vibration acceleration level of the pump foot is small, and the signal distribution is relatively sparse. Both spectral variations are not sufficiently apparent and less sensitive to the onset of cavitation.

2.3 Liquid-borne Noise Signals

With the decrease of inlet pressure, *NPSHa* continuously decreases, and the frequency domain of the peak signal of the inlet and outlet liquid-borne noise gradually shrinks, as shown in Fig. 1. As the cavitation effect intensifies, the signal above 2 0 dB inlet almost disappears. The sound pressure level in 1000 Hz to 0 0 Hz at the outlet drops below 10 dB. The length of the vapour attached to the blade's working surface increases, and there are large oscillations in the tail of the cavitation. It causes the bubbles to fall off, and the unstable cavitation intensifies, thus leading to broad frequency pulsations in the low-frequency band of the liquid-borne noise. Moreover, because the cavitation in part of the flow channel blocks the entry of the main flow, the number of effective flow channels is reduced, thereby changing the frequency distribution of the liquid-borne noise. Although there is also a more pronounced change in the outlet liquid-borne noise signal, the variation is insignificant compared to the inlet. Fig. 11 shows that with the decrease of the *NPSHa*, the inlet liquid-borne noise presents a continuous decreasing trend, which is similar to the trend in [10]. However, the sound pressure level of the liquid-borne noise at

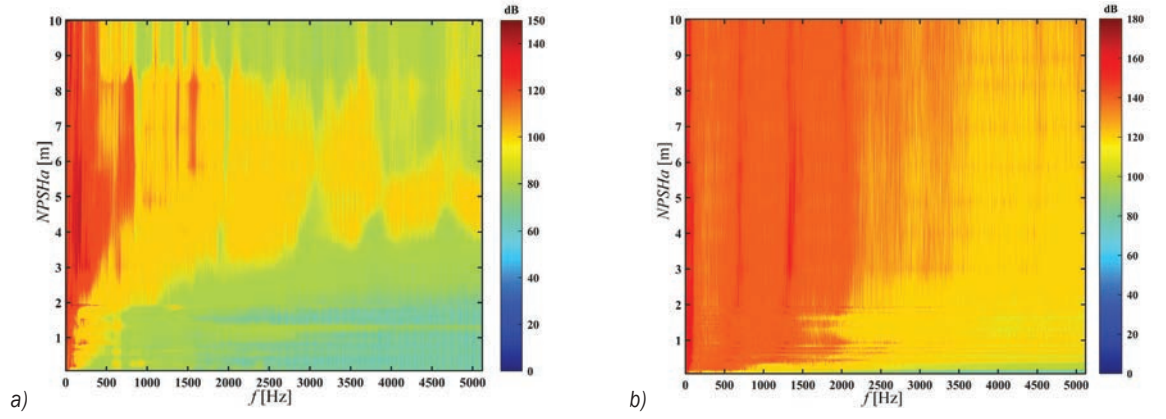

Fig. 10. *Liquid-borne noise frequency characteristics; a) at the inlet, and b) at he outlet with NPSHa*

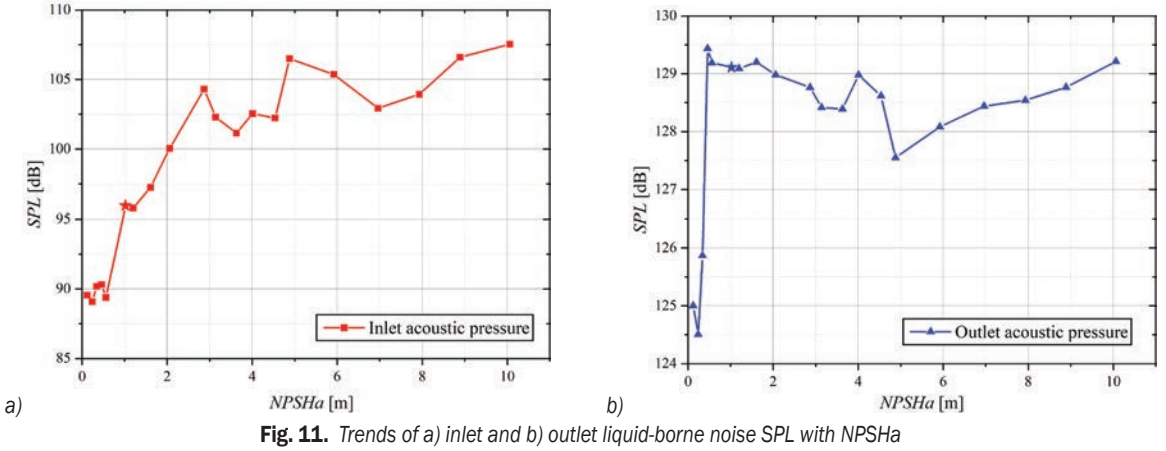

Fig. 11. *Trends of a) inlet and b) outlet liquid-borne noise SPL with NPSHa*

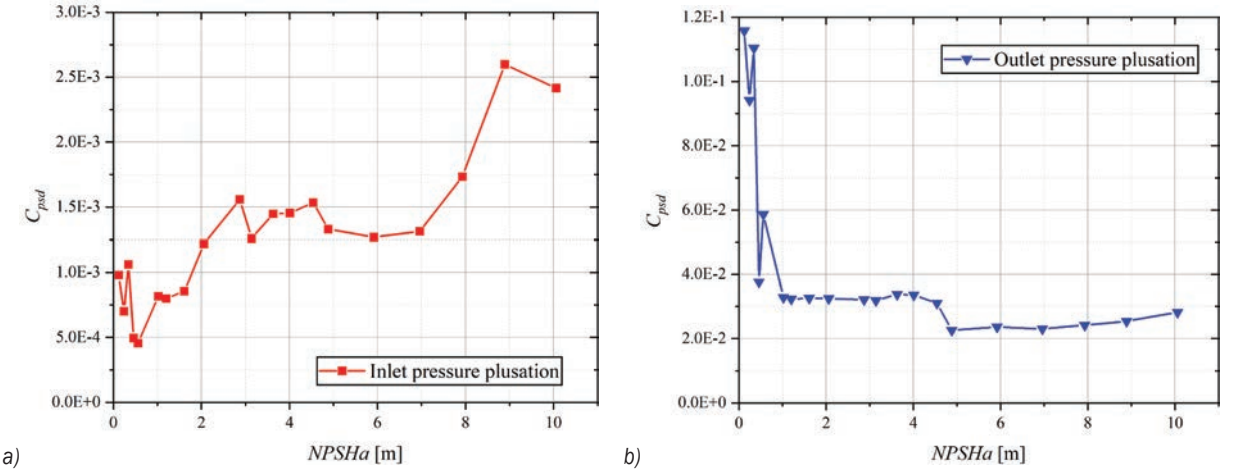

Fig. 12. *Trends of a) inlet and b) outlet pressure pulsation PSD with NPSHa*

the outlet first decreased, then increased, and finally decreased rapidly. At the net positive suction head required point, the inlet liquid-borne noise decreases by approximately 4 %, while the outlet liquid-borne noise decreases by approximately 1 %. The comparison shows that the inlet liquid-borne noise measuring point is more sensitive to the outlet.

2.4 Pressure Pulsation Signals

The power spectral density (PSD) method was used to process the pressure pulsation signal to determine the intensity of the pressure pulsation. Fig. 12 shows the pressure pulsation intensity coefficient as the *NPSHa* decreases. It can be found that the inlet pressure pulsation shows a decreasing trend with the reduction of the *NPSHa*, while the outlet pressure pulsation is maintained first and then rapidly rising trend. When the head drops by 3 %, the inlet pulsation intensity decreases by 63 %, while the outlet pulsation intensity increases by 39 %. The inlet pulsation intensity shows an overall decreasing trend as the *NPSHa* decreases. Although there are some fluctuations, it can better reflect the pressure pulsation intensity change with the development of cavitation. The outlet pressure pulsation does not change significantly before the onset of cavitation. When it is close to complete cavitation, the sudden rise occurs, and the rate of change is not as apparent as the inlet measuring point. Therefore, relative to the measuring point at the outlet position, the pressure pulsation measuring point at the inlet can better predict the inception and development of cavitation.

3 ANALYSIS OF NUMERICAL SIMULATION RESULTS

3.1 Vapour Volume Evolution

Fig. 13 shows the evolution in the volume fraction distribution of vapour under different NPSHa. As the NPSHa decreases, the vapour volume in the impeller continues to extend from the blade inlet to the outlet. The development of vapor volume presented in the results is consistent with [4]. When the NPSHa is 16 m, it is the inception of cavitation. A lower level of vapour has appeared on the suction surface of the blade inlet, but there is no significant change in head and flow rate. When the NPSHa is 13 m, the vapour volume area expands. At this time, the head does not decrease but instead increases slightly, which is due to the bubbles generated on the blade surface, which improve the flow state in the pump. When approaching the NPSHr, the vapour area begins to diffuse towards the blade working surface, and the flow rate and head drop by approximately 2.8 % and 3 %, respectively. At NPSHa is 0.8 the vapour area spreads to the root of the splitter blade, occupying about one half of the flow channel, and the head drops by more than 5 %. While the flow rate drops slightly lags behind the head, dropping by about 3 %. As NPSHa continues to decline, the vapour area occupies the entire flow channel of the impeller and flows into the diffusion section of the volute, blocking the flow channel. The flow rate and head drop by 27 % and 34 %, the pump's performance is seriously affected.

3.2 Pressure Pulsation Analysis

To investigate the characteristic changes of the pressure pulsation signal in the pump under different

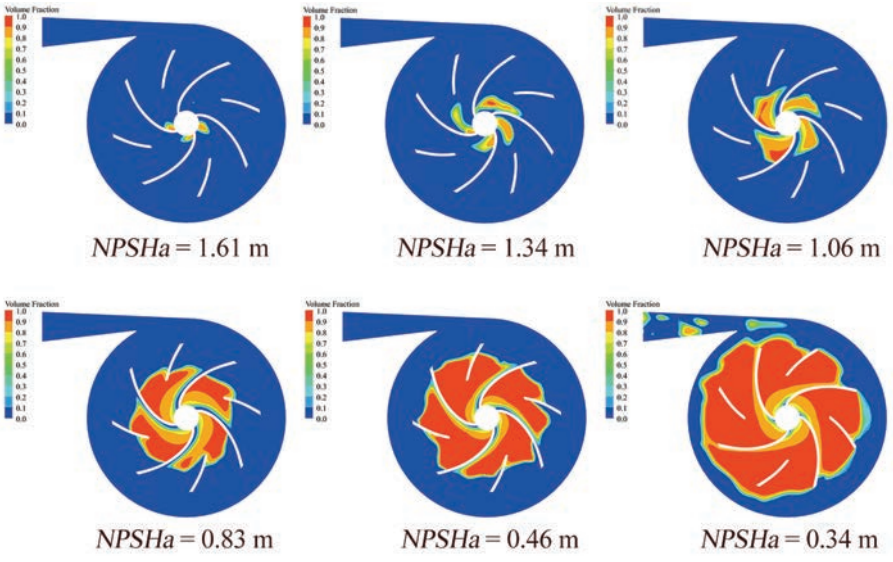

Fig. 13. *Volume fraction distribution of vapor under different NPSHa*

NPSHa, eight pressure pulsation monitoring points were set up at the interface between the impeller and the volute, and each monitoring point is separated by 45°, as shown in Fig. 14. The stable results of the last three cycles are ectracted from the unsteady calculation. The fast Fourier transform (FFT) algorithm was used to calculate the discrete Fourier transform (DFT) of the pressure pulsation time-domain signal at different cavitation stages at each measuring point. The frequency-domain results are shown in Fig. 15.

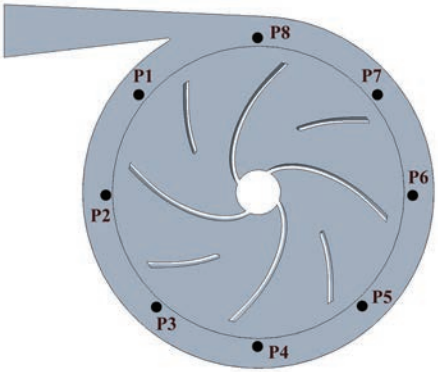

Fig. 14. *Pressure pulsation measuring points*

The impeller rotational speed is n = 2900 rpm, so the shaft frequency f_r = 48.3 Hz, the main blade passing frequency f_{MBPF} = 193.3 Hz, and the total blade passing frequency f_{BPF} = 967 Hz. In the non-cavitation phase, the main frequency of the pressure pulsation at the monitoring points P2 to P4 and P8 is the total blade passing frequency f_{BPF} of the impeller, which is eight times the shaft frequency. The main frequency of P5 to P7 is the main blade passing frequency f_{MBPF}, (i.e,, four times the axis frequency). When cavitation causes a 3 % drop in head, the main frequency is at the main blade passing frequency f_{MBPF} at all six monitoring points except for P3 and P7, where the main frequency is at the f_{BPF}. When the head drops by 5 %, the main frequency at P1 appears at two times the shaft frequency. The main frequency P3 is at the main blade passing frequency f_{MBPF}. For other monitoring points, the main frequency is at the total blade passing frequency f_{BPF}. When the head drops sharply by 10 %, the main frequency of some monitoring points shift. Except for P4, P5, and P6 at the f_{BPF}, the main frequencies appear at the 1/3 and 2/3 shaft frequency. As cavitation develops and the amplitude of the pressure pulsation signal increases, the interference at harmonic frequencies becomes severe. The main frequency of some monitoring points also has some changes.

4 CONCLUSIONS

This paper studied the influence of measuring point distribution for pump cavitation diagnosis. The liquid-borne noise, vibration acceleration and pressure pulsation at different positions of the pump units were measured through the fixed valve test. The RMS was used to process the signal data of each cavitation condition, which can better reflect the sensitivity of monitoring points to cavitation than the data analysis at the characteristic frequency in [10] and [13]. The sensitivities of different measuring points to predict

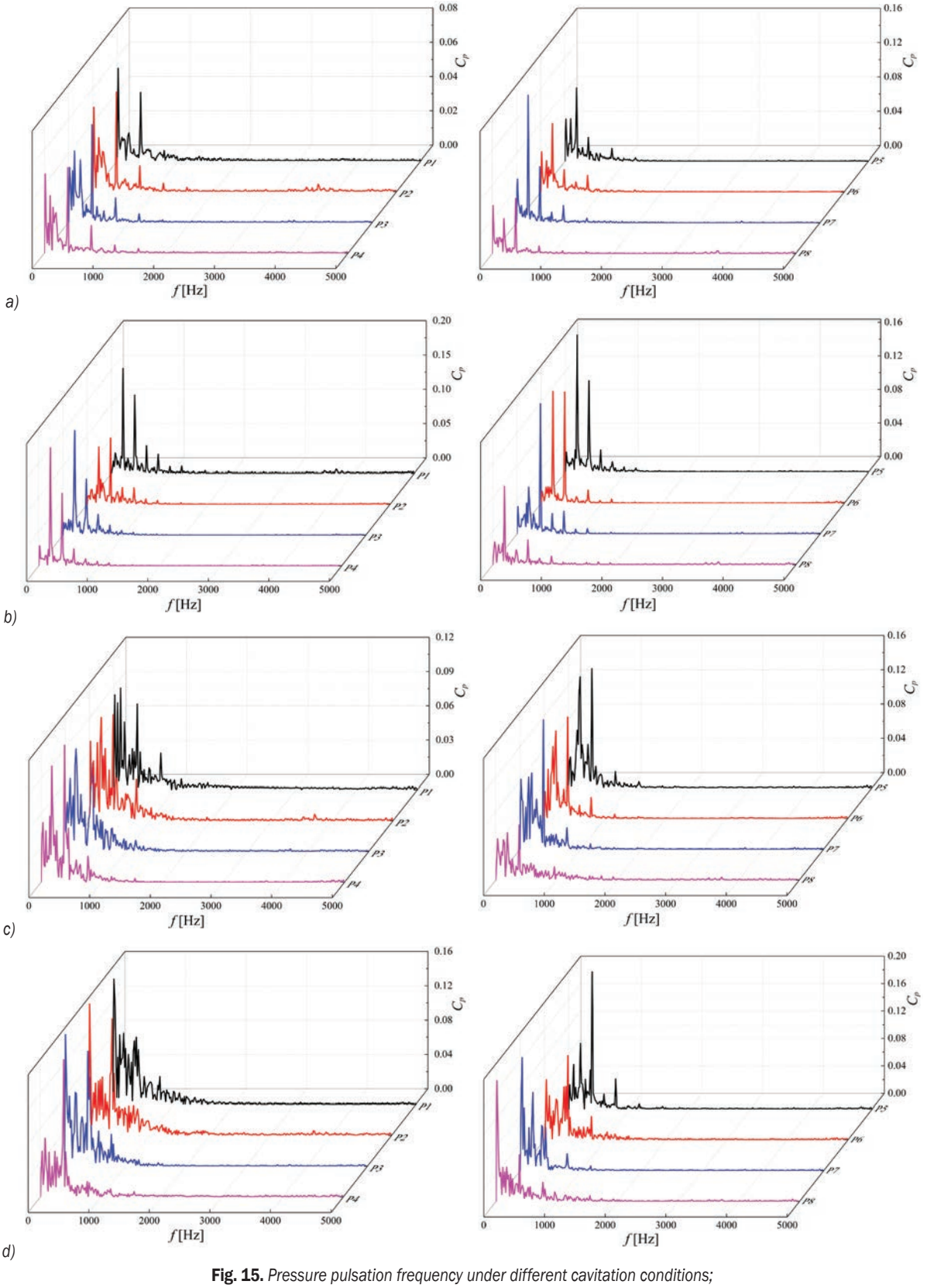

Fig. 15. *Pressure pulsation frequency under different cavitation conditions; a) none-cavitation, b) 3 % drop in head, c) 5 % drop in head, d) 27 % drop in head*

cavitation were compared. Furthermore, the SST k–ω turbulence model and Zwart cavitation model were used to numerically simulate the evolution of the vapour's volume distribution and pressure pulsation characteristics inside the pump.

With the development of cavitation, the flow rate decreases more slowly than the head. When the head drops by 3 %, the flow rate reduces by about 2.8 %. The motor current also shows a certain decrease, which can be used to predict the onset of cavitation and agrees with the findings [8]. When $NPSH_a$ is less than 0.5 m, the current drops sharply, about 2 %. The vibration acceleration level of each measuring point increases significantly. The measuring points of the inlet flange and the pump body axial are more sensitive to predicting cavitation, and both decreased by 0.6 % .

The frequency band of the liquid-borne noise peak shrinks significantly. At the $NPSH_r$ operating point, the sound pressure level of the inlet liquid-borne noise decreases by 4 %, while the outlet decreases by 1 %, so the inlet liquid-borne noise measuring point is better for cavitation prediction. The inlet pressure pulsation intensity shows a decreasing trend, while the outlet is the opposite. The rate of change of inlet pressure pulsation intensity is more pronounced than the outlet. When the head drops by 3 %, the inlet pulsation intensity decreases by 63 %, while the outlet pulsation intensity increases by 39 %. The main frequency of the pressure pulsation signal is mainly distributed at the total blade passing frequency f_{BPF}. However, with the development of cavitation, the main frequency is influenced by the harmonic frequency, and some of the main frequencies are shifted. In summary, the inlet flange and pump casing axial vibration measuring points, inlet liquid-borne noise, and pressure pulsation measuring points have superior sensitivity and are suitable for cavitation fault diagnosis.

The arrangement of measuring points for cavitation fault diagnosis proposed in this work can be effectively applied to other pumps. The proposed method can be extended to the diagnosis of other pump faults, such as impeller damage, shaft misalignment, and shaft imbalance. However, regarding the thresholds for fault signal prediction, since different types of pumps have different performances and requirements, it is necessary to make specific judgments according to the actual situation. It can be further investigated in subsequent studies to improve the accuracy of cavitation fault diagnosis.

5 ACKNOWLEDGEMENTS

The authors would like to thank the financial support from National Natural Science Foundation of China (No. 51879122,51779106), National Key Research and Development Program of China (Grant No. 2016YFB0200901, 2017YFC0804007), Zhenjiang key research and development plan (GY2017001, GY2018025), the Open Research Subject of Key Laboratory of Fluid and Power Machinery, Ministry of Education, Xi-hua University (szjj2017-09, szjj2016068), Sichuan Provincial Key Lab of Process Equipment and Control (GK201614, GK201816), Jiangsu University Young Talent training Program-Outstanding Young backbone Teacher, Program Development of Jiangsu Higher Education Institutions (PAPD), and Jiangsu top six talent summit project (GDZB-017).

6 REFERENCES

[1] Guan, X.F.(1995). *Handbook of Modern Pump Technology*, Astronautic Press, China.

[2] Guo, X., Zhu, L., Zhu, Z., Cui, B., Li, Y. (2015). Numerical and experimental investigations on the cavitation characteristics of a high-speed centrifugal pump with a splitter-blade inducer. *Journal of Mechanical Science and Technology*, vol. 29, p. 259-267, **DOI:10.1007/s12206-014-1232-x**.

[3] Luo, X.W., Ji, B., Tsujimoto, Y. (2016). A review of cavitation in hydraulic machinery. *Journal of Hydrodynamics*, vol. 28, p. 335-358, **DOI:10.1016/S1001-6058(16)60638-8**.

[4] Dong, L., Shang, H., Zhao, Y., Liu, H., Wang, Y. (2019). Study on unstable characteristics of centrifugal pump under different cavitation stages. *Journal of Thermal Science*, vol. 28, p. 608-620, **DOI:10.1007/s11630-019-1136-2**.

[5] Al-Obaidi, A.R. (2019). Effects of different turbulence models on three-dimensional unsteady cavitating flows in the centrifugal pump and performance prediction. *International Journal of Nonlinear Sciences and Numerical Simulation*, vol. 20, no. 3-4, p. 487-509, **DOI:10.1515/ijnsns-2018-0336**.

[6] ISO 3555 (1977). *Centrifugal, Mixed Flow and Axial Pumps-Code for Acceptance Tests-Class B*. International Organization for Standardization, Geneva.

[7] Stopa, M.M., Cardoso Filho, B.J., Martinez, C.B. (2013). Incipient detection of cavitation phenomenon in centrifugal pumps. *IEEE Transactions on Industry Applications*, vol. 50, no. 1, p. 120-126, **DOI:10.1109/TIA.2013.2267709**.

[8] Harihara, P.P., Parlos, A.G. (2006). Sensorless detection of cavitation in centrifugal pumps. *ASME International Mechanical Engineering Congress and Exposition*, p. 187-192, **DOI:10.1115/IMECE2006-14655**.

[9] Al-Hashmi, S., Gu, F., Li, Y., Ball, A. D., Fen, T., Lui, K. (2004). Cavitation detection of a centrifugal pump using instantanous angular speed. Engineering Systems Design and Analysis, p. 185-190, **DOI:10.1115/ESDA2004-58255**.

[10] Čudina, M., Prezelj, J. (2009). Detection of cavitation in situ operation of kinetic pumps: effect of cavitation on the characteristic discrete frequency component. *Applied Acoustics*, vol. 70, no. 9, p. 1175-1182, **DOI:10.1016/j.apacoust.2009.04.001**.

[11] Čudina, M. (2003). Noise as an indicator of cavitation in a centrifugal pump. *Acoustical Physics*, vol. 49, no. 4, p. 463-474, **DOI:10.1134/1.1591303**.

[12] Čudina, M. (2003). Detection of cavitation phenomenon in a centrifugal pump using audible sound. *Mechanical Systems and Signal Processing*, vol. 17, no. 6, p. 1335-1347, **DOI:10.1006/mssp.2002.1514**.

[13] Černetič, J. (2009). The use of noise and vibration signals for detecting cavitation in kinetic pumps. *Proceedings of the Institution of Mechanical Engineers, Part C: Journal of Mechanical Engineering Science*, vol. 223, no. 7, p. 1645-1655, **DOI:10.1243/09544062JMES1404**.

[14] Černetič, J., Čudina, M. (2011). Estimating uncertainty of measurements for cavitation detection in a centrifugal pump. *Measurement*, vol. 44, no. 7, p. 1293-1299, **DOI:10.1016/j.measurement.2011.03.023**.

[15] Chini, S.F., Rahimzadeh, H., Bahrami, M. (2005). Cavitation detection of a centrifugal pump using noise spectrum. *International Design Engineering Technical Conferences and Computers and Information in Engineering Conference*, p. 13-19, **DOI:10.1115/DETC2005-84363**.

[16] Wang, Y., Liu, H., Yuan, S., Tan, M., Wang, K. (2012). Experimental testing on cavitation vibration and noise of centrifugal pumps under off-design conditions. *Transactions of the Chinese Society of Agricultural Engineering*, vol. 28, no. 2, p. 35-38, **DOI:10.3969/j.issn.1002-6819.2012.02.007**. (in Chinese)

[17] Zhang, N., Yang, M., Gao, B., Li, Z. (2015). Vibration characteristics induced by cavitation in a centrifugal pump with slope volute. *Shock and Vibration*, vol. 2015, art. ID 294980, **DOI:10.1155/2015/294980**.

[18] Dong, L., Zhao, Y., Dai, C. (2019). Detection of inception cavitation in centrifugal pump by fluid-borne noise diagnostic. *Shock and Vibration*, vol. 2019, art. ID 9641478, **DOI:10.1155/2019/9641478**.

[19] Al-Obaidi, A.R. (2020). Experimental comparative investigations to evaluate cavitation conditions within a centrifugal pump based on vibration and acoustic analyses techniques. *Archives of Acoustics*, vol. 45, no. 3, p. 541-556, **DOI:10.24425/aoa.2020.134070**.

[20] Al-Obaidi, A.R. (2019). Investigation of effect of pump rotational speed on performance and detection of cavitation within a centrifugal pump using vibration analysis. Heliyon, vol. 5, no. 6, art. ID e01910, **DOI:10.1016/j.heliyon.2019.e01910**.

[21] Al-Obaidi, A.R. (2020). Detection of cavitation phenomenon within a centrifugal pump based on vibration analysis technique in both time and frequency domains. *Experimental Techniques*, vol. 44, p. 329-347, **DOI:10.1007/s40799-020-00362-z**.

[22] Al-Obaidi, A.R., Mishra, R. (2020). Experimental investigation of the effect of air injection on performance and detection of cavitation in the centrifugal pump based on vibration technique. *Arabian Journal for Science and Engineering*, vol. 45, p. 5657-5671, **DOI:10.1007/s13369-020-04509-3**.

[23] Mousmoulis, G., Karlsen-Davies, N., Aggidis, G., Anagnostopoulos, I., Papantonis, D. (2019). Experimental analysis of cavitation in a centrifugal pump using acoustic emission, vibration measurements and flow visualization. *European Journal of Mechanics-B/Fluids*, vol. 75, p. 300-311, **DOI:10.1016/j.euromechflu.2018.10.015**.

[24] Pan, Z.Y., Yuan, S.Q. (2013). *Fundamentals of Cavitation in Pumps*, Jiangsu University Press, Jiangsu .

[25] Dong, L., Zhao, Y.Q., Dai, C., Wang, Y. (2018). Research on cavitation acoustic characteristics of centrifugal pump based on fluid-acoustic field coupling method. *Advances in Mechanical Engineering*, vol. 10, no. 5, **DOI:10.1177/1687814018773665**.

[26] Yu, H. (2016). *Vibration Noise Measurement and Analysis Technology of Ship*. China Light Industry Press, p. 4-11.

[27] Du, G. (2012). *Acoustic Fundamentals*. Nanjing university Press, Nanjing, p. 127-128.

[28] Alahmadi, Y., Nowakowski, A. (2016). Modified shear stress transport model with curvature correction for the prediction of swirling flow in a cyclone separator. *Chemical Engineering Science*, vol. 147, p. 150-165, **DOI:10.1016/j.ces.2016.03.023**.

Strojniški vestnik - Journal of Mechanical Engineering 68(2022)5, 339-349
DOI:10.5545/sv-jme.2022.4
Original Scientific Paper
Received for review: 2022-01-07
Received revised form: 2022-02-14
Accepted for publication: 2022-03-01

Optimization of a Tuned Mass Damper Location for Enhanced Chatter Suppression in Thin-Wall Milling

Mohanraj Selvakumar* – Prabhu Raja Venugopal – Gautham Velayudhan
PSG College of Technology, Department of Mechanical Engineering, India

In this paper, a method of optimizing the location of a tuned mass damper (TMD) for enhancing the chatter stability limits of a thin-walled workpiece by using numerical techniques is proposed with due consideration of the mass effect of TMD. The dominant mode of the workpiece is identified from the simulated and measured frequency response functions of the workpiece. Two TMDs each having a single degree of freedom are designed, and a finite element model to predict the response of the workpiece-damper system is developed. The effect of damper location on the chatter stability of the thin-walled workpiece is investigated. Furthermore, the locations for TMDs are optimized for enhanced chatter stability of the workpiece by using response surface methodology. Milling tests were performed on workpieces with and without TMDs. A three-fold improvement in the minimum stable depth of cut is realized after incorporating the TMDs at their optimal locations on the thin-walled workpiece.

Keywords: chatter, thin-wall milling, tuned mass damper, response surface optimization

Highlights

- *The dynamics of a thin-wall workpiece is studied using numerical and experimental methods.*
- *A single degree of freedom tuned mass damper is designed to suppress the dominant mode of the workpiece.*
- *A numerical model is developed to investigate the effect of the location of the tuned mass damper on the chatter stability of the workpiece.*
- *The location of the tuned mass damper is optimized to enhance the chatter stability of the workpiece by adopting the response surface method.*
- *The milling test revealed a three-fold improvement in the critical depth of cut of the workpiece by introducing TMD.*

0 INTRODUCTION

Regenerative chatter is a sort of self-excited vibration that occurs during milling and other machining processes. Chatter has several drawbacks, including poor surface finish, shorter tool life, reduced material removal rate, and increased machining noise. Chatter is usually caused by the most compliant element of the structural dynamic chain. Because workpiece is the most compliant part in thin-wall milling, investigations on the chatter stability of the thin-walled part are gaining momentum. Typical thin-walled parts used in aerospace structures are shown in Fig. 1

Altintas et al. [1] proposed a frequency domain analytical solution for a dynamic milling model based on the zero-order approximation (ZOA) method to predict chatter stability. Budak et al. [2] proposed an analytical method for modelling varying workpiece dynamics and their effect on process stability.

Iglesias et al. [3] stated that stability lobe diagrams (SLDs) aid in the practical selection of the optimum cutting conditions determined either by time domain or frequency domain-based methods. Heng et al. [4] suggested a new tuned mass damper (TMD) that was designed and optimized using a sequential quadratic programming algorithm. Experiments showed that the critical depth of the cut had increased as observed from SLD.

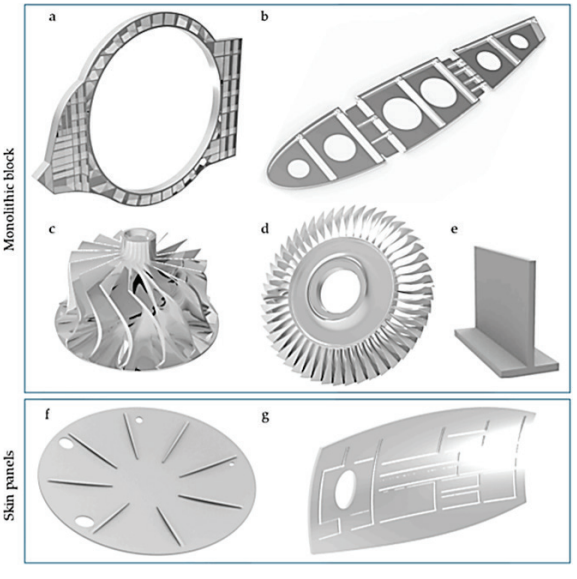

Fig. 1. *Typical thin-ribbed aerospace structures; a) frame, b) rib, c) impeller, d) blisk, e) sample part, f) bulkhead, and g) fuselage skin* [5]

Fei et al. [6] proposed a moving damper for chatter suppression while milling flexible components

*Corr. Author's Address: PSG College of Technology, Department of Mechanical Engineering, India, smr.mech@psgtech.ac.in

wherein the damper is supported on the back surface of the workpiece. Shui et al. [7] proposed a tuneable stiffness vibration absorber that could be tuned by changing the position of the slider. Sims [8] presented a new analytical solution for tuning methodology and observed that the critical depth of cut improved by 40 % to θ % compared to using classical TMD. Yang et al. [9] suggested two degrees of freedom (DOF) TMD that has both translational and rotational motions. The proposed method was found to reduce vibration amplitude by 8 % and double the critical depth of cut. Yang et al. [10] proposed a passive damper with tenable stiffness to accommodate variations in part dynamics during thin-wall milling, which reduced the surface roughness by θ %. Bolsunovsky et al. [11] developed a TMD based on spindle frequency, which had a 20-fold mitigation of vibration amplitude. Wang [12] proposed a new non-linear TMD with a friction-spring element that improved the critical depth of cut by θ % as compared to the optimally tuned linear TMD.

Yang et al. [13] designed a two-DOF magnetic TMD to mitigate workpiece vibration in multiple modes. Researchers [14] and [15] proposed a passive damping solution using tuned viscoelastic dampers to mitigate the vibration of thin-wall castings focusing on change in coupled interaction between tool and workpiece due to the addition of tuned dampers. Yang et al. [16] investigated numerically the real part-based tuning by employing the minimax numerical approach to maximize the minimum real part of the primary structure under harmonic excitation. They demonstrated the effectiveness by raising the minimum stability limit with single and multiple TMDs. Burtscher and Fleischer [17] proposed an innovative adaptive TMD with variable mass to suppress chatter in the machine tool.

Despite many studies on the application of TMD for chatter suppression, the literature review reveals that no extensive studies on the effect of TMD mounting location on chatter stability of thin-wall workpieces are carried out. Hence, the present work addresses the above gap and focuses on proposing a generalized methodology for optimizing the location of TMD, taking into consideration the mass effect of TMD.

1 METHODOLOGY

In the present work, numerical and experimental methods are used to study the dynamics of a thin-wall workpiece. A TMD is designed based on the modal parameters of the workpiece corresponding to the dominant mode. A numerical model of the workpiece with TMD is developed to investigate the effect of the location of TMD on chatter stability and optimize the same by using the response surface optimization method.

1.1 Milling Dynamic Model

Precise dynamic modelling of the milling system plays a vital role in the design and analysis of TMDs. In thin-wall milling, the dynamic rigidity of the workpiece rather than the cutter is one of the critical parameters that decide the occurrence of chatter. Moreover, the dynamic rigidity of the workpiece in the normal direction to the cutter axis limits the process stability and material removal rate. Hence, a single degree of freedom milling dynamic model developed by considering only the dynamics of the workpiece to be sufficient to investigate chatter stability in thin wall milling.

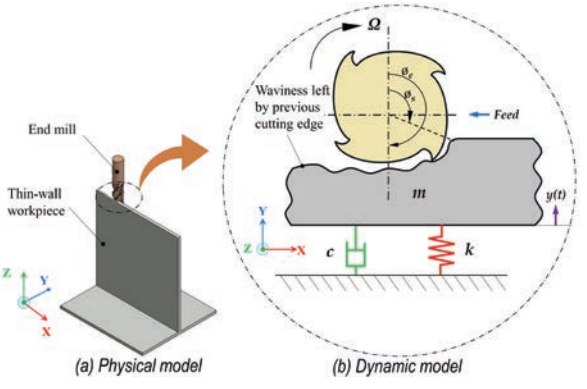

Fig. 2. *Single degree of freedom milling dynamic model*

A single degree of freedom milling dynamic model proposed by Budak et al. [3], presented in Fig. 2, is adopted for the study. The model consists of a spring-mass-damper system, where m, k, and c respectively represent the modal mass, modal stiffness, and modal damping coefficient at a dominant mode of vibration of the workpiece. The dynamic chip thickness that modulates the cutting force is denoted as $h(t)$. The governing equation of motion of the system shown in Fig. 1c an be written as

$$m\ddot{y} + c\dot{y} + ky = K_s \cdot b \cdot h(t), \qquad (1$$

where, K_s and b are the specific cutting resistance of the workpiece material and axial depth of cut, respectively. According to the regenerative chatter theory, the axial depth of cut at the stability limit of the milling process is given by

$$b_{lim} = \frac{-2\pi}{N_t \alpha_{yy} K_t Re\left[\Lambda\left(i\omega_c\right)\right]}, \quad (2)$$

where b_{lim} is the limiting depth of cut, N_t is the number of teeth in the cutter, α_{yy} is the directional coefficient in the *y*-direction K_t is tangential cutting force coefficient, $Re[\Lambda(i\omega_c)]$ is the negative real part of receptance (displacement per unit force) of the workpiece in the *y*-direction and ω_c is the chatter frequency. The directional dynamic milling coefficient in the *y*-direction, α_{yy} is given by

$$\alpha_{yy} = \frac{1}{2}\left[-cos\left(2\theta\right) - 2K_r\theta - K_r sin\left(2\theta\right)\right]_{\phi_s}^{\phi_e}. \quad (3)$$

In Eq. (3), θ is the tool engagement angle, K_r is the radial milling force coefficient, and ϕ_s and ϕ_e are the start and exit angles of the tool during the machining. The relation between the phase shift (ϵ), the integer number of oscillations (n) between each tooth pass and the chatter frequency (ω_c) can be expressed as

$$\frac{60\omega_c}{\Omega} = 2\pi n + \epsilon, \quad (4)$$

where Ω is the spindle speed of the machine tool. Using Eqs. (2) and (4), the stability lobe diagram can be plotted for different values of *n*.

1.2 Prediction of Thin-Rib Dynamics

Modal parameters, namely the modal frequency, modal mass, and modal damping ratio corresponding to the dominant mode of the workpiece, play a significant role in the design of TMD for enhanced chatter stability. These parameters are determined with the help of the frequency response function of the workpiece obtained at its critical location. The critical location is the location on the workpiece where the vibration amplitude is maximal. Numerical modal analysis is used to identify the critical location from the mode shapes of the workpiece. A representative thin-wall workpiece (Fig. 3) made of Aluminium 6061 alloy with the following properties is considered for the study: Young's modulus was 69 GPa, Poisson's ratio 0.33 and density 2700 kg/m^3. The bottom face of the base plate is constrained in all directions and the analysis is performed using a commercial finite element code ANSYS Workbench®. A chatter range of 0 Hz to 3000 Hz is considered for the analysis, which is the tooth passing frequency range associated with end milling using four flute cutters with a spindle speed range of 0 rpm to 6000 r pm.

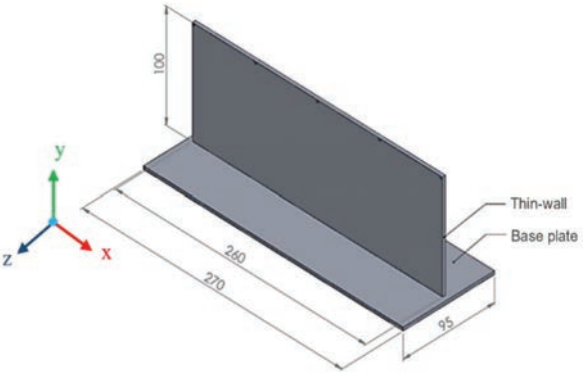

Fig. 3. *Thin-walled workpiece*

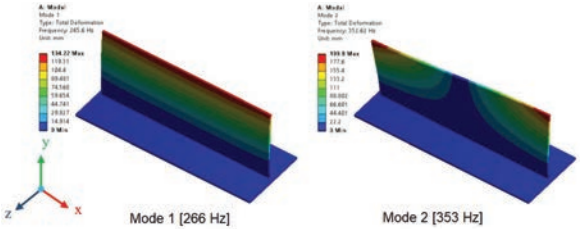

Fig. 4. *Mode shapes of workpiece*

Fig. 4 depicts the mode shapes of the workpiece obtained from the modal analysis, where the bending mode about the *x*-axis and twisting mode about the *y*-axis are observed at 266 Hz and 353 Hz, respectively. The mode shapes are symmetrical to the YZ plane and the locations L1 and L5 (Fig. 5) are identified as critical locations where relative amplitudes of vibration are maximal. Hence, due to the symmetric nature of mode shapes, L1 is considered to be the critical location for subsequent analysis.

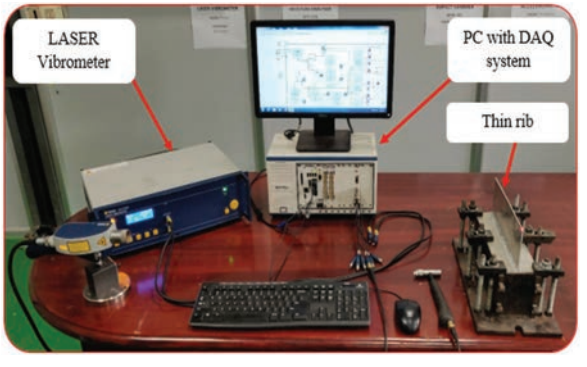

Fig. 5. *Experimental setup for impact hammer test*

An impact hammer test (Fig. 5) was performed on the workpiece at L1 to determine the dynamic parameters of the workpiece through frequency response function (FRF) measurements. An impact hammer (Make: Brüel & Kjær, sensitivity: 2.097

mV/N) was used to excite the workpiece at L1 with an impulse force of 5 N to 10 N applied in +Y direction and vibration response was recorded right behind L1 using a Laser Doppler Vibrometer (Make: Polytec, model: NLV-2500, sensitivity: 500 μm/V). The signals were obtained using a DAQ system (Make: National Instruments, model: PXIe-1078) at a sampling rate of 5 kHz and receptance was estimated using LabVIEW® software.

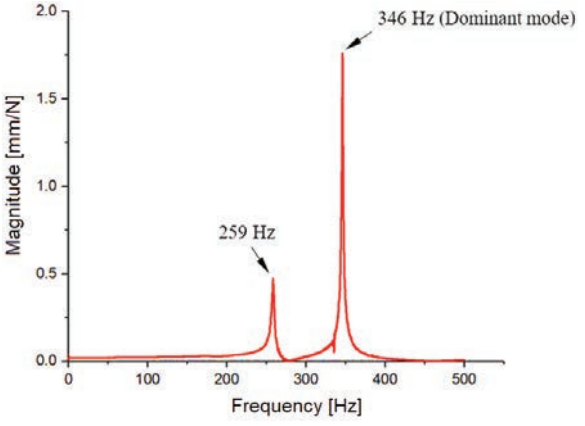

Fig. 6. *Magnitude of receptance at location L1*

The magnitude of receptance obtained from the test is depicted in Fig. 6 which shows two distinct peaks at 259 Hz and 346 Hz that correspond to the frequencies of 266 Hz and 353 Hz, respectively, as predicted by numerical analysis. A mode at 346 Hz is termed a dominant mode, which has a maximum magnitude of 1.72 mm/N. The damping ratio is identified as 0.0023 for the dominant mode using the half-power bandwidth method. The frequencies obtained by numerical analysis are in close agreement with experimentation with a maximum deviation of 4.2 %, thereby validating the numerical model.

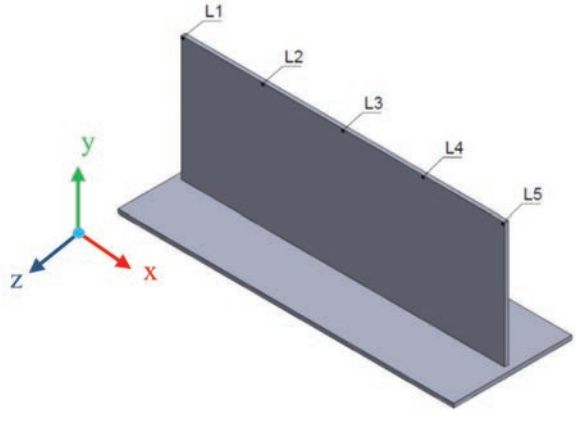

Fig. 7. *Excitation locations on the workpiece*

The validated model is tuned with the experimentally obtained damping ratio to predict the receptances of the workpiece. It is evident from Eq. (2) that $Re[\Lambda(i\omega_c)]$ of the workpiece is a decisive factor for chatter stability in thin wall milling of a given workpiece material and tool combination. However, $Re[\Lambda(i\omega_c)]$ of the workpiece, in turn, depends on the location of excitation during machining. The harmonic response analysis is performed on the tuned model using ANSYS Workbench® to predict the $Re[\Lambda(i\omega_c)]$ of the workpiece at critical locations. A force of unit magnitude is applied at L1 along the +Y direction, and the frequency of the applied force is swept between 100 Hz to 400 Hz to completely capture the $Re[\Lambda(i\omega_c)]$ of the dominant mode.

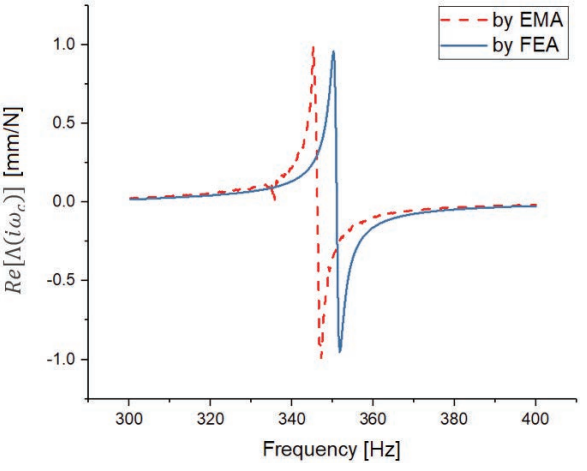

Fig. 8. *Comparison of real parts of receptance of L1*

A comparison of the real part of receptances of the workpiece at L1 obtained with numerical and experimental methods is shown in Fig. 8 $Re[\Lambda(i\omega_c)]$ predicted using the numerical method is in close agreement with that obtained by experimentation with a frequency shift of 7 Hz corresponding to a 2 % deviation in natural frequency. Furthermore, $Re[\Lambda(i\omega_c)]$ obtained with the numerical method is 0.325 mm/N, which is in close agreement with the experimental result of 0.302 mm/N with a maximum deviation of 4 %.

1.3 Design of Tuned Mass Damper (TMD)

The modal stiffness (k) of the workpiece is calculated from the negative maximum of the imaginary part of receptance $Im[\Lambda(i\omega_c)]$ and damping ratio measured at L1 by the Eq. (5) [18].

$$k = \frac{-1}{2\zeta\, min\left(Im\left[\Lambda\left(i\omega_c\right)\right]\right)}. \quad (5$$

The modal stiffness of the workpiece corresponding to $Im[\Lambda(i\omega_c)]$ of 47 mm/N is calculated as 273 kN/m and the modal mass is found to be 0.020 kg. A mass ratio (μ) of 5 % [8] is used to design the TMD. The stiffness of the TMD is computed using Eq. (6 [18].

$$f_r = \frac{f_d}{f_w} = \sqrt{\frac{\mu + 2 + \sqrt{2\mu + \mu^2}}{2\left(1+\mu\right)^2}}, \quad (6$$

where, f_r, f_d and f_w are the frequency ratio, the natural frequency of the damper and the dominant frequency of the workpiece, respectively. The design parameters of TMD are calculated and are presented in Table 1.

Table 1. *Design parameters of TMD*

Frequency ratio	1.036
Natural frequency [Hz]	358
Effective mass [kg]	0.0013
Stiffness [kN/m]	6.58

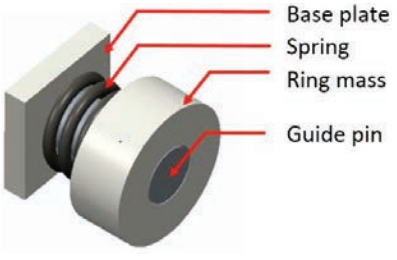

Fig. 9. *Proposed design of TMD*

Fig. 9 shows a proposed design of TMD, which consists of a ring mass, guide pin, base plate, and a helical compression spring. The base plate of the TMD is made of an aluminium sheet of 3 mm thickness. Steel dowel pins of 2.5 mm and 25 mm long are used as guide pins. An open coil helical spring of mean coil diameter, wire diameter, free length, and number of active coils of 0 mm, 1 mm, 0 mm, and 3 turns, respectively, is designed to obtain the required stiffness.

1.4 Effect of Location of TMD on Chatter Stability

Some of the applications of TMD based on conventional approaches may not yield optimum performance in thin wall milling. Therefore, the location on the workpiece that results in an optimum mass ratio needs to be identified by considering the stationary component of TMD.

A TMD having a single degree of freedom is designed based on the design parameters obtained in the previous section. The TMD is mounted on one of the locations on the workpiece defined by X and Y coordinates about the coordinate system, as shown in Fig. 0. A COMBIN4 element with longitudinal stiffness of 6 kN/m is used between the ring mass and the base plate of the TMD. A frictionless contact is applied between the ring mass and the guide pin, and the base plate of the TMD is attached to the workpiece using a bonded connection.

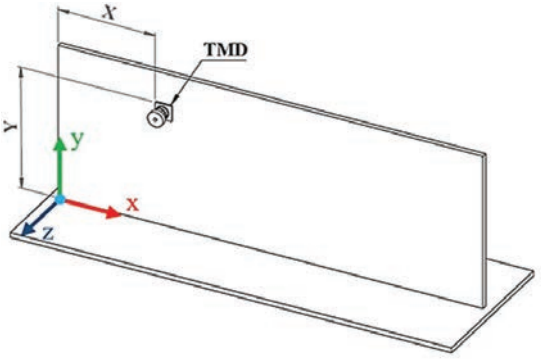

Fig. 10. *TMD and its location on the workpiece*

Parameterized harmonic response analysis was carried out with coordinates of damper location (X, Y) as input parameters and the magnitude of the negative maximum of imaginary parts of receptance ($Im[\Lambda(i\omega_c)]$) as an output parameter. Thirty-six mounting locations of TMD on the workpiece were considered for the investigation.

Custom design of experiments with 8 design points as the coordinate of the damper is employed for the analysis. The X-coordinate of the damper is varied from 0 mm to 20 mm in steps of 6 mm along the length of the plate. Similarly, the Y-coordinate of the damper is varied from 25 mm to 00 mm in steps of 25 mm. Harmonic response analysis is performed on the workpiece for location L1 and the negative maximum of the real part of receptance of the ($Re[\Lambda(i\omega_c)]$) is noted for all the thirty-six locations of TMD.

Similar analyses are carried out for the other two excitation locations L2 and L3 and the results presented as response surfaces as shown in Fig. 1, which portrays the effect of TMD location on the negative ($Re[\Lambda(i\omega_c)]$) of the workpiece three excitation locations.

Since the workpiece is geometrically symmetrical about the YZ plane, which passes through L3, the

contours of $|(Re[\Lambda(i\omega_c)])|$ of L5 and L4 will be the mirror images of the contours of that of L1 and L2, respectively. As L3 is the node point for mode 2, it exhibits the least value for $|(Re[\Lambda(i\omega_c)])|$ in almost all the locations of the damper except for L1 and L5

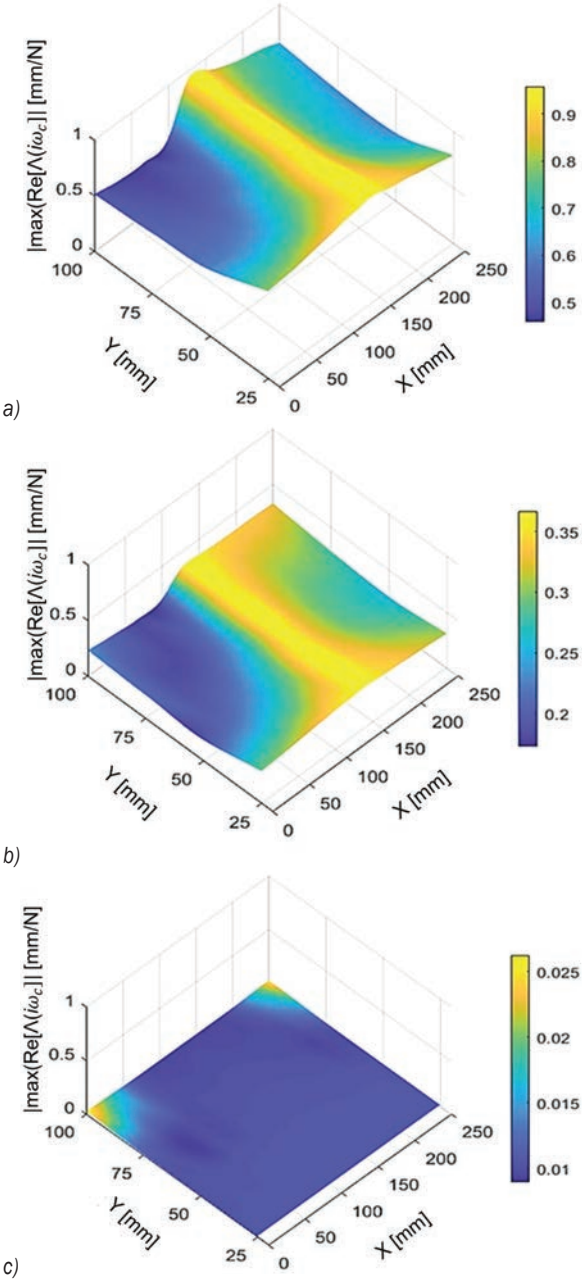

Fig. 11. Effect of TMD location a) L1, b) L2 and c) L3 on $(Re[\Lambda(i\omega_c)])$

It is inferred from Fig. 11 that the damper is ineffective for all values of Y when it is located at X = 0 mm and most effective near the location of excitation. Hence, the optimum location of TMD needs to be identified for effective chatter suppression.

1.5 Optimization of TMD Location for Enhanced Chatter Stability

The optimum location of the damper for enhancing the chatter stability of the workpiece is carried out by employing response surface optimization. The response surfaces obtained for are optimized using genetic algorithms. The basic flow chart for carrying out parameterized harmonic analysis followed by optimization is shown in Fig. 12. The optimization is performed for each of the five excitation locations to minimize the of the workpiece. Three candidate points that represent the optimal locations for the damper on the workpiece are obtained for each excitation location.

It is inferred from Table 2 that the Y-coordinates for the candidate points of all excitation locations remain the same irrespective of X-coordinates. The average *Y*-coordinate of damper for minimizing is found to be 86 mm, which is 90 % of the height of the part from the base. The corresponding to the critical location L1 is found to be higher in comparison to other locations as expected. Considering the critical locations L1 and L5, it is evident from Table 2 that the coordinates, as well as the objective equation values, are quite close to each other for all the three candidate points. Therefore, the average *X*-coordinate of the damper for minimizing chatter is found to be 65 mm, which is at 25 % of the length of the workpiece from the respective excitation locations. Hence, the TMD is placed on the workpiece at (X, Y) = (65, 90) mm and harmonic response analysis is performed for each of the excitation locations of the workpiece.

Table 2. *Optimal locations of damper for each excitation location*

Location	Candidate point	Coordinates [mm]		Objective equation values
		X	Y	Max $(Re[\Lambda(i\omega_c)])$ [mm/N]
L1	1	65.89	98.79	-0.4691
	2	63.89	98.45	-0.4692
	3	61.77	98.83	-0.4688
L2	1	47.30	98.81	-0.1942
	2	51.33	98.95	-0.1924
	3	53.70	98.77	-0.1908
L3	1	62.48	98.63	-0.0107
	2	195.62	98.69	-0.0106
	3	76.62	96.22	-0.0089

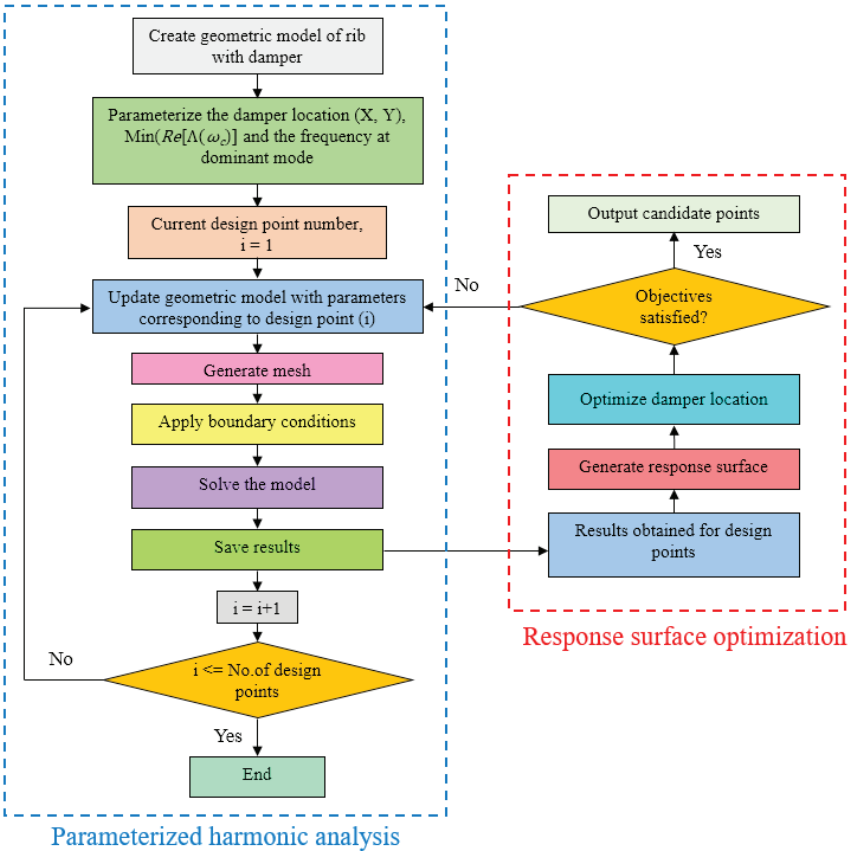

Fig. 12. *Flow chart for parameterized harmonic analysis and optimization*

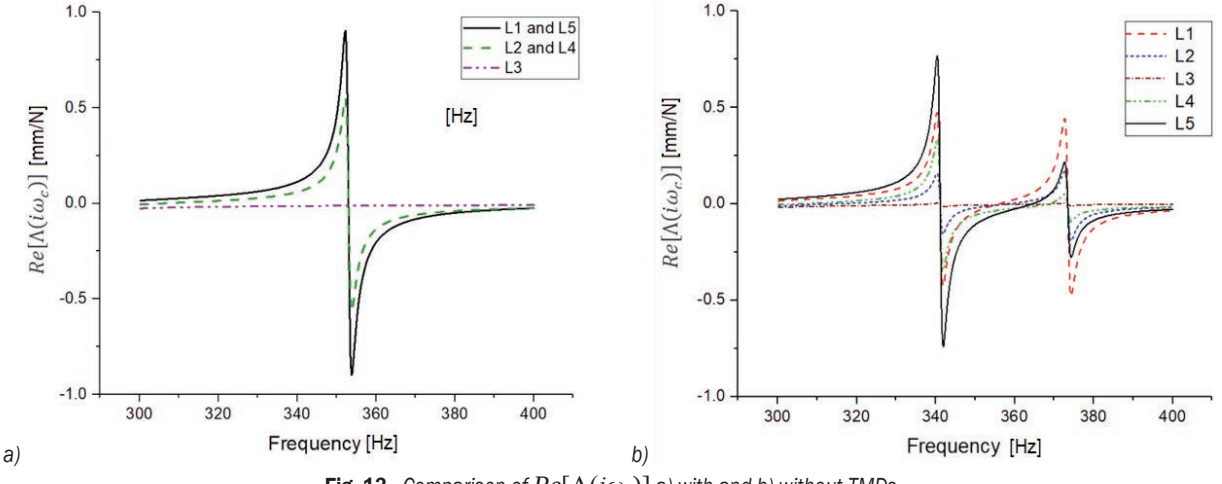

Fig. 13. *Comparison of* $Re[\Lambda(i\omega_c)]$ *a) with and b) without TMDs*

A comparison of the real parts of receptance of the plate with and without TMD is shown in Fig. 13. It is inferred from Fig. 13 that negative ($Re[\Lambda(i\omega_c)]$) of the workpiece at L1 is reduced from -0.92 mm/N to -0.46 mm/N, which corresponds to about a 50 % improvement in dynamic stability. Also, the TMD is found to be effective for the locations L1, L2, and L3 and least effective for L4 and L5 when located at the optimum location for L1. This implies that the use of a single TMD is effective when the cutter traverses between L1 and L3 and is least effective between L3 and L5. Therefore, one more TMD with the same

modal parameters was designed and located at the optimum location for L5 and the harmonic response analyses were repeated for L1 and L5

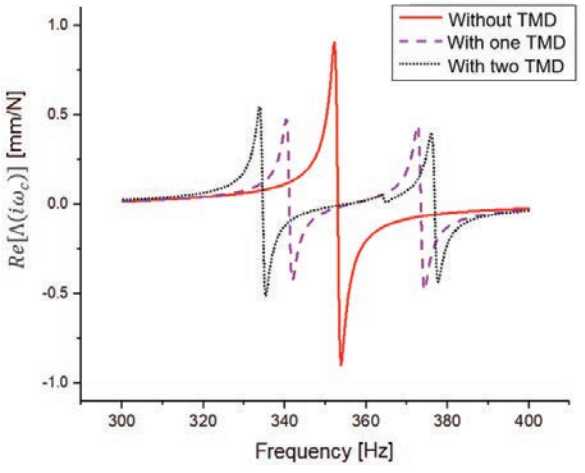

Fig. 14. *Real parts of receptance at L1 and L5*

Fig. 14 depicts the comparison of the real part of receptance obtained at L1 and L5 of the workpiece without TMD, with one TMD and two TMDs. It is evident from the figure that the use of two TMDs considerably minimizes $Re[\Lambda(i\omega_c)]$ at L5 from 0.477 mm/N to 0.551 mm/N, which correspond to an improvement of 13 % when compared to the use of one TMD and 46 % without TMD. Even though the negative maximum values of *Re* of the workpiece at L1 and L5 are minimized using two TMDs, there is a drop in the corresponding chatter frequencies from 351 Hz to 348 Hz.

2 EXPERIMENTAL VALIDATION OF OPTIMUM LOCATION OF TMD

2.1 Impact Hammer Test on Workpiece with TMDs

TMDs were fabricated as per the design parameters obtained in the previous section. Ring masses are prepared by stacking and gluing the brass washers of outer diameter, inner diameter and thickness of 16 mm, 5 mm, and 0.3 mm, respectively. Each washer weighs about 4.73 g, and three washers are used to achieve a total mass of 2.73 g, which is slightly larger than the required mass of 2.60 g. The increased mass of the ring mass alters the mass ratio from 5 % to 5.2 %, which is negligible and insignificant. The prepared TMDs were mounted on the workpiece at optimum locations obtained in the previous section. Fig. 15 shows the workpiece with TMDs in which TMD1 and TMD2 were mounted at the optimum locations corresponding to L1 and L5, respectively. Initially, the impact hammer test was carried out with one TMD mounted at an optimum location and then with both the TMDs mounted at their optimum locations.

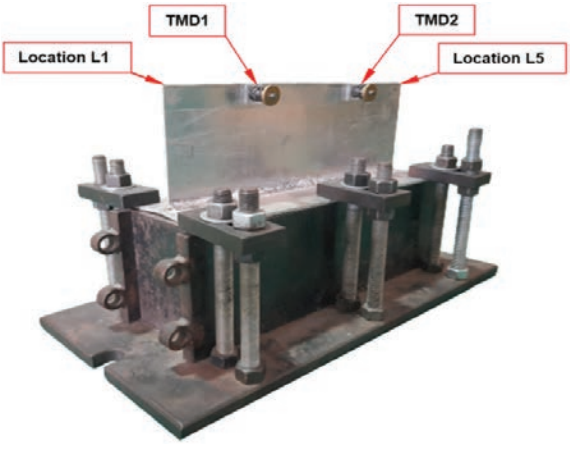

Fig. 15. *Thin-walled workpiece with TMDs*

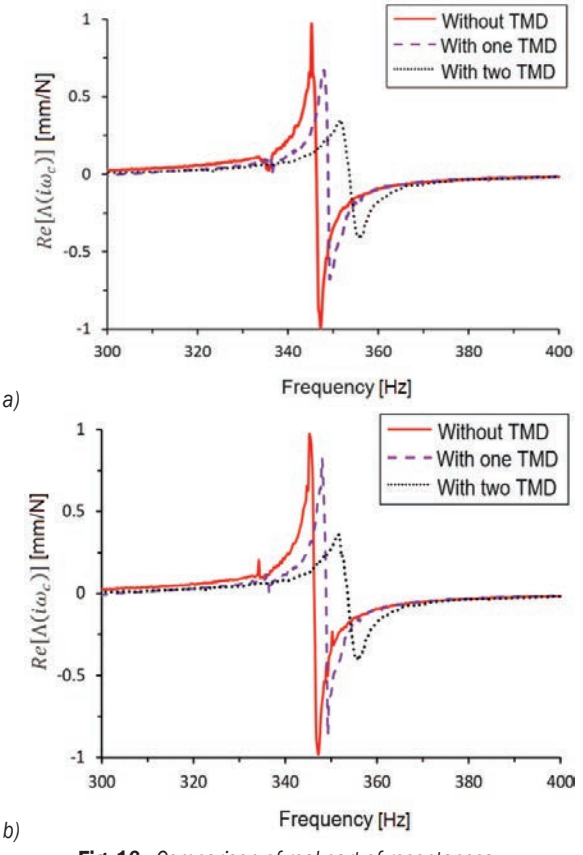

Fig. 16. *Comparison of real part of receptances; a) location L1, and b) location L5*

The comparison of Reobtained at critical locations L1 and L5 are shown in Figs. 16 a and b, respectively. It is inferred from Figs. 16 a and b that

the negative real parts of receptance of the workpiece are minimized at both critical locations of the workpiece after the introduction of TMDs. When one TMD is located at the optimum location for L1, there is a marginal improvement in negative Re of L5 as observed as predicted by numerical analysis.

The marginal improvement in Re of L5 is attributed to the inertial effect of TMD located at L1. It is also revealed from Fig. 16 b that a considerable improvement in the dynamic stability of the workpiece is observed on applying two TMDs at their optimum locations.

The Reof the workpiece at critical locations for the cases without TMD, with one TMD and with two TMDs are found to be about -0.092 mm/N, -0.047 mm/N, and -0.09 mm/N, respectively, which correspond to 23 % and 96 % improvements in the dynamic stability of the workpiece.

2.2 Machining Test

The chatter stability of the undamped and damped workpiece was predicted and compared by using SLDs which were plotted (Fig. 17) by using the modal parameters and the identified cutting coefficients of the workpiece material, namely K_{tc} = 2118 N/mm^2, K_{rc} = 753.5 N/mm^2, K_{ac} = 2080 N/mm^2, K_{te} = 22.9 N/mm, K_{re} = 25.6 N/mm, and K_{ae} = 1.6 N/mm. A comparison of SLDs of the workpiece without TMD and that with two TMDs is depicted in Fig. 17. It is observed that the minimum stable depths of cut of the undamped and damped workpiece are in the order of 0.08 mm and 0.24 mm, respectively, which correspond to a three-fold improvement in the chatter stability of the workpiece.

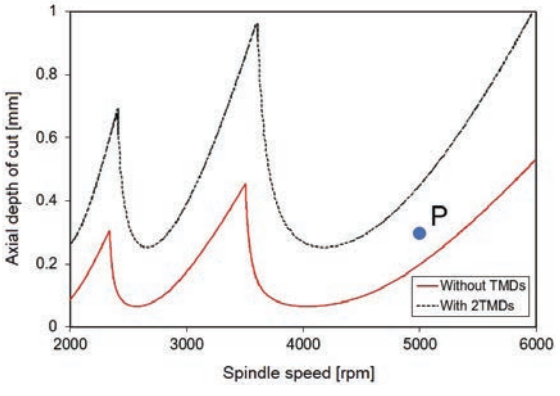

Fig. 17. *Stability lobe diagrams*

The application of TMDs for rough milling may not be feasible as a large amount of material needs to be removed from both sides of the workpiece which hinders machining operation and greatly alters the structural dynamics. Also, the surface roughness is of least consideration in rough milling. However, chatter needs to be avoided during finish milling as it affects the surface quality of the machined part. The chatter stability during finish milling of thin walls can be improved by mounting the TMDs on a surface that is opposite to the surface of the thin wall being machined.

Milling tests were carried out on a three-axis machining centre (Jyoti & Model: RDX20) shown in Fig. 18 using a carbide milling cutter of diameter 16 mm with 4 flutes. The TMDs were mounted at their optimum locations on the surface of the thin wall just behind the surface being machined. Down milling was carried out on the damped and undamped parts on the part surface opposite to the surface where TMDs were placed. The test was conducted under similar cutting conditions to validate the damping characteristics of TMDs. Similar cutting parameters, namely a feed rate of 1200 m/min, spindle speed of 6000 rpm, axial depth of cut of 0.3 mm and radial depth of cut of 1 mm were selected from the SLDs. The above parameters were selected so that point P (Fig. 17) lies in the region of the SLD which results in unstable machining without TMDs. A uniaxial accelerometer (Dytran 3224A 1 with a sensitivity of 98 mV/g) was used to acquire vibration signals during milling. The time domain and frequency domain signals, along with the machined surface quality, with and without TMDs are shown in Fig. 19.

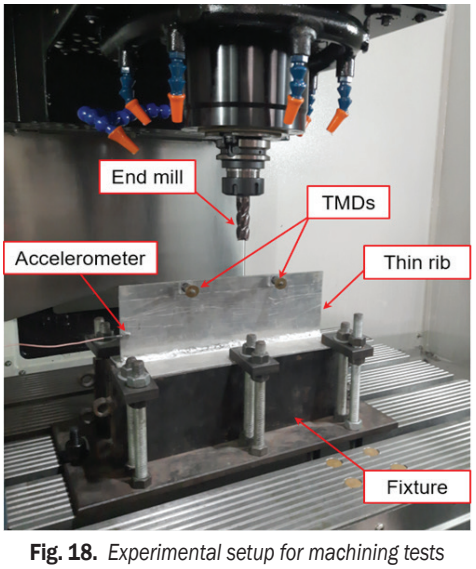

Fig. 18. *Experimental setup for machining tests*

It is observed from the figure that the magnitude of vibration has reduced from 8 g to 8 g after

introducing TMDs. It can also be observed from the frequency spectrum that the spike at 340 Hz (chatter frequency of undamped workpiece) has vanished. Because of the above, the damped workpiece does not exhibit chatter marks, as shown in Fig. 19. The setup for surface roughness measurement is shown in Fig. 20. The surface roughness of the machined workpieces was measured using a surface roughness tester (Make: Kosaka Lab, Model: SE-1200) with a diamond stylus of 5 µm radius at a measuring speed of 0.2 m/s.

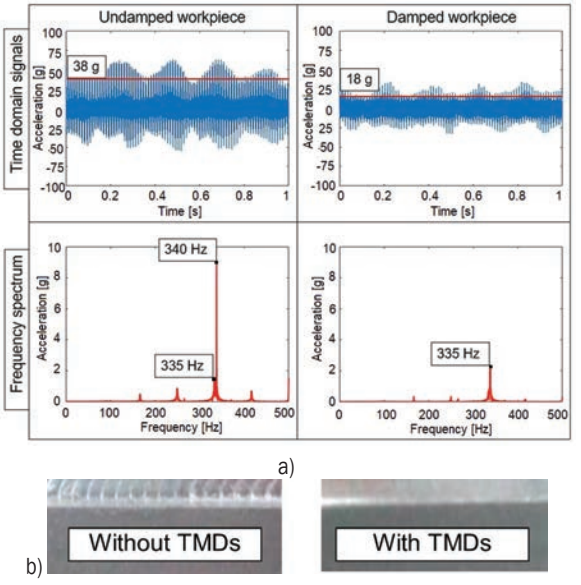

Fig. 19. *Results of experimentation; a) vibration signals obtained during milling tests, and b) surface quality of the machined parts*

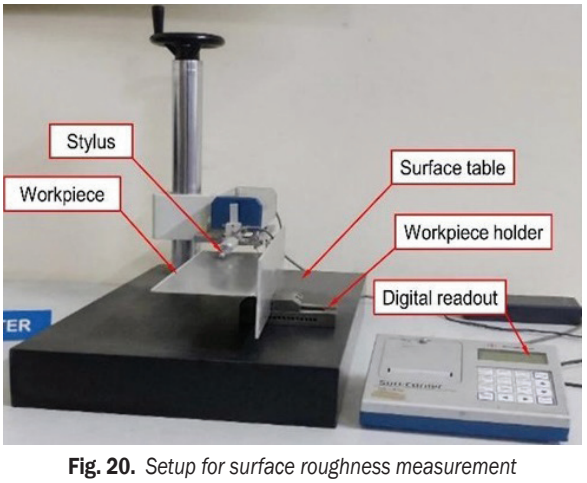

Fig. 20. *Setup for surface roughness measurement*

The average surface roughness (R_a) of the undamped and damped workpieces are found to be 4.24 µm and 2.63 µm, respectively, which correspond to an improvement in surface finish by 38 % .

3 CONCLUSIONS

A novel methodology for optimizing the TMD location towards enhancing chatter suppression in thin-wall milling considering the mass effect of TMDs is presented. The optimization of TMD location is carried out based on a parameterized harmonic analysis aided with a response surface methodology. The effectiveness of the proposed methodology is assessed by plotting SLDs followed by a series of milling tests. The results reveal that chatter in thin-wall milling can be suppressed to a great extent with the proposed approach. The following are the major conclusions drawn from the research work:

- The location of TMD is a crucial factor that influences the dynamic stability of the workpiece at critical mode.
- The optimal X- and Y-coordinates of TMD location for effective chatter suppression of the thin-walled workpiece with dominant mode as torsional mode are about 25 % of the length from either end, and 9 % of the height of the workpiece, respectively.
- Use of a single TMD is found to be effective only for the first half of the cutter path whereas two TMDs are required to improve chatter stability while machining along the entire path.
- Milling tests revealed that the application of TMDs yielded a 6 % improvement in the overall dynamic stability of the workpiece which corresponds to a three-fold improvement in productivity with an enhanced surface finish of 38% .

The above results portray the effectiveness of the proposed method. Even though the method is validated using a simple thin-walled part, it can also be applied to improve the chatter stability of complex thin-wall structures, such as turbine blades, impellers, and other aircraft and automobile parts, where one just needs to design and locate TMDs at their optimum locations.

4 NOMENCLATURES

m	modal mass, [kg]
c	modal damping coefficient, [Ns/m]
k	modal stiffness, [kN/m]
ζ	modal damping ratio, [-]
f_r	frequency ratio, [-]
f_d	frequency of TMD, [Hz]
f_w	frequency of workpiece, [Hz]
Λ	frequency response function, [mm/N]
ω_c	chatter frequency, [rad/s]

K_{tc} tangential cutting force coefficient, [N/mm^2]
K_{rc} radial cutting force coefficient, [N/mm^2]
K_{ac} axial cutting force coefficient, [N/mm^2]
K_{te} tangential edge force coefficient, [N/mm^2]
K_{re} radial edge force coefficient, [N/mm^2]
K_{ae} axial edge force coefficient, [N/mm^2]

5 ACKNOWLEDGEMENTS

The authors would like to express their sincere thanks to the management of PSG College of Technology, Coimbatore and the Office of Principal Scientific Advisor to GoI, New Delhi for providing the necessary facilities for carrying out this research work.

6 REFERENCES

[1] Altintas, Y., Budak, E. (1995). Analytical prediction of stability lobes in milling. *CIRP Annals*, vol. 44, no. 1, p. 357-362, **DOI:10.1016/S0007-8506(07)62342-7**.

[2] Budak, E., Tunç, L.T., Alan, S., Özgüven,H.N. (2012). Prediction of workpiece dynamics and its effects on chatter stability in milling. *CIRP Annals*, vol. 61, no. 1, p. 339-342, **DOI:10.1016/j.cirp.2012.03.144**.

[3] Iglesias, A., Munoa, J., Ciurana, J., Dombóvári, Z., Stépán, G. (2016). Analytical expressions for chatter analysis in milling operations with one dominant mode. *Journal of Sound and Vibration*, vol. 375, p. 403-421, **DOI:10.1016/j.jsv.2016.04.015**.

[4] Yuan, H., Wan, M., Yang, Y., (2019). Design of a tunable mass damper for mitigating vibrations in milling of cylindrical parts. *Chinese Journal of Aeronautics*, vol. 32, no. 3, p. 748-758, **DOI:10.1016/j.cja.2018.12.002**.

[5] Del Sol, I., Rivero, A., López de Lacalle, L.N., Gamez, A.J. (2019). Thin-wall machining of light alloys: A review of models and industrial approaches. *Materials*, vol. 12, no. 12, art. ID 2012, **DOI:10.3390/ma12122012**.

[6] Fei, J., Lin, B., Yan, S., Ding, M., Xiao, J., Zhang, J., Zhang, X., Ji, C., Sui, T. (2017). Chatter mitigation using moving damper. *Journal of Sound and Vibration*, vol. 410, p. 49-63, **DOI:10.1016/j.jsv.2017.08.033**.

[7] Shui, X., Wang, S. (2018). Investigation on a mechanical vibration absorber with tunable piecewise-linear stiffness. *Mechanical Systems and Signal Processing*, vol. 100, p. 330-343, **DOI:10.1016/j.ymssp.2017.05.046**.

[8] Sims, N.D. (2007). Vibration absorbers for chatter suppression: a new analytical tuning methodology. *Journal of Sound and Vibration*, vol. 301, no. 3-5, p. 592-607, **DOI:10.1016/j.jsv.2006.10.020**.

[9] Yang, Y., Muñoa, J., Altintas, Y. (2010). Optimization of multiple tuned mass dampers to suppress machine tool chatter. *International Journal of Machine Tools and Manufacture*, vol. 50, no. 9, p. 834-842, **DOI:10.1016/j.ijmachtools.2010.04.011**.

[10] Yang, Y., Xie, R., Liu, Q. (2017). Design of a passive damper with tunable stiffness and its application in thin-walled part milling. *The International Journal of Advanced Manufacturing Technology*, vol. 89, p. 2713-2720, **DOI:10.1007/s00170-016-9474-7**.

[11] Bolsunovsky, S., Vermel, V., Gubanov, G., Leontiev, A. (2013). Reduction of flexible workpiece vibrations with dynamic support realized as tuned mass damper. *Procedia CIRP*, vol. 8, p. 230-234, **DOI:10.1016/j.procir.2013.06.094**.

[12] Wang, M. (2011). Feasibility study of nonlinear tuned mass damper for machining chatter suppression. *Journal of Sound and Vibration*, vol. 330, no. 9, p. 1917-1930, **DOI:10.1016/j.jsv.2010.10.043**.

[13] Yang, Y., Dai, W., Liu, Q. (2017). Design and machining application of a two-DOF magnetic tuned mass damper. *The International Journal of Advanced Manufacturing Technology*, vol. 89, p. 1635-1643, **DOI:10.1007/s00170-016-9176-1**.

[14] Zhang, Z., Li, H., Liu, X., Zhang, W., Meng, G. (2018). Chatter mitigation for the milling of thin-walled workpiece. *International Journal of Mechanical Sciences*, vol. 138-139, p. 262-271, **DOI:10.1016/j.ijmecsci.2018.02.014**.

[15] Kolluru,K.V., Axinte, D.A., Raffles, M.H., Becker, A.A. (2014). Vibration suppression and coupled interaction study in milling of thin wall casings in the presence of tuned mass dampers. *Proceedings of the Institution of Mechanical Engineers, Part B: Journal of Engineering Manufacture*, vol. 228, no. 6, p. 826-836, **DOI:10.1177/0954405413508769**.

[16] Yang, Y.Q., Chen, T.T. (2012). Numerical solution of tuned mass dampers for optimum milling chatter suppression. *Materials Science Forum*, vol. 697-698, p. 223-228, **DOI:10.4028/www.scientific.net/MSF.697-698.223**.

[17] Burtscher, J., Fleischer, J. (2017). Adaptive tuned mass damper with variable mass for chatter avoidance. *CIRP Annals*, vol. 66, no. 1, p. 397-400, **DOI:10.1016/j.cirp.2017.04.059**.

[18] Schmitz, T.L., Smith, K.S. (2014). Machining Dynamics. Springer, New York, **DOI:10.1007/978-0-387-09645-2**.

Strojniški vestnik - Journal of Mechanical Engineering 68(2022)5, 350-358
DOI:10.5545/sv-jme.2021.7536
Original Scientific Paper
Received for review: 2021-12-30
Received revised form: 2022-02-24
Accepted for publication: 2022-02-24

Fatigue Life Prediction of Butt Weld Joints with Weld Defects at Multiple Locations

Ebron Shaji* Prabhu Raja Venugopal Gautham Velayudhan Mohanraj Selvakumar
PSG College of Technology, Department of Mechanical Engineering, India

A numerical model developed using finite element software is used to determine the fatigue life of an arc-welded butt joint with weld defects: lack of penetration, lack of fusion, and undercut, which occur predominantly in welded structures. High-strength, tempered, and quenched fine grain ASTM A517 grade F structural steel, widely used in welded structures, is selected as the base material. The finite element analysis approach adopted in the present work is validated using the experimental and analytical results by performing a benchmark study. The validated numerical approach is then used to generate datasets for developing an empirical model for predicting the fatigue life of a butt joint with defects, modelled as cracks at specific locations, subjected to bending and/or membrane stresses. An experimental investigation was undertaken to validate the empirical model. The influencing parameters are ranked based on their severity on the fatigue life of butt joint.
Keywords: butt joint, weld defects, fatigue loading, fatigue life

Highlights

- *The present paper takes into consideration the size and location of weld defect in addition to the type of loading and type of weld defect to predict the fatigue life of a butt welded joint.*
- *The analysis revealed that a lack of penetration and undercut lead to minimum fatigue life when the butt joint is subjected to pure membrane stress.*
- *The combined influence of multiple smaller defects at various locations as against a single bigger defect at a particular location in a butt-welded joint is investigated and reported.*
- *A regression model is used to rank the severity of weld defect on the fatigue life of butt weld joint, and an experimental investigation was carried out to validate the above model.*

0 INTRODUCTION

Butt welding is a commonly used joining technique for most of the components that require simpler and strong bonding. The ASTM A517 grade F structural steel is selected as the base material for the present study, since it is used widely in welded structures in all kinds of applications [1] to [3], such as pressure vessels, transport vehicles, bridges, hoisting, and earthmoving equipment.

Welding is a major factor in the fatigue life reduction of any large structure. In fillet welded joints, stress concentration occurs at the weld toe, weld root and between the base and weld metal [4] to [6]. The above zones with higher stress concentration are more likely to initiate cracks when subjected to dynamic loads. Even though the fatigue properties of the weld metal are good, failure can be caused by the existence of weld defects, such as lack of penetration, lack of fusion, undercut, and porosity. In a single-pass, butt-welded joint, a lack of penetration (LOP) occurs at the root of weldment, lack of fusion (LOF) occurs between the surfaces of weldment and base plate, and undercut (UC) occurs at the weld toe [7]. Porosity will be commonly found close to the upper surface of weld reinforcement. Under fatigue loading, a crack may be initiated from the weld defect and the propagation of such a crack in weldment is likely to result in the failure of the joint. In the presence of weld defects, the crack initiation period is shorter relative to the crack propagation period [8]. A weldment with a defect is considered to be a notched component, and the crack initiation life can be predicted using a local stress-strain approach. The crack propagation life depends on the growth rate of the crack from its initial size to the critical size; it can be predicted by means of stress intensity factor (SIF) at the crack tip [9]. Even though equations are provided in SIF data-books for obtaining solutions for simpler weld joints, it is challenging to obtain adequate solutions for structures with different weld configurations involving complex geometry and loading conditions [10] and [11].

The present study takes into consideration the presence of weld defects at different locations in addition to the type of loading, type of weld defect, and size of defect for analysis. The weld defects are modelled as semi-elliptical cracks based on the recommendations made by the IIW for the fatigue design of welded joints and components [11]. The stress intensity factor in the proximity of weld defect

*Corr. Author's Address: PSG College of Technology, Peelamedu, Coimbatore, India, 1601rm01@psgtech.ac.in

is evaluated with M-integral and the corresponding propagation life is calculated using the Paris law with the aid of fracture analysis (FRANC3D) software. The main objective of the work is to predict and rank the severity of weld defects on the fatigue life of a butt-welded joint shown in Fig. 1, considering defects at three locations (CL_1, CL_2, CL_3).

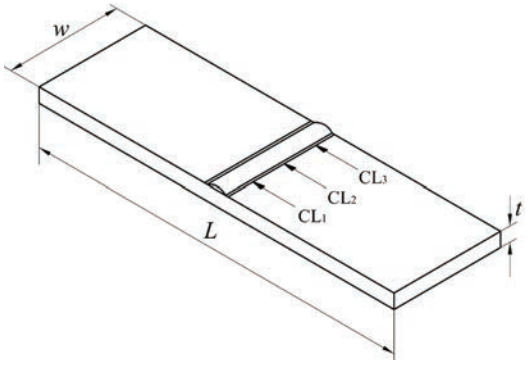

Fig. 1. *Crack locations in butt-welded joint*

1 BENCHMARK STUDY

Prior to performing the finite element analysis of a butt-welded joint with weld defect, a benchmark study considering a cruciform joint, with LOP defect, subjected to repeated tensile load (Fig. 2) is undertaken. The fatigue life corresponding to the failure of cruciform joint is determined using analytical and numerical methods and the same is compared with the experimental results presented by Balasubramanian and Guha [12].

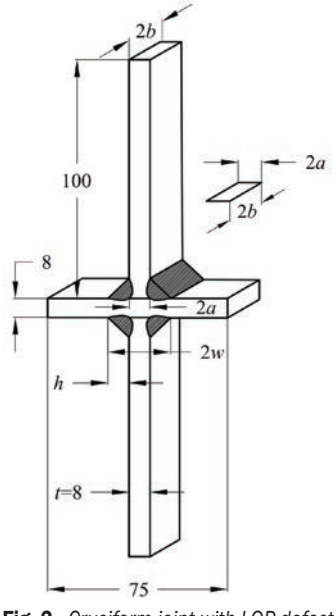

Fig. 2. *Cruciform joint with LOP defect*

The stress intensity at the crack tip is determined analytically by employing Eq. (3) proposed by Frank and Fisher [13] and numerically using FRANC3D software by modelling the LOP defect as a double-edge crack [11] and performing crack propagation analysis. The corresponding fatigue life is then calculated by using the Paris Erdogan law given by Eq. (2) [14] and [15].

$$K = \frac{\sigma\left(A_1 + A_2\frac{a}{w}\right)\left(\pi a \sec\left(\pi\frac{a}{2w}\right)\right)}{1+2\frac{h}{t}}, \qquad (3)$$

$$A_1 = 0.528 + 3.287\frac{h}{t} - 4.361\frac{h^2}{t} + 3.696\frac{h^3}{t} - 1.875\frac{h^4}{t} + 0.415\frac{h^5}{t},$$

$$A_2 = 0.218 + 2.717\frac{h}{t} - 10.171\frac{h^2}{t} + 13.122\frac{h^3}{t} - 7.755\frac{h^4}{t} + 1.783\frac{h^5}{t},$$

where σ is the normal stress range

$$w = h + \frac{t}{2}.$$

The above equation for stress intensity factor K is valid for the range of,

$$0.2 \le \frac{h}{t} \le 1.2 \quad \text{and} \quad 0.1 \le \frac{a}{w} \le 0.7.$$

$$\frac{da}{dN} = C(\Delta K)^m, \qquad (2)$$

where C and m are Paris constants.

The experimental investigation [12] was carried out for both single-pass and double-pass welding considering various h/t ratios for the joint made of ASTM A3 grade F, at different stress levels. For the current benchmark study, a cruciform joint of $h/t = 1$ with LOP of 7 mm and subjected to 20 MPa is considered. The corresponding fracture parameters [12] considered are as follows: fracture threshold ΔK_{th} of 126 MPa√mm, fracture toughness ΔK_{cr} of 8 MPa√mm, and Paris constants ($C = 2.0 \times 10^{-4}$, $m = 3.4$).

Using an analytical approach, the initial SIF (ΔK_o) corresponding to the initial defect is determined as 256 MPa√mm. The size of defect is increased incrementally until the SIF reaches the fracture toughness of the material ($\Delta K_{cr} = 1581$ MPa√mm), and the corresponding critical crack length is found to be 20.8 mm. Using Eq. (2), the corresponding fatigue life of the joint is calculated as 1.25×10^6 cycles.

As regards the numerical approach, a finite element model of the joint with defect is made using Brick 8 node 185 elements using Ansys software, as shown in Fig. 3a, and the fatigue life is determined using FranC3D software. The bottom end of the vertical plate of the cruciform joint is fully constrained and the load corresponding to a stress level of 210 MPa at weld zone is applied at the top end, and the principal stress distribution (Fig. 3b) is obtained.

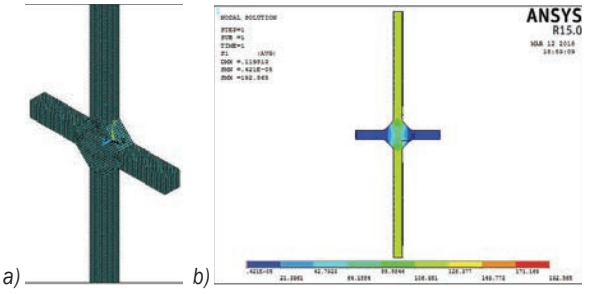

Fig. 3. *Cruciform joint; a) finite element model, and b) stress plot*

After performing stress analysis using Ansys software, the finite element model along with nodal displacements is imported into FranC3D software.

A double edge crack of length $2a$ = 7 mm and b = 8 mm is modelled and incorporated at LOP location in the weldment as shown in Fig. 4a. FranC3D uses an adaptive meshing technique, which allows fine mesh at the crack tip and coarse mesh at other geometric locations; therefore, mesh convergence is automatically taken care of. Static crack analysis predicts the initial SIF (ΔK_o) as 287 MPa√mm at the crack front of double edge crack. Furthermore, the crack was propagated at the rate of 0.3 mm until it reached the critical SIF value (1581 MPa√mm) as shown in Fig. 5. The finite element analysis (FEA) predicts the exact propagation path (Fig. 4b) in comparison to the experimentally determined path [12] and the fatigue life corresponding to the critical crack length is found to be 1.17 × 10^6 cycles.

Table 1. *Fatigue life of cruciform joint*

	Initial SIF ΔK_o [MPa√mm]	CI Life [×10^6 cycles]	CP Life [×10^6 cycles]	Total life [×10^6 cycles]
By analytical approach	282	-	1.25	-
By FEA	287	-	1.17	-
By expt. [12]	253	0.6	1.32	1.92

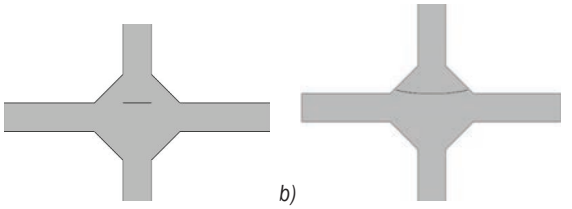

Fig. 4. *Crack propagation path; a) before propagation, and b) after propagation*

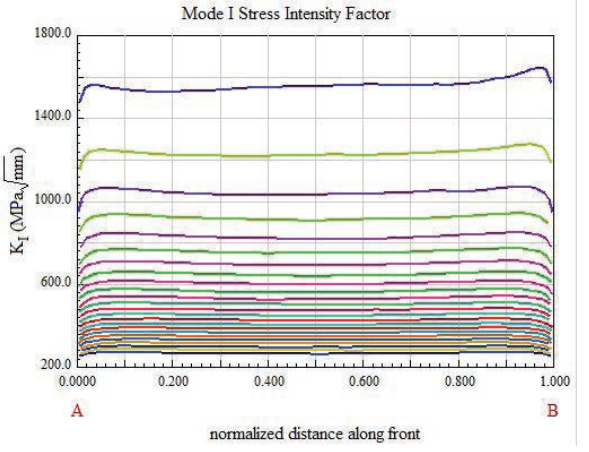

Fig. 5. *SIF along the crack front*

As shown in Fig. 6, the comparison plot shows good agreement between numerical and analytical solutions with a maximum deviation of 6.4 %. The numerical approach predicts the fatigue life with a deviation of 11 % compared to the experimental determination [12].

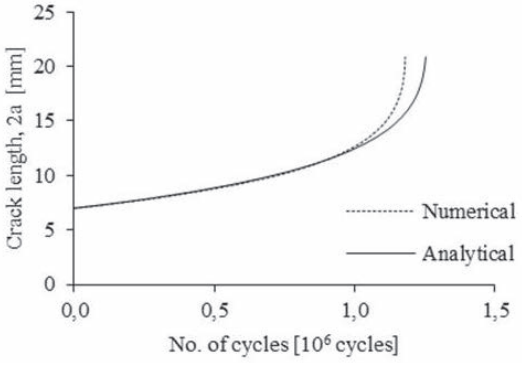

Fig. 6. *Comparison of crack propagation life of a cruciform joint*

Hence, the validated numerical approach is extended to predict the fatigue life of butt joint when the same is subjected to a combination of membrane and bending loads in the presence of weld defects at three locations.

2 FATIGUE LIFE PREDICTION OF A BUTT JOINT CONSIDERING WELD DEFECTS

The plate with the butt-welded joint is considered for the present study (Fig. 1). The material considered is ASTM A36 grade F steel for the plate as well as the weldment. In an in-depth approach, a hypothetical assumption is made to postulate defects with the assumption of severe violation of manufacturing standards.

The three major weld defects considered for the present investigation are lack of penetration [LOP], lack of fusion [LOF], and undercut as shown in Fig. 7. LOP happens when the metal groove is not entirely filled, with weld metal throughout joint thickness. LOP occurs because of improper edge preparation.

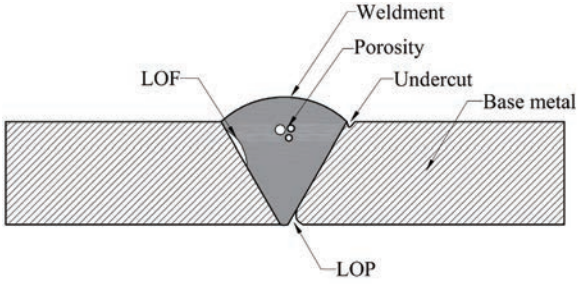

Fig. 7. *Types of weld defect*

LOF occur when there is an improper fusion between the metal and weld. This produces a gap inside the joint that is not filled with molten metal. A major cause of LOF is contamination of metal surface and use of low heat input. Undercut occurs at weld toe region because of an incorrect electrode angle and too high weld current. These defects will affect the fatigue strength of weld joint, which leads to joint failure. To rank the severity of these weld defects on the fatigue life of a butt-welded joint with respect to loading and position of defect, the following analysis is carried out.

The total length (L) of the two plates considered for analysis is 200 mm. The plate width (w) and plate thickness (t) are considered 60 mm and 8 mm, respectively. The initial dimensions of the weld defect LOP and LOF correspond to the length and depth are 152 mm and 1.6 mm, respectively. For undercut the values are 152 mm and 2 mm, respectively, as mentioned in Table 2. The initial weld defect dimensions are considered with respect to the maximum acceptable value mentioned as in the acceptance criteria for welds ASME B31.3 [16].

The above weld defects are modelled as equivalent cracks in the weld zones [11], and the crack growth behaviour is simulated using FRANC3D software. An initial non-cohesive semi-elliptical crack was placed in the finite element model depending upon the type of weld defect, as shown in Fig. 8. An adaptive mesh is auto-generated after incorporating the initial crack with appropriate dimensions and the fatigue life is estimated by performing crack propagation analysis. Fig. 9 shows the results of numerical simulation of crack propagation in a butt-welded joint.

Table 2. *Acceptance criteria - ASME B31.3 for weld defects*

Weld defect	Initial crack		Occurrence
	Length	Depth	
Lack of penetration	(38/150) w	0.20 t	Weld root
Lack of fusion	(38/150) w	0.20 t	Weld toe (Oriented to bead angle)
Undercut	(38/150) w	0.25 t	Weld toe

Fig. 8. *Finite element model of butt joint*

The simulation indicates the extent of crack propagation from top to bottom surface of the butt joint for lack of fusion and undercut and vice-versa for lack of penetration. The fatigue life corresponds to the number of cycles applied until the crack depth tends to approach plate thickness, where the crack becomes asymptotic.

Although LOF and undercut are modelled as cracks of the same dimensions, their position and orientation are different, as shown in Fig. 7. Therefore, LOF and undercut are likely to have a varying influence on fatigue life.

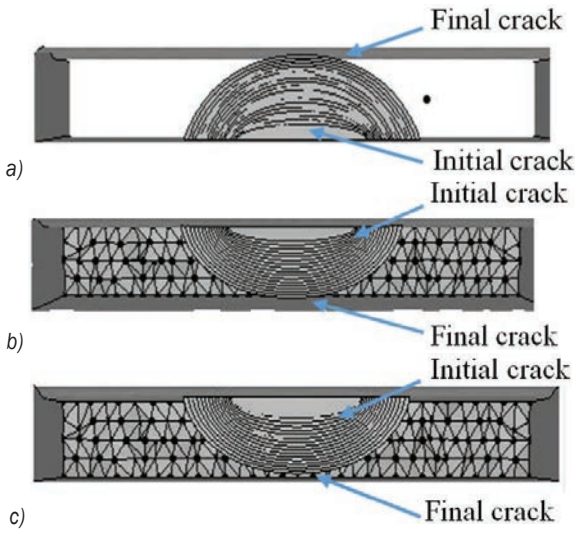

Fig. 9. *Numerical simulation of crack propagation in butt-weld joint; a) propagation of crack originating from LOP, b) propagation of crack originating from LOF, and c) propagation of crack originating from undercut*

3 TAGUCHI DESIGN FOR PREDICTION OF FATIGUE LIFE

Since the problem under consideration has a wide range of variables, a five-factor, three-level factorial design matrix was selected based on Taguchi design. The experimental design matrix contains the factors, viz., type of load (A), type of defect (B), Crack1 (C), Crack2 (D) and Crack3 (E) at specific locations with their corresponding levels as shown in Table 3

Table 3. *Control factors and their selected levels*

	Control factor	Level		
		1	2	3
A	Type of load	L1	L2	L3
B	Type of defect	LOP	LOF	UC
C	Location for Crack 1	CL1	CL2	CL3
D	Location for Crack 2	CL1	CL2	CL3
E	Location for Crack 3	CL1	CL2	CL3

Fig. 10 shows the stress distribution when the specimen is subjected to membrane load (P_m) and bending load (P_b) individually and as a combination of the above loads ($P_m + P_b$). On applying bending load in an upward direction, q lack of fusion will not have considerable influence on crack propagation in the top surface as it is subjected to compressive stress.

Similarly, for bending load in a downward direction, a lack of penetration will not have considerable influence on crack propagation. However, the high cyclic fatigue failure will occur at stress lesser than half the ultimate stress. Hence, the load applied on the plate corresponds to a normal stress of 120 MPa, which will aid in crack propagation analysis [17] and [18]; the same is considered while formulating the design matrix.

The specimen is fixed at one end, and a repeated load (zero to peak stress and back to zero) is applied with appropriate kinematic constraints for simulation to ensure that the plane section remains flat before and after application of load. Three types of repeated load (zero to peak stress and back to zero) considered for analysis are given below:

L1: Peak stress = 120 MPa (membrane),
L2: Peak stress = 60 MPa (membrane) + 60 MPa (tensile stress due to positive bending moment),
L3: Peak stress = 60 MPa (membrane) + 60 MPa (compressive stress due to negative bending moment).

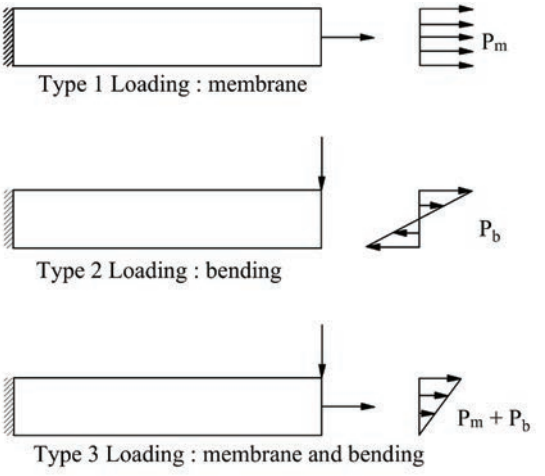

Fig. 10. *Types of loading on butt weld joint*

4 RANKING THE SEVERITY OF WELD DEFECTS ON FATIGUE LIFE

Based on the control factors and levels shown in Table 3, a design matrix is arrived with different datasets. The fatigue life of butt-joint is determined for each dataset in the design matrix by using simulation software (Franc3D) as shown in Table 4.

Considering the presence of three cracks (i.e., Crack1, Crack2 and Crack3) at the same location (CL1) as an example (Table 3), it implies that a bigger crack with thrice the dimensions of a single crack is incorporated in the finite element model for analysis. Since a higher fatigue life is desirable, the signal-to-noise ratio (S/N) is determined by using the criteria "larger is better", as shown in Table 5. To determine the fatigue life of butt-weld joint, a quadratic

mathematical model of the second order is developed. The chosen empirical formula accounts for the influence of individual factors and their interactions. The empirical Eq. (3) obtained at 95 % confidence level using MINITAB statistical software is given in Eq. (3).

Table 4. *Design of experiments and results*

Type of load	Type of defect	Crack location			Fatigue life [cycles]
		Crack1	Crack2	Crack3	
L1	LOP	CL1	CL1	CL1	137511
L1	LOP	CL1	CL1	CL2	253440
L1	LOP	CL1	CL1	CL3	264217
L1	LOF	CL2	CL2	CL1	324471
L1	LOF	CL2	CL2	CL2	211396
L1	LOF	CL2	CL2	CL3	378649
L1	UC	CL3	CL3	CL1	218589
L1	UC	CL3	CL3	CL2	252548
L1	UC	CL3	CL3	CL3	127441
L2	LOP	CL2	CL3	CL1	907636
L2	LOP	CL2	CL3	CL2	572106
L2	LOP	CL2	CL3	CL3	557734
L2	LOF	CL3	CL1	CL1	378091
L2	LOF	CL3	CL1	CL2	484553
L2	LOF	CL3	CL1	CL3	381541
L2	UC	CL1	CL2	CL1	288604
L2	UC	CL1	CL2	CL2	334500
L2	UC	CL1	CL2	CL3	450367
L3	LOP	CL3	CL2	CL1	298335
L3	LOP	CL3	CL2	CL2	207791
L3	LOP	CL3	CL2	CL3	198583
L3	LOF	CL1	CL3	CL1	496818
L3	LOF	CL1	CL3	CL2	648794
L3	LOF	CL1	CL3	CL3	472327
L3	UC	CL2	CL1	CL1	364090
L3	UC	CL2	CL1	CL2	354164
L3	UC	CL2	CL1	CL3	532533

$$\begin{aligned} \textit{Fatigue life} = {} & -6\,19 + 10\,06\,A - 1\,8\,B \\ & + 0\,91\,C - 2\,7\,D - 8\,3\,E \\ & - 2\,40\,A\times A - 4\,3\,B\times B - 9\,0\times C\times C \\ & + 0\,6\,D\times D + 4\,6\times E\times E - 9\times A\times E \\ & + 0\,7\,B\times E - 1\,4\,C\times E - 2\,2\,D\times E \\ & + 4\,0\,A\times A\times E - 8\times A\times B\times E \\ & + 1\,7\times A\times C\times E - 2\,4\,A\times E\times E \\ & - 3\,0\times B\times B\times E - 6\times B\times E\times E \\ & + 6\,C\times E\times E - 3\,D\times E\times E. \end{aligned} \quad (3)$$

The average S/N ratio and the average fatigue life for each factor at every level are obtained. Subsequently, delta values are computed, and the factors that influence the fatigue life are ranked as shown in Table 5. It is inferred from the table that the type of load has the largest effect on S/N ratio among the control factors considered. Furthermore, L_1 is found to have lower S/N ratio than the other two types of load, which implies that L_1 is more critical.

Table 5. *S/N ratio on fatigue life*

Level	Type of load	Type of defect	Crack location		
			Crack 1	Crack 2	Crack 3
1	107.2	110	110.6	110.3	110.5
2	113.2	112.1	112.7	109.2	110.6
3	111.4	109.6	108.4	112.2	110.6
Delta	6	2.5	4.3	3	0.2
Rank	1	4	2	3	5

Next, it is required to determine the effect of weld defect on fatigue life, considering the critical load type (L_1) by referring to Table 4. It is inferred from the table that two cases result in minimum fatigue life owing to the maximum severity of weld defect; lack of penetration leading to 37 1 cycles and undercut leading to 27441 cycles, where either of the defects is concentrated at a single location.

The next level of severity pertaining to crack location is assessed by referring to Table 4, where the values of fatigue life are 8 cycles and 2804 cycles. The fatigue life of 8 cycles corresponds to lack of penetration, where the concentration of weld defect in terms of crack size at CL_3 is twice that of a single crack at CL_2. Similarly, the fatigue life of 2804 cycles corresponds to undercut, where the concentration of weld defect in terms of crack size at CL_1 is twice that of a single crack at CL_2. The lack of fusion is found to have a lesser influence towards reducing the fatigue life of butt welded joint.

In general, referring to Table 5, it is found that a bigger crack at a single location (rank 2) has more influence than relatively smaller cracks at multiple locations (rank 3 and rank 5).

5 EXPERIMENTAL VALIDATION OF THE EMPIRICAL MODEL

By performing numerical analysis and subsequently adapting an empirical model for ranking the severity of weld defects on fatigue life of butt joint, it is found that undercut has more influence on fatigue life under tensile loading. To validate the empirical model, a typical dataset (L_1, UC, CL_2, CL_2, CL_2) is considered for experimental investigation. A BISS (Bangalore Integrated System Solutions) 6 kN hydraulic actuator with a maximum frequency of 20 Hz was used to propagate the crack in butt weld joint.

Two plates (0 mm × 0 mm × 2 mm) made of ASTM A5 grade F were welded together to form a butt joint, which was considered for numerical analysis; an additional length of 0 mm was provided at the ends to facilitate the clamping of specimen. The centre portion of the plate was reduced to a thickness of 8 mm by milling to obtain the desired stress level in the weld zone. An equivalent notch that represents undercut was made at the mid-location CL_2 by using a 0.5 mm metal cutting wheel. The specimen was held in a fixture using dowel pins and the fixture was connected between the actuator head and base plate by bolted connection as shown in Fig. 11. The butt-welded specimen with a notch of length 15 mm and depth 1.6 mm was preloaded by applying a force of 0.1 kN in the vertical direction to eliminate free play. To initiate crack at notch tip, the specimen was subjected to high cycle fatigue at a frequency of 5 Hz. A stress level of 0 MPa was maintained at the notch tip to avoid plastic deformation.

Fig. 11. *Butt joint under fatigue loading*

At the notch tip, dye penetrant testing as shown in Fig. 2a was carried out for every 0,000 cycles to monitor the crack growth behaviour. After a period of 1.1 × 10^5 cycles, a visible crack of 0.5 mm was identified at the notch tip. Furthermore, to propagate the crack, the specimen was subjected to low-cycle fatigue by increasing the stress level to 20 MPa. The loading frequency was maintained at 1 Hz to maintain the rate of propagation in a controlled manner. The propagation of crack was measured for every 0,000 cycles using a crack depth gauge; the corresponding crack length was plotted as shown in Fig. 3.

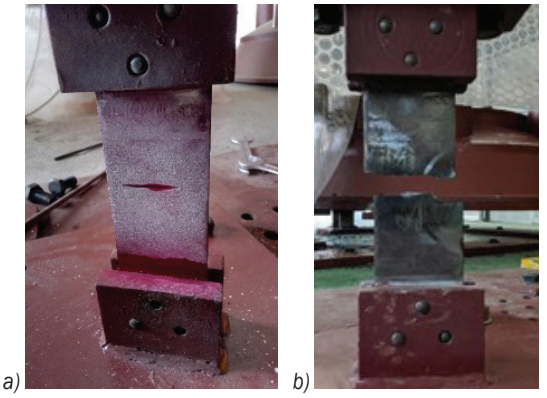

Fig. 12. *Butt-welded joint; a) initial notch, and b) fractured specimen*

It is evident from the crack growth curve that the specimen fractured at 1.3 × 0 ^{5} cycles. For the same dataset (L_1, UC, CL_2, CL_2, CL_2), the fatigue life of butt joint is estimated using the empirical model and the numerical technique. The corresponding fatigue lives are found to be 1.8 × 0 ^{5} and 1.7 × 0 ^{5} cycles, respectively.

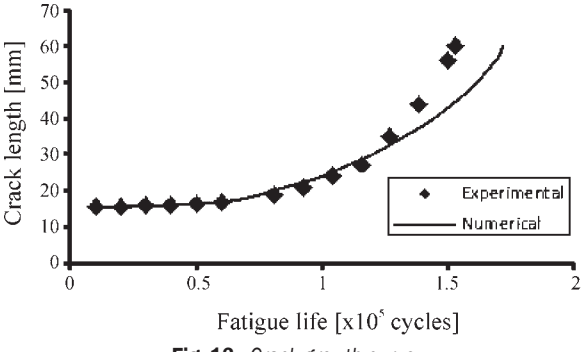

Fig. 13. *Crack growth curve*

The experimental determination shows 4 % deviation of fatigue life predicted by the empirical model, which accounts the deviation of 4 % between the prediction of numerical and empirical model. This gives more confidence on numerical procedure and the empirical model to determine the crack propagation life.

6 CONCLUSIONS

A systematic analysis of a butt weld joint using FEA was undertaken by incorporating weld defects as equivalent cracks and propagating them until they

become through-wall cracks. The number of cycles taken for an initial crack to become a through-wall crack is estimated as the fatigue life of a butt-weld joint. The numerical model of cruciform joint with LOP defect was validated using an analytical equation and experimental results found in the literature.

A Taguchi experimental design was employed to determine the extent of severity of weld defects at multiple locations on the fatigue life of the butt-weld joint subjected to membrane and bending stresses. The lack of penetration and undercut were found to result in minimum fatigue life, when the joint is subjected to pure membrane stress rather than a combination of membrane and bending stresses.

In the presence of multiple defects in the butt-welded joint, the combined influence of three defects followed by two defects at either one-fourth or three-fourth locations along the length of weld is found to significantly reduce the fatigue life, more so than the presence of defect at mid-span of weldment. Also, compared to smaller multiple defects, a single defect of combined size of multiple cracks has more influence on the fatigue life of a butt weld joint. While ranking the weld defects based on severity, LOP has the highest influence on fatigue life, while undercut is marginally less severe. The least severe type of defect on fatigue life is found to be lack of fusion.

In the present work, stress is taken as the driving parameter and not the applied load. Furthermore, the defects are parametrically modelled and hence the size of defects is proportional to geometric dimensions of plate. Therefore, the results are geometry independent and are quite generic.

7 ACKNOWLEDGEMENTS

The research described in this paper was financially supported by the Board of Research in Nuclear Science (BRNS), Mumbai, India (Sanction No. 2)/1/ 9 201-BRNS/19). The authors are indebted to Board of Research in Nuclear Science (BRNS), Mumbai and Indra Gandhi Centre for Atomic Research (IGCAR), Kalpakkam, Tamil Nadu for their support throughout the investigation of this work. The authors sincerely acknowledge the technical support and valuable inputs provided by Dr P. Chellapandi, Former Director, Safety Group and Former Associate Director, Nuclear Engineering Group, IGCAR, Kalpakkam.

8 REFERENCES

[1] Cai, S., Chen, W., Kashani, M.M., Vardanega, P.J., Taylor, C.A. (2017). Fatigue life assessment of large scale T-jointed steel truss bridge components. *Journal of Constructional Steel Research*, vol. 133, p. 499-509, **DOI:10.1016/j.jcsr.2017.01.008**.

[2] Schijve, J. (ed.) (2009). *Fatigue of Structures and Materials*. Springer, Dordrecht, **DOI:10.1007/978-1-4020-6808-9**.

[3] Hyde, T.R., Leen, S.B., McColl, I.R. (2008). A methodology for modelling the effects of nitriding on fatigue life. *Proceedings of the Institution of Mechanical Engineers, Part L: Journal of Materials: Design and Applications*, vol. 222, no. 1, p. 1-14. **DOI:10.1243/14644207JMDA145**.

[4] Fuštar, B., Lukačević, I., Dujmović, D. (2018). Review of fatigue assessment methods for welded steel structures, *Advances in Civil Engineering*, vol. 2018, art. ID 3597356, **DOI:10.1155/2018/3597356**.

[5] Razavi, S.M.J., Ayatollahi, M.R., Samari, M., da Silva, L.M.F. (2019). Effect of interface non-flatness on the fatigue behavior of adhesively bonded single lap joints. *Proceedings of the Institution of Mechanical Engineers, Part L: Journal of Materials: Design and Applications*, vol. 233, no. 7, p. 1277-1286, **DOI:10.1177/1464420717739551**.

[6] Schütz, W. (1996). A history of fatigue. *Engineering Fracture Mechanics*, vol. 54, no. 2, p. 263-300, **DOI:10.1016/0013-7944(95)00178-6**.

[7] Al-Mukhtar, A.M., Henkel, S. (2009). A finite element calculation of stress intensity factors of cruciform and butt welded joints for some geometrical parameters. *Jordan Journal of Mechanical and Industrial Engineering*, vol. 3, no. 4, p. 236-245.

[8] Ottersbock, M.J., Leitner, M., Stoschka, M., Maurer, W. (2019). Crack Initiation and Propagation Fatigue Life of Ultra High-Strength Steel Butt Joints. *Applied Sciences*, vol. 9, no. 21, p. 1-28, art. ID 4590, **DOI:10.3390/app9214590**.

[9] Baumgartner, J., Waterkotte, R. (2015). Crack initiation and propagation analysis at welds-Assessing the total fatigue life of complex structures. *Materialwissenschaft und Werkstofftechnik*, vol. 46, no. 2, p. 123-135, **DOI:10.1002/mawe.201400367**.

[10] Newman, J., Raju, I. (1984). Stress-intensity factor equations for cracks in three-dimensional finite bodies subjected to tension and bending loads. *NASA Technical Memorandum*, 85793, p. 1-40, NASA Research Center, Hampton.

[11] Hobbacher, A.F. (2009). The new IIW recommendations for fatigue assessment of welded joints and components - A comprehensive code recently updated. *International Journal of Fatigue*, vol. 31, no. 1, p. 50-58, **DOI:10.1016/j.ijfatigue.2008.04.002**.

[12] Balasubramanian, V., Guha, B. (1999). Influence of weld size on fatigue crack growth characteristics of flux cored arc welded cruciform joints. *Materials Science and Engineering*, vol. A265, p. 7-17, **DOI:10.1016/S0921-5093(99)00007-6**.

[13] Frank, K.H., Fisher, J.W. (1979). Fatigue strength of fillet welded cruciform joints. *Journal of the Structural Division*, vol. 105, no. 9, p. 1727-1740, **DOI:10.1061/JSDEAG.0005226**.

[14] Paris, P., Erdogan, F. (1963). Critical analysis of crack propagation laws. *Journal of Fluids Engineering, Transactions of ASME*, vol. 85, no. 4, p. 528-533, **DOI:10.1115/1.3656900**.

[15] Alvesa, A.S.F., Sampayo, L., Correia, J.A.F.O., De Jesus, A.M.P., Moreira, P.M.G.P., Tavares, P.J.S. (2015). Fatigue life

prediction based on crack growth analysis using an equivalent initial flaw size model: *Application to a notched geometry. Procedia Engineering*, vol. 114, p. 730-737, **DOI:10.1016/j.proeng.2015.08.018**.

[16] Process Piping (2020). *ASME Code for Pressure Piping*, B31.3. American Society of Mechanical Engineers, New York.

[17] Chapetti, M.D., Jaureguizahar, L.F. (2011). Estimating the fatigue behaviour of welded joints. *Procedia Engineering*, vol. 10, p. 959-964, **DOI:10.1016/j.proeng.2011.04.158**.

[18] Lotsberg, I. (2009). Fatigue capacity of load carrying fillet-welded connections subjected to axial and shear loading. *Journal of Offshore Mechanics and Arctic Engineering*, vol. 131, no. 4, art. ID 041302, **DOI:10.1115/1.3160531**.

Strojniški vestnik - Journal of Mechanical Engineering 68(2022)5, 359-367
DOI:10.5545/sv-jme.2021.7466
Original Scientific Paper
Received for review: 2021-11-11
Received revised form: 2022-03-14
Accepted for publication: 2022-03-28

Multi-Response Optimization of the Tribological Behaviour of PTFE-Based Composites via Taguchi Grey Relational Analysis

Musa Alhaji Ibrahim[1,2,*] – Hüseyin Çamur[2] – Mahmut A. Savaş[2] – Alhassan Kawu Sabo[3]

[1] Kano University of Science and Technology, Faculty of Engineering, Nigeria
[2] Near East University, Faculty of Engineering, Cyprus
[3] Kano University of Science and Technology, Physical Planning and Development Unit, Nigeria

Polymer-based composites find applications in several areas because of their exceptional properties. This article deals with Taguchi grey relational optimization method of abrasive parameters (load (L), grit size (G) and sliding distance (D)) and their influence on abrasive performance of reinforced polytetrafluoroethylene (PTFE) composites. A Taguchi L_9 orthogonal array was designed, and nine experimental tests were conducted based on the Taguchi designed experiments. A pin-on-disc tribology machine was used for the experiments. The coefficient of friction (μ) and abrasive specific wear rate (A_w) were recorded for each experiment. An analysis of variance (ANOVA) was performed to establish the significance and percentage contribution of each parameter affecting the abrasive wear performance. Results from the Taguchi-grey-relational method showed that the optimal combination of parameters was achieved at load of 10 N, grit size of 1000 mesh, and sliding distance of 350 m (coded as L3G1D3). ANOVA findings revealed that a grit size with 67.69 % as the most influential on the abrasive performance of polymer-based composites. Validation tests performed using the optimal combination parameter showed an enhancement of 55.22 % in grey relational grade.

Keywords: PTFE, carbon fibre, bronze fibre, abrasive, Taguchi, grey relational analysis

Highlights

- *Optimization of abrasive tribological performance of PTFE based composites has been performed.*
- *Influence of load, grit size and sliding distance on coefficient of friction (μ) and specific abrasive wear rate (Aw) were studied.*
- *Optimization of multiple responses of μ and Aw via Taguchi-grey relational method is presented.*
- *Analysis of variance performed to find the most significant parameter on Taguchi grey relational grade.*
- *Optimal parameters found to be load and sliding distance at their third levels while grit size at its first level.*
- *According to the order of significance and percentage, the contribution on and to grey relational grades in abrasive performance is enumerated as grit size, load, and sliding distance.*

0 INTRODUCTION

Polymer matrix composites (PMCs) are used in the automotive and aerospace sectors because of their high strength and stiffness [1]. Polytetrafluoroethylene (PTFE) is a commonly used matrix due to its antifriction property, water and chemical resistance, thermal stability, and low cost [2] to [4]. However, PTFE shows poor wear properties. It is reinforced with fibres including glass, carbon, aramid and bronze fibres to improve the wear properties [5]. PTFE and its composites are exposed to abrasive action and used in highly abrasive environments. The wear rate and coefficient of friction (μ) of PMCs are not inherent material properties and strongly rely on the system where the system will operate [6] and [7].

Experimental studies showed that reinforcing matrices with fibres improve their wear rate. Suresha and Kumar [8] reinforced PA6 PP with nano-clay and short carbon fibres. Improvement in wear rate of the PA6 PP matrix was observed. In their study of abrasive property of different polymers, Shipway and Ngao [9] showed that polymers exhibited different behaviours and concluded that the abrasive wear of polymer depends on the type of the polymer. Ravi Kumar et al. [10] studied the abrasive wear rate of glass and carbon fabric reinforced vinyl/ester composites. The results showed that vinyl/ester reinforced with carbon had lower abrasion compared to glass reinforced vinyl/ester composite and that increasing the distance decreased the abrasion. Liu et al. [11] studied abrasive performance of a filled UHMWPE matrix and found that the applied load was most significant process variable. Yousif et al. [12] studied the abrasion resistance of betelnut-filled epoxy composite. It was revealed that rougher particles and high velocity generated high μ and wear rate, respectively. Harsha and Tewari [13] studied the influence of glass fibre at different loadings, sliding distance, load, and grit size on polysulfone. The results revealed a deterioration in abrasive performance of the polysulfone. Moreover, decreasing and increasing trends of tribological behaviour were observed due to varying load, distance, speed and grit size.

The single response optimization Taguchi method has been used for the tribological performance of

*Corr. Author's Address: Kano University of Science and Technology/Near East University, Wudil. Kano/Nicosia, Nigeria/Cyprus, musaibrahim@kustwudil.edu.ng

PMCs. Thakur and Chauchan [14] studied the wear and friction behaviour of submicron size cenosphere particle-reinforced vinyl ester composites using Taguchi L_{27}. Load, roughness, filler size, speed, and distance (each at three levels) were considered as parameters controlling the tribological behaviour of the vinyl ester composite. Different optimal combinations of parameters for desired μ and A_w were found for the two responses. ANOVA showed that load at 63 % and 69 % was the most significant factor controlling the μ and A_w. Pogosian, Cho, and Bahadur [15] used the Taguchi method to optimize polyphenylene sulphide reinforced with MoS_2, Al_2O_3 particles. The optimal Taguchi combination of parameters was found to be PPS+7 % Vol. MoS_2 +10 % Vol. PTFE, speed 1.5 ms^{-1} and roughness 0.1 μm for minimum wear rate. ANOVA indicated that MoS_2 exhibited the greatest effect on wear rate of the composites. Chang et al. [16] optimized load, distance, counterface roughness, and amount of fibre as parameters influencing the abrasive wear of kenaf-reinforced polyester composite via Taguchi $L_9(3^4)$. The results showed that the optimal combination for minimum wear was obtained at a load of 10 N, composition B, and distance 2,000 m and that applied load was the most influential parameter on wear rate. Şahin [1] optimized control the factors of abrasive wear of glass- and carbon-reinforced PTFE composites through the Taguchi method. Load, grit size, distance, and compressive strength were the investigated parameters. For minimum volume loss, it was found that a load of 5 N, a grit size of 200 mesh, a distance of 45 m, and a compressive strength of 98 MPa were the optimal parameters.

To study multiple responses related to tribological behaviours of composites, several decision-making methods, including data envelopment analysis (DEA), analytic hierarchy process (AHP), and grey relational analysis (GRA) have been proposed. Of these, GRA, introduced by Deng in 89 [17], is the most commonly used when the nature of the information is uncertain and incomplete. Ramesh and Suresha [18] integrated Taguchi with the grey relational method to establish the optimal levels of abrasive performance of carbon-epoxy hybrid composites. It was found that grit size and filler loading were the most influential parameters. Based on the Taguchi-grey relational analysis, Subbaya et al. [19] investigated the wear assessment of SiC-filled epoxy composites; the results showed that the optimal combination for minimum wear was obtained at filler content of 10 wt. %, grit size of 320 mesh, load of 10 N, and distance of 75 m. Filler with 0.09 % was the found to be most significant parameter influencing the GRG. Dharmalingam et al. [20] combined Taguchi with GRA to determine the optimal parameter settings of multiple responses of abrasive wear aluminium hybrid metal composites. The optimal parameters were found to be load of 20 N, sliding speed of 1.5 m/s, and the amount of molybdenum disulphide at 2 wt.%. An integrated Taguchi with GRA has been adopted for optimization of μ and wear rate of co-long composite by Sylajakumar et al. [21] combined Taguchi with GRA. Using this method, optimal parameter settings of were found to be an applied load of 60 N, a sliding speed of 1 ms^{-1}, and a sliding distance of 1000 m. Validation testing showed an improvement of 32.5 % in GRA. Savaran and Thanigaivelan [22] coupled Taguchi-particle component analysis and GRA to optimize the dimple geometry of stainless steel (SS316L). The results indicated that optimum parameter values for the highest GRG peak value of 0.2462 were an average power of 12 W, a pulse duration of 100 ns, and a frequency of 50 Hz.

Even though the Taguchi approach is simple, efficient, and economical, it is limited to optimizing a response at a time. The need for a method that can optimize multiple responses cannot be overemphasized. Therefore, this study is aimed at optimizing multiple responses of the coefficient of friction (μ) and specific abrasive wear rate (A_w) of reinforced PTFE composites using a Taguchi-GRA method. Moreover, abrasive wear performance should be optimized to prevent detrimental consequences on output performance.

1 EXPERIMENTAL

1.1 Materials

In this study, PTFE reinforced with carbon 25 % wt. and bronze 40 % wt. has been used. The materials fabricated by compression moulding process were supplied by Polymer Chemical Industry Ltd, Turkey in the form of square plates (100 mm × 100 mm × 6 mm). Selected properties of the materials are shown in Table 1. All samples have been cut from the same lot to minimize variations in the production technique.

Table 1. *Selected properties of materials used*

Materials	Code	ρ [gcm^{-3}]	σ [kgcm^{-2}]
Polytetrafluoroethylene	PTFE	2.10	380
Carbon-filled composite	CF25	2.05	210
Bronze-filled composites	BF40	3.05	280

1.2 Abrasive Test

An abrasive test was conducted according to ASTM G9 on a pin-on-disc tribometer (Model: Arton Paar, Switzerland), shown in Fig. 1 The counterface material for the wear test is a steel of disc 40 mm in diameter and thickness of 0 mm that has been heat-treated to obtain a surface hardness of 5 RC to 6 RC. This is ground to a surface finish of nearly 0.2 µm centreline average. The square samples (20 mm ×20 mm) were cut from the plates using computer numerical control water machining for the pin-on-abrasive testing. A specially designed fixture for holding the rectangular samples was designed and fabricated. The samples were inserted into the fixture and bolted and then loaded against SiC abrasive papers fixed to the hardened steel holder by means of liquid adhesive. Control parameters and their levels are shown in Table 2. The experimental design is as shown in Table 3 and was performed at 0.5 ms^{-1}. In all the experiments, mass before (m_1) and mass after (m_2) was measured using digital weighing balance (Model: PS 00 0.RS RADWAG, made in Poland) with 0 3 g precision accuracy. Testing was performed at room temperature (29 °C and relative humidity 5 %). Samples were cleaned with a brush before and after the experiment to remove debris and then weighed. The specific abrasive wear rate (A_w) was then computed from Eq. (1):

$$A_w = \frac{m_1 - m_2}{L\rho D}, \qquad (1)$$

where $m_1 - m_2$ is mass loss [g], L load [N], ρ density [gcm^{-3}] and D sliding distance [m], respectively. Two replicates were performed for each run and the average reported. The tribometer is connected to a computer with a data acquisition system that collects and transmits to software for processing and generation of results. The coefficient of friction (μ) is obtained from this process.

Table 2. *Control parameters and their levels*

Parameters	Symbol	Level 1	Level 2	Level 3
Load [N]	L	5	8	10
Grit size (mesh)	G	1000	320	220
Distance [m]	D	150	250	350

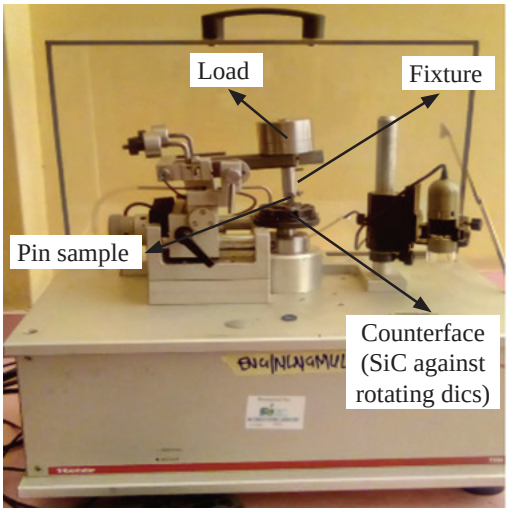

Fig. 1. *Arton Paar Tribometer used for the experiment*

1.3 Taguchi Design of Experiment (DOE)

The Taguchi design of the experiment is a tool which optimizes process parameters, keeping the process under control by managing variations while improving quality. In this study, based on literature, three parameters (i.e., load (L), grit size (G), and sliding distance (D)) at three levels were optimized. The experiment was designed based on a Taguchi L_9 (3^3) orthogonal array (OA) and conducted according to Table 2. Although the Taguchi design is simple, cost-effective, and improves the process, it is limited to optimizing a single response. For the optimization purpose, Taguchi uses the signal-to-noise ratios (*SN Rs*) to determine the optimum combination of parameters and followed Eq. (2).

$$(SNRs)STB = -10\log_{10}\left(\frac{1}{n}\sum_{i=1}^{n} y_i^2\right), \qquad (2)$$

where n is repetition of number of each trial and y_i outcome of the i^{th} experiment for each trial. *SN R* of μ and A_w were computed as per Eq. (2).

Table 3. *Taguchi L_9 (3^3) OA Design*

Run	L [N]	G (mesh)	D [m]
1	1	1	1
2	1	2	2
3	1	3	3
4	2	1	2
5	2	2	3
6	2	3	1
7	3	1	3
8	3	2	1
9	3	3	2

1.4 Grey Relational Analysis (GRA)

The Taguchi design approach is limited to single response optimization. For multi-objective optimization, GRA has been developed exploiting the Taguchi design to estimate the degree of correlation between test trials (series) via grey relational grade (GRG). To reduce data inconsistency, the data is normalized to a comparable range between 0 and1 [22]. Different objective functions exist, such as larger is better and smaller is better. The objective of this study is to minimize wear rate. Therefore, the smaller is better function is chosen, and the data are normalized according to (Eq. (3)):

$$X_i^*(k) = \frac{max\varphi_i(k) - \varphi_i(k)}{max\varphi_i(k) - min\varphi_i(k)}, \quad (3)$$

where $X_i^*(k)$ is normalized for the i^{th} experiment and $\varphi_i(k)$ initial sequence of the average responses.

1.5 Calculation of Grey Relational Coefficient (GRC) and Grade (GRG)

The next step after data normalization is the computation of the deviation sequence using (Eq. (4)):

$$\Delta_{oi}(k) = X_0^*(k) - X_i^*(k), \quad (4)$$

where $\Delta_{oi}(k)$ stands for deviation, $X_0^*(k)$ denotes normalized data and $X_i^*(k)$ refers to comparability sequence. GRC is thus estimated through (Eq. (5)):

$$\xi_i(k) = \frac{\Delta_{min} + \zeta\Delta_{max}}{\Delta_{oi}(k) + \zeta\Delta_{max}}, \quad (5)$$

where $\xi_i(k)$ is a GRC of each response calculated as a function of Δ_{min} and Δ_{max} the lowest and the highest deviations of each target factor, respectively. Differentiating or identification coefficient is symbolized by ζ and is demarcated within the range of $\zeta \in [0,1]$. This is usually set at one half to assign equivalent weights to every variable. As indicated in (Eq. (6)), GRG is then determined by taking mean of GRG of each response:

$$\gamma_i = \frac{1}{n}\sum_{i=1}^{n}\xi_i(k), \quad (6)$$

where γ_i is a GRG obtained for i^{th} test run, and n summation count of performance attributes. As soon as optimal level of variables is established via GRG, the last phase is to predict and confirm the quality attributes by (Eq. (7)):

$$\gamma_{predicted} = \gamma_m + \sum_{i=1}^{q}\gamma_0 - \gamma_m. \quad (7)$$

1.6 Analysis of Variance (ANOVA)

ANOVA is traditionally utilized to determine the significance of parameters on responses. Generally, Taguchi-GRA in combination with ANOVA is used to ascertain the percentage contribution of each factor to responses. The parameter with the largest percentage contribution is the most significant parameter and vice versa.

3 RESULTS AND DICUSSION

The results of the experiment based on Table 3 with corresponding SNRs of μ and A_w are presented in Table 4; these results are used for the Taguchi GRA. From Table 4, it was seen that run 4 produced the largest value of *SN Rs*, signifying that BF40 composite is the most resistant material in the study.

3.1 Effect of Load on μ and A_w

Fig. 2 shows the changes in A_w of reinforced PTFE composites as a function of load, grit size and distance. It is seen that A_w decreased with increasing applied load. The decrease in A_w of the PTFE based composites is because as the load increases the contact between samples, and the SiC counterface increases. This decreases the contact pressure, which allows particles of samples cooperating with the interface to share the stress. Additionally, a uniform, thin, and adherent transfer film in-between the samples and the counterface, which prevented direct contact with SiC counterface is another reason for the lower A_w. However, at lower load A_w was high. This is related to high contact pressure in-between and the ineffective tribo-layer between samples and counterface leading to direct contact of the samples with the counter surface. Fig. 3 presents the variation in μ of PTFE based composites as a function *L*, *G*, *D* and *S*. It is observed in Fig. 3 that μ shows increasing and decreasing trends as the load increased from 5 N to 8 N and from 8 N to 10 N, respectively. The low μ due to increasing the load is related to formation of layers by the fibres at the counterface and their viscoelastic properties. These layers act as lubricants between samples and SiC surface. High μ occurred, owing to destruction of these tribo-layers. These findings were in agreement with literature data [22] to [24].

3.2 Effect of Grit Size on μ and A_w

As seen in Fig. 2, increasing grit size causes a decrease in A_w. The minimum A_w at higher G is due to

deposition of debris from the samples and formation of transfer film between samples and counterface. This resulted in reduction of cutting efficiency of the SiC particles leading to lower A_w loss. At smaller grit size, say 220 mesh, the particles are rough and penetrated deeply into samples. This caused large plastic deformation, leading to removal of more materials by micro-ploughing action. As seen in Fig. 3, μ exhibited a linear decreasing trend with an increase in grit size. μ is related to smoothness and roughness of surfaces. The high μ at smaller grit size is related to roughness of the SiC particle, which offered significant resistance. However, decrease in μ when the grit size is large is attributed to smoothness of the SiC particles leading to the formation of protective layer (lubricant) at the contact surface, preventing direct contact of the samples with the abrasive surfaces. This finding agrees with the finding of [1] when bronze and carbon filled PTFE was studied.

3.3 Effect of Sliding Distance on μ and A_w

As seen in Fig. 2 A_w linearly decreases when the sliding distance increases. Also, μ follows the same trend as A_w (Fig. 3). In other words, both μ and A_w reduced due to increasing sliding distance. This could be explained on the basis that the sliding distance acts as lubrication to the contact surfaces thereby separating the pin samples from the abrasive counterface. More so, the lower wear rate of the reinforced PTFE composites could be linked to pull out or fracture of abrasive particles owing to the presence of fibres. Also, wear debris is transferred from the matrix leading to reduced wear rate. Similar findings were reported by [25] and [26] when nylon 6 was reinforced with glass fibre at varied proportions.

3.4 Main Effect and Percentage Contribution of Factors on μ and A_w

To determine the optimal combination of parameters for minimum μ and A_w, the *SN Rs* computed were obtained using Eq. (2). The largest *SN Rs* give the desired value. *SN Rs*' mean response table for μ is provided in Table 4, and the main effect plot depicted in Fig. 4. From Fig. 4, the optimum predicted maximum *SN Rs* for *L*, *G* and *D* are obtained at 10 N, 1000 mesh, and 0.8 m, respectively. In Table 5 the desired corresponding level values are bolded to facilitate understanding. The optimum combination of process parameters for desired μ is coded as L3G3D3. To estimate the significance (contribution) of each parameter on the μ, ANOVA (Table 6) was executed. As observed from Table 6, grit size with the percentage contribution of 68.38 %, shows the greatest effect on μ, followed by load with 14.12 % and the distance with 9.10 %. More so, it can be seen that the error is less than 10 %. Similarly, the same optimal combination of parameters was obtained for A_w (L3G3D3) for the lowest Aw using the main effect plot (Fig. 5). From the ANOVA results (Table 8), it can be implied that the grit size is the most significant parameter (42.56 %), followed by load (35.05 %), and distance shows the least significance (7.78 %) on A_w.

Table 4. *Taguchi L_9 (3^4) OA results with SNRs*

Run	μ	μ *SNRs* [dB]	A_w [mm³N⁻¹m⁻¹]	A_w *SNRs* [dB]
1	0.11	19.54	8.5714E-07	121.34
2	0.28	10.96	2.4390E-06	112.26
3	0.53	5.47	1.7237E-06	115.27
4	0.22	13.07	5.1639E-07	125.74
5	0.30	10.34	4.0816E-07	127.78
6	0.56	5.08	3.5366E-06	109.03
7	0.03	29.50	4.1115E-07	127.72
8	0.28	11.04	1.2568E-06	118.01
9	0.40	7.90	9.8095E-07	120.17

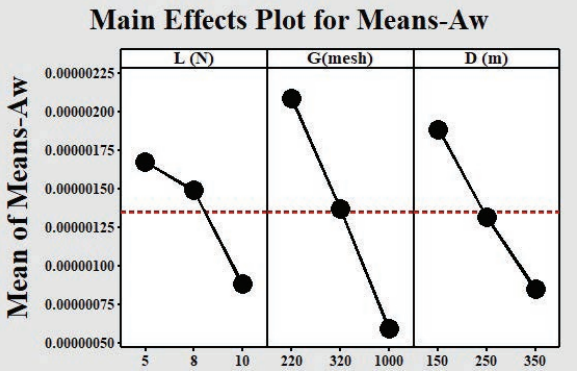

Fig. 2. *Effect of process variables on A_w*

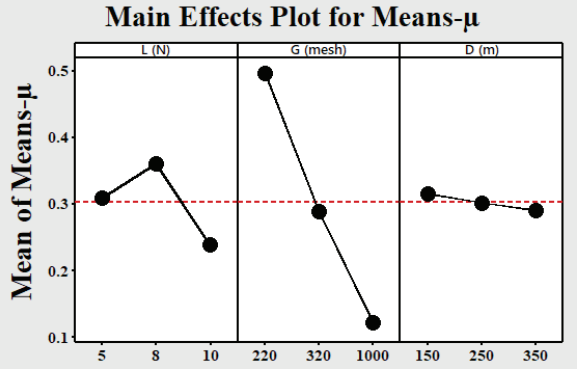

Fig. 3. *Effect of process variables on μ*

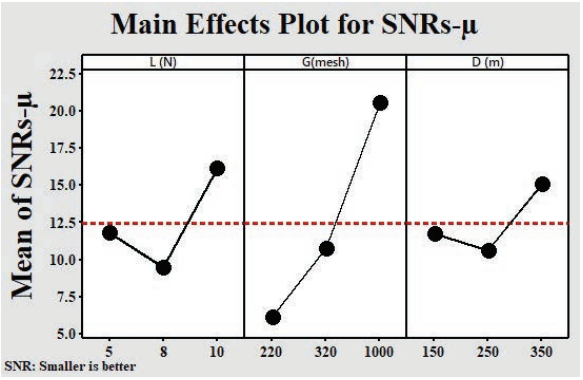

Fig. 4. *Main effect plot for SNRs of* μ

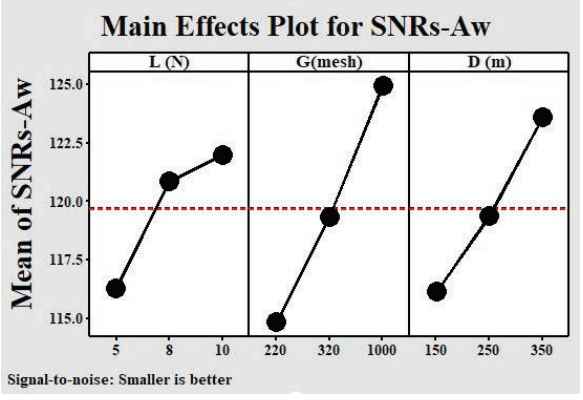

Fig. 5. *Main effect plot for SNRs of* A_w

Table 5. *Response table for SNRs of* μ *(STB)*

Factors	L1	L2	L3	Delta	Rank
L [N]	11.83	9.45	16.15	6.65	2
G [mesh]	6.15	10.78	20.54	14.39	1
D [m]	11.73	10.65	15.10	4.46	3

Table 6. *ANOVA for* μ

Source	DF	SSS	AMS	Contribution [%]
L [N]	2	68.3	34.15	14.62
G [mesh]	2	323.81	161.9	69.34
D [m]	2	32.41	16.2	6.94
Error	2	42.5	21.25	9.10
Total	8	467.01		100.00

Table 7. *Response table for SNRs of* A_w *(STB)*

Factors	L1	L2	L3	Delta	Rank
L [N]	116.30	120.90	122.00	5.7	3
G [mesh]	114.80	119.40	124.90	10.10	1
D [m]	116.10	119.40	123.60	7.50	2

Table 8. *ANOVA for* A_w

Source	DF	SSS	AMS	Contribution [%]
L [N]	2	54.31	27.15	15.05
G [mesh]	2	153.9	76.95	42.64
D [m]	2	84.59	42.01	23.4
Error	2	68.59	34.29	19.00
Total	8	360.81		100.00

3.5 Optimization via GRA

Principally, GRA is used to unravel real problems comprising a bounded amount of data. It is commonly employed to approximate the properties of indefinite systems having no black and white solutions. In a grey system, black signifies being without information whereas white connotes being with information. This technique is largely utilized to maximize or minimize problems involving multiples parameters and responses [27] and [28]. The data in Table 3 are pre-processed in the range of 0 to 1 according to Eq. (3). Thereafter, post-data processing was performed to obtain the deviation sequences using Eq. (4). Table 9 reveals the results of the post-data processing models. *GRC* for μ and A_w was computed using Eq. (5). Eventually, the mean of *GRC* is calculated to establish the *GRG*. As enumerated in Table 10, the calculated values of *GRG* were employed to produce equivalent *SNR*. A larger magnitude of SNR is useful, provided that the tests are close to the normalized magnitudes of *GRG*. Fig. 6 depicts the plot of *GRG* against *SNRs*. It indicates that seventh experimental run possesses the highest SNR. Correspondingly, the first rank was assigned to the seventh run. The straggling disposition of the *GRG*, below the plot of *SNR* in Fig. 6 adds to the discussion above.

Once the ranks are obtained, the *GRG* response table was developed. Each factor of *GRG* at the chosen level was selected and the average computed to obtain the mean *GRG* for different parameters. To obtain mean *GRG* values, of each parameter from Table 9, for instance, parameter *L* at L1 in the 1st, 2nd and 3rd runs. The corresponding GRG values from Table 9 was used for computation as depicted in Eq. (8).

$$L_1 = \frac{0.7737 + 0.4735 + 0.4435}{3} = 0.5336. \quad (8)$$

The mean of chosen *GRG* was computed utilizing technique above and put together to generate the response table (Table 11). The grades in the response table are used as a degree of correlation between the normalized and comparability sequence of GRA. Higher values of *GRG* show strong correlation

[29]. Hence, from Table 11, it is possible to achieve a combination of optimal parameters capable of maximizing the overall response. As observed in Table 10, the maximum *GRG* exists at L3, G1, and D3. Therefore, the optimal levels for useful abrasive tribological property of reinforced PTFE composites are L = 10 N, G at 1000 mesh and D = 6 m.

Table 9. *Reference and deviation sequences post data processing*

Run	X_i^*		Δ_{oi}	
	μ	A_w	μ	A_w
1	0.8510	0.8565	0.1490	0.1435
2	0.5234	0.3508	0.4766	0.6492
3	0.0458	0.5795	0.9542	0.4205
4	0.6399	0.9654	0.3601	0.0346
5	0.4833	1.0000	0.5167	0.0000
6	0.0000	0.0000	1.0000	1.0000
7	1.0000	0.9990	0.0000	0.0010
8	0.5282	0.7287	0.4718	0.2713
9	0.2951	0.8169	0.7049	0.1831

Table 10. *Computed GRC and GRG with SNRs*

Run	$X_i^*(k)$		γ_i	γ_i SNR [dB]	Rank
	μ	A_w			
1	0.7704	0.7770	0.7737	-2.2285	2
2	0.5120	0.4351	0.4735	-6.4929	7
3	0.3438	0.5432	0.4435	-7.0619	8
4	0.5813	0.9353	0.7583	-2.4030	3
5	0.4918	1.0000	0.7459	-2.5465	4
6	0.3333	0.3333	0.3333	-9.5424	9
7	1.0000	0.9981	0.9990	-0.0083	1
7	0.5145	0.6483	0.5814	-4.7107	5
8	0.4150	0.7320	0.5735	-4.8297	6
9	0.7704	0.7770	0.7737	-2.2285	2

Table 11. *Response table for GRGs*

Factors	L1	L2	L3	Delta	Rank
L [N]	0.5636	0.6125	0.7189	0.1544	3
G [mesh]	0.4501	0.6003	0.8437	0.3936	1
D [m]	0.5628	0.6018	0.7295	0.1667	2

Table 12. *ANOVA for GRG*

Source	DF	SSS	AMS	Contribution [%]
L [N]	2	7.22	3.61	10.37
G [mesh]	2	47.12	23.56	67.69
D [m]	2	7.96	3.98	11.44
Error	2	7.32	7.32	10.51
Total	8	69.61		100.00

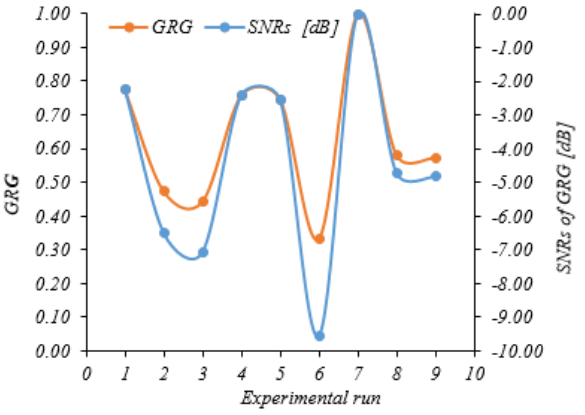

Fig. 6. *Plot of GRG versus SNRs*

3.6 ANOVA for GRG

To study the significance and percentage contribution of each parameter on the multiple Aw of reinforced PTFE composites, an ANOVA was executed for GRG. Taking into account the responses of μ and A_w, Table 12 depicts that grit size has the maximum influence of 67.69 % on the GRG, load has 23.37 %, and distance with lowest effect of 10.93 %.

3.7 Confirmatory Tests

When the identities of optimum levels were established, the concluding phase in GRA is to predict and validate performance enhancement of the responses. The prediction of *GRG* was conducted based on Eq. (8). Confirmatory tests were performed to validate the results of the analysis and mean of GRG of two trials was computed. For the optimal conditions, the μ and Aw were determined to be (0.04 and 1.40× 10^{-7}) mm^{3}N^{-1} m^{-1}, respectively. Moreover, it can be implied from Table 13 that the outcomes of the validation experiment are in concordance with the predicted results. Furthermore, an improvement of 55.22 % in *GRG* is also achieved. This enhancement in the experimental outcomes over the initial design parameter asserts the validity of the Taguchi-GRA method for improving the abrasive wear performance of reinforced PTFE composites.

Table 13. *Results of the confirmatory tests*

Initial design parameters		Optimal design parameters	
		Prediction	Experiment
Setting levels	L1G3D3	L3G1D3	L3G1D3
GRA	0.4435	1.0000	0.9904
Improvement in GRG [%]		55.65	55.22

5 CONCLUSIONS

This study presents the results of optimal parameters that influence the abrasive performance of reinforced PTFE composite involving multiple responses. Initially, the result of varying three factors (i.e., load, grit size, and sliding distance) on multiple responses of specific wear rate and coefficient of friction was investigated using a Taguchi L_9 orthogonal array and grey relational analysis. As seen in the response table of the grey relational grades, the optimum combination of parameters for improved abrasive performance of the reinforced PTFE composites was found to be load at 10 N, grit size at 1000 mesh, and sliding distance at 90 m. Analysis of variance for grey relational grade showed that grit size with 66.66 % is the most influential parameter followed by applied load with 21.73 %, and sliding distance indicated the least effect having 10.53 % on the grey relational grade. Finally, validation tests were conducted to validate the improvement 5.22 % in grey relational grade from 0.4443 for the initial design parameters ($L_1G_1D_3$) to 0.9093 for the optimal combination of parameters ($L_2G_3D_3$). It is recommended that heavy conditions of parameters should be studied. The presented Taguchi-grey relational analysis results has proven to be capable of dealing with several responses in the optimization of tribological wear study of PTFE matrix composites.

6 ACKNOWLEDGEMENTS

The authors are grateful to Kano University of Science and Technology, Wudil, Kano State, Nigeria, Kano State Scholarship Board, Kano State, Nigeria and Near East University, Nicosia, Cyprus

8 REFERENCES

[1] Şahin, Y. (2015). Analysis of abrasive wear behavior of PTFE composite using Taguchi's technique. *Cogent Engineering*, vol. 2, no. 1, p. 1-15, **DOI:10.1080/23311916.2014.1000510**.

[2] Vasilev, A.P. Struchkova, T.S., Nikiforov, L.A., Okhlopkova, A.A., Grakovich, P.N., Shim, E.L., Cho, J.-H. (2019). Mechanical and tribological properties of polytetrafluoroethylene composites with carbon fiber and layered silicate fillers. *Molecule*s, vol. 24, art. ID. 224, **DOI:10.3390/molecules24020224**.

[3] He, R., Chang, Q., Huang, X., Bo, J. (2018). Improved mechanical properties of carbon fiber reinforced PTFE composites by growing graphene oxide on carbon fiber surface. *Composite Interfaces*, vol. 25, no. 11, p. 995-1004, **DOI:10.1080/09276440.2018.1451677**.

[4] Suh, J., Bae, D. (2016). Mechanical properties of polytetrafluoroethylene composites reinforced with graphene nanoplatelets by solid-state processing. *Composites Part B: Engineering*, vol. 95, p. 317-323, **DOI:10.1016/j.compositesb.2016.03.082**.

[5] Friedrich, K., Zhang, Z., Schlarb, A.K. (2005). Effects of various fillers on the sliding wear of polymer composites. *Composites Science and Technology*, vol. 65, no. 15-16, p. 2329-2343, **DOI:10.1016/j.compscitech.2005.05.028**.

[6] Harsh, A.P., Tewari, U.S. (2007). Tribological studies on glass fiber reinforced polyether ketone composites. *Journal of Reinforced Plastics Composites*, vol. 23, no. 1, p. 65-82, **DOI:10.1177/0731684404029349**.

[7] Hashmi, S.A.R., Dwivedi, U.K., Chand, N. (2006). Friction and sliding wear of UHMWPE modified cotton fibre reinforced polyester composites. *Tribology Letters*, vol. 21, p. 79-87, **DOI:10.1007/s11249-006-9014-y**.

[8] Suresha, B., Kumar, K.N.S. (2009). Investigations on mechanical and two-body abrasive wear behaviour of glass/carbon fabric reinforced vinyl ester composites. *Materials & Design*, vol. 30, no. 6, p. 2056-2060, **DOI:10.1016/j.matdes.2008.08.038**.

[9] Shipway, P.H., Ngao, N.K. (2003). Microscale abrasive wear of polymeric materials. *Wear*, vol. 255, no. 1-6, p. 742-750, **DOI:10.1016/S0043-1648(03)00106-6**.

[10] Ravikumar, B.N., Suresha, B. Venkataramareddy, M. (2009). Effect of particulate fillers on mechanical and abrasive wear behaviour of polyamide 66/polypropylene nanocomposites. *Materials & Design*, vol. 30, no. 9, p. 3852-3858, **DOI:10.1016/j.matdes.2009.01.034**.

[11] Liu, C., Ren, L.Q., Arnell, R.D., Tong, J. (1999). Abrasive wear behavior of particle reinforced ultrahigh molecular weight polethylene composites. *Wear*, vol. 225-229, p. 199-204, **DOI:10.1016/50043-1648(99)00011-3**.

[12] Yousif, B.F., Nirmal, U., Wong, K.J. (2010). Three-body abrasion on wear and frictional performance of treated betelnut fibre reinforced epoxy (T-BFRE) composite. *Materials & Design*, vol. 31, no. 9, p. 4514-4521, **DOI:10.1016/j.matdes.2010.04.008**.

[13] Harsha, A.P. Tewari U.S. (2002). Abrasive wear resitance of glass fibre reinforced polysulfone composites. *Indian Journal of Engineering & Materials Science*, vol. 9, p. 203-208.

[14] Sunil Thakur and SR Chauhan. (2014). Friction and sliding wear characteristics study of submicron size cenosphere particles filled vinylester composites using Taguchi design of experimental technique. *Journal of Composite Materials*, vol. 48, no. 23, p. 2831-2841, **DOI:10.1177/0021998313502740**.

[15] Cho, MH., Bahadur, S., Pogosian, A.K. (2005). Friction and wear studies using Taguchi method on polyphenylene sulfide filled with a complex mixture of MoS2, Al203, and other compounds. *Wear*, vol. 258, no. 11-12, p. 1825-1835, **DOI:10.1016/j.wear.2004.12.017**.

[16] Chang, B.P., Yong, Y.F., Akil, H., Nasir, R. (2017). Optimization on abrasive wear performance of pultruded kenaf-reinforced polymer composite using Taguchi method. Key Energy Materials, vol. 739, p. 42-49, **DOI:10.4028/www.scientific.net/KEM.739.42**.

[17] Deng, J.L. (1989). *Introduction to Grey System Theory*. Journal of Grey Systems, vol. 1, p. 1-24.

[18] Ramesh, B.N., Suresha, B. (2014). Optimization of tribological parameters in abrasive wear mode of carbon-epoxy

hybrid composites. *Materials & Design*, vol. 59, p. 38-49, **DOI:10.1016/j.matdes.2014.02.023**.

[19] Subbaya, K.M., Suresha, B., Rajendra, N., Varadarajan, Y.S. (2012). Grey-based Taguchi approach for wear assessment of SiC filled carbon-epoxy composites. *Materials & Design*, vol. 41, p. 124-130, **DOI:10.1016/j.matdes.2012.04.051**.

[20] Dharmalingam, S., Subramanian, R., Kök, M. (2013). Optimization of abrasive wear performance in aluminium hybrid metal matrix composites using Taguchi-grey relational analysis. *Proceedings of the Institution of Mechanical Engineers, Part J: Journal of Engineering Tribology*, vol. 227, no. 7, p. 749-760, **DOI:10.1177/1350650112467945**.

[21] Sylajakumari, P.A., Ramakrishnasamy, R., Palaniappan, G. (2018). Taguchi grey relational analysis for multi-response optimization of wear in co-continous composite. *Materials*, vol. 11, no. 9, p. 1743, **DOI:10.3390/ma11091743**.

[22] Saravanan, K.G., Thanigaivelan, R. (2021). Optimisation of laser parameters and dimple geometry using PCA-coupled GRG. *Strojniški vestnik - Journal of Mechanical Engineering*, vol. 67, no. 10, p. 525-533, **DOI:10.5545/sv-jme.2021.7246**.

[23] Kim, J.W., Jang, H., Kim, J.W. (2014). Friction and wear of monolithic and glass fibre reinforced PA66 in humid condition. *Wear*, vol. 309, no. 1-2, p. 82-88, **DOI:10.1016/j.wear.2013.11.007**.

[24] Chowdhury, M.A., Nuruzzaman, D.M., Roy, B.K., Samad, S. Sarker, R., Rezwan, A.H.M. (2013). Experimental Investigation of friction coefficient and wear rate of composite materials sliding against smooth and rough mild steel counterfaces. *Tribology in Industry*, vol. 35, no. 4, p. 286-292.

[25] Gunes, I. Uygunoğlu, T., Çelik, A.G. (2021). Tribological properties of fly ash blended polymer composites. *Matéria*, vol. 26, no. 1, **DOI:10.1590/S1517-707620210001.1229**.

[26] Deo, C., Acharya, S.K. (2010). Effects of load and sliding velocity on abrasive wear of Lantana camara fibre-reinforced. *Proceedings of the Institution of Mechanical Engineers, Part J: Journal of Engineering Tribology*, vol. 224, no. 5, p. 491-496, **DOI:10.1243/13506501JET699**.

[27] Zou, S.Y., Huang, R., Chi, M.C., Hsu, H.M. (2013). Factors affecting the effectiveness of inorganic silicate sealer materials through multi-quality characteristics. *Materials*, vol. 6, no. 3, p. 1191-1204, **DOI:10.3390/ma6031191**.

[28] Kasemsiri, P., Dulsang, N., Pongsa, U., Hiziroglu, S., Chindaprasit, P. (2017). Optimization of biodegradable foam composites from cassava starch, oil palm fibre, chitosan and palm oil using Taguchi method and grey relational analysis. *Journal of Polymers and the Environment*, vol. 25, p. 378-390, **DOI:10.1007/s10924-016-0818-z**.

[29] Wojceichowski, P. Maruda, S., Krolczyk, R.W., Nieslony, G.M. (2018). Application of signal noise ratio and grey relational analysis to minimze forces and vibrations during precise ball end milling. *Precision Engineering*, vol. 51, p. 582-596, **DOI:10.1016/j.precisioneng.2017.10.014**.

Strojniški vestnik - Journal of Mechanical Engineering 68(2022)5, 368-373
DOI:10.5545/sv-jme.2021.7538
Short Scientific Paper
Received for review: 2021-12-30
Received revised form: 2022-03-13
Accepted for publication: 2022-03-28

Numerical Analysis on a Constant Rate of Kinetic Energy Change Based a Two-Stage Ejector-Diffuser System

Virendra Kumar[1] – Anil Kumar[2] – Surendra Kumar Yadav[3] – Anshul Yadav[4] – Lalta Prasad[5] – Jerzy Winczek[6] *

[1] Noida Institute of Engineering and Technology, India
[2] Kamla Nehru Institute of Technology, India
[3] K R Mangalam University, India
[4] CSIR-Central Salt and Marine Chemicals Research Institute, India
[5] National Institute of Technology Uttarakhand, India
[6] Częstochowa University of Technology, Poland

Supersonic ejector energy flow devices are extensively used in various applications, such as pumping, mixing, compression, etc. The conventional single-stage ejector (SSE) design approaches are inefficient for modelling an efficient ejector because of their inefficiency in minimizing mixing losses in the mixing chamber, thermodynamic shock in constant area diffuser, and utilization of redundant discharged momentum at the exit of the first stage. The physics-based single-stage ejector design has better solutions because it minimizes irreversibility due to thermodynamic shocks. The present study utilizes the constant rate of a kinetic energy change physics-based approach to design a two-stage ejector (TSE) for water vapour. The computational fluid dynamics (CFD) tool ANSYS-Fluent has been utilized to predict flow characteristics. The performance of the ejector-diffuser system has also been compared with a single-stage ejector. It is found that the performance of TSE is 70 % higher than that of the performance of SSE.

Keywords: ejector-diffusor, constant rate of kinetic energy change, two-stage ejector, single-stage ejector, computational fluid dynamics

Highlights

- *The computation of a two-stage ejector-diffuser profile was performed based on the CRKEC approach.*
- *A comparison of a two-stage ejector-diffuser with a single-stage ejector was carried out.*
- *The performance of the two-stage ejector-diffuser is 70% higher than that of a single-stage ejector.*
- *The CRKEC approach helps in the computation of high-performance two-stage ejector geometrical profiles.*

0 INTRODUCTION

The ejector's simplicity and reliability are its key features and the reason it is widely used; however, the ejector has low efficiency. It is used to pump, induce, mix and/or recompress primary/motive and two secondary/induced flows. The ejector has numerous industrial applications, including refrigeration systems **[1]** to **[4]**, bus air-conditioning **[5]** and **[6]**, sea-water desalination systems **[7]** and **[8]**, chemical lasers **[9]** and hydrogen fuel cells **[10]** and **[11]** others.

Conventional design ejectors are based on constant area mixing (CAM) **[12]** and constant pressure mixing (CPM) **[13]**. These ejectors were categorized based on the exit position of the nozzle in the mixing section. From previous studies, one of the major losses in conventional ejectors is due to thermodynamic shocks. To tackle the thermodynamic shock in the constant area section of a conventional ejector-diffuser, a one-dimensional gas-dynamic constant rate of momentum change (CRMC) approach was presented by Eames **[14]**. This approach helped reduce thermodynamic shock. Kitrattana et al. **[15]** studied the performance of three steam ejectors designed based on conventional and CRMC approaches. The result showed that the CRMC ejector performance is better than conventional ejectors. Furthermore, a complete ejector design approach with frictional effect is presented by Kumar et al. **[16]**. In another study, Kumar et al. **[17]** presented a physics-based ejector design approach, i.e., constant rate of kinetic energy change (CRKEC), to design a complete single-stage ejector. The CRKEC approach converts the constant area section convention diffuser section into a variable area and minimizes loss due to mixing and thermodynamic shocks.

The performance of the conventional (CAM/CPM) and physics-based (CRMC/CRKEC) single-stage ejectors remains low. Apart from utilizing different design approaches to improve the performance, many researchers have attempted to minimize mixing losses by optimizing the supersonic nozzle **[18]** to **[20]**, nozzle exit positions **[21]**, suction chamber **[22]**, mixing chamber **[23]**, and diffuser section **[24]**. Consequently, the present era of the ejector modified the single-stage ejector into a two/multi-stage ejector. The two-stage compression is another way to decrease throttling loss and improve system efficiency. The single-stage ejector always has a primary flow inlet, a secondary/induced flow

*Corr. Author's Address: Częstochowa University of Technology, 42-201 Częstochowa, Poland, winczek@gmail.com

inlet, a mixing chamber, and a diffuser. In the case of two-stage ejectors, the second induced/entrained flow enters at the exit of the mixing section of single stage ejector [25]. It better utilizes the redundant momentum discharging at the exit of the mixing of the first stage of the ejector (Fig. 1). The system usually comprises one motive stream inlet and two (primary and secondary) induced fluid inlets; the second induced fluid can be accelerated by the combined (primary motive and induced) flow of the first stage [26]. The process of the momentum exchange between the motive and the induced fluids and carry over the former by the latter is often termed "entrainment". The entrainment ratio is a global performance parameter, which is a ratio of the mass flow rate of induced flow to motive flow.

Ding et al. [27] utilized the CAM approach to design a two-stage ejector for sub-zero refrigeration for R134a working fluid. The operating temperatures of the generator were used in the range of 85 °C to 74 °C and 24 °C to 0 °C for the evaporator. The CFD study was carried out to find the best design parameters for a range of operating conditions. The results showed that using a two-stage ejector in sub-zero refrigeration applications could benefit cold-chain logistics systems. Kong and Kim [28] studied single-stage and two-stage ejectors and concluded that the two-stage ejector-diffuser system could be utilized to improve the inefficiency of conventional single-stage ejector-diffuser systems by reducing energy loss and utilization of redundant momentum of the discharge flow.

It is evident from the literature that the single-stage ejector-diffuser has low performance. It is also found that the conventional design ejectors have higher thermodynamic losses than physics-based ones. Therefore, the objective of the present study is to utilize redundant momentum and kinetic energy of discharged flow to induce secondary mass flow. It is expected that the two-stage ejector designed based on the CRKEC approach will further improve the flow mixing and entrainment performance of the ejector-diffuser system by installing a second stage. The numerical analysis is performed on the CRKEC design two-stage ejector-diffuser (TSED) and compared with the single-stage ejector-diffuser (SSED).

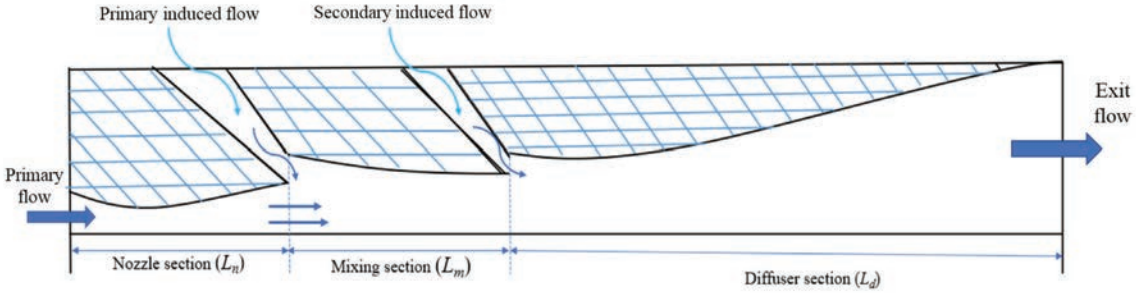

Fig. 1. *Axisymmetric two-stage ejector (TSE) system*

1 COMPUTATIONAL GEOMETRY

A supersonic ejector consists of three major components: supersonic nozzle, mixing chamber, and diffuser section. The CRKEC approach [17] for ideal gas was further manipulated using the Redlich-Kwong equation to model supersonic ejector for water vapour. The separate MATLAB of each component was made to compute variation in geometrical coordinates and flow properties at each small step 0.5 mm. The selection of CRKEC constants to compute geometry and flow properties for the given length was based on the recommendation of Kumar et al. [17].

The computed geometrical profile along the convergent-divergent nozzle is shown in Fig. 2. The profile of the nozzle is presented for the selected CRKEC constant. The CRKEC constant was selected based on the targeted Mach number (~2.5) and the convergent and divergent section length. The variation in radius is continuously decreased up to the throat. At the throat, the minimum radius is approximately 1.01 mm, and the inlet radius of the nozzle is 2.28 mm. The radius at the outlet of the nozzle is 5.37 mm.

The mixing section is a converging passage where primary motive and induced flows are mixed and exchange the fluids' momentum and kinetic energy. The actual mixing phenomena is very complex, which is difficult to quantify and explain. After mixing both primary motive and induced flow, it is tried to achieve an equilibrium condition at the exit of the mixing section. The computation mixing chamber geometry starts with the computation of equilibrium properties

from exit to inlet of chamber. The variation in radius along the mixing section is shown in Fig. 3

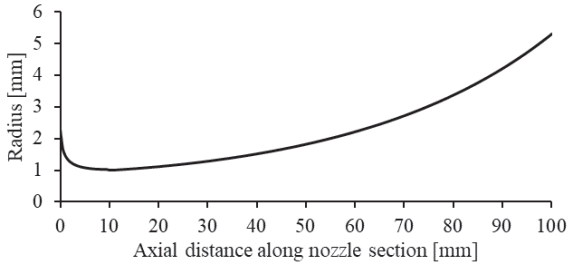

Fig. 2. *Variation in nozzle radius along with nozzle profile*

The mixing section is a converging passage where primary motive and induced flows are mixed and exchange the fluids' momentum and kinetic energy. The actual mixing phenomena is very complex, which is difficult to quantify and explain. After mixing both primary motive and induced flow, it is tried to achieve an equilibrium condition at the exit of the mixing section. The computation mixing chamber geometry starts with the computation of equilibrium properties from exit to inlet of chamber. The variation in radius along the mixing section is shown in Fig. 3

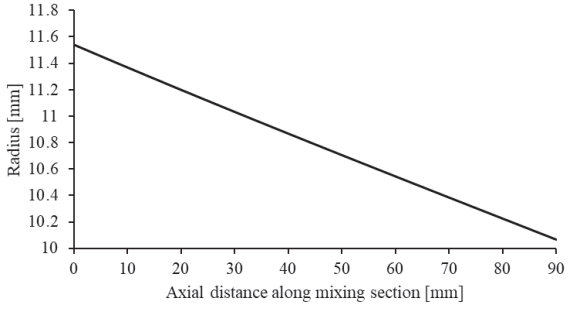

Fig. 3. *Variation in radius along mixing section*

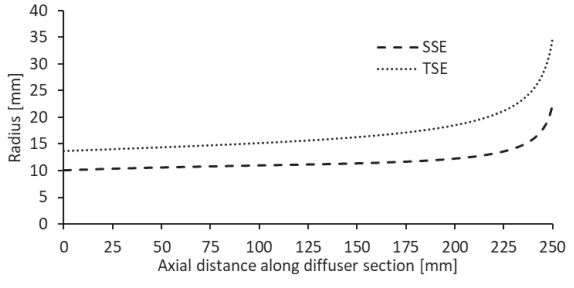

Fig. 4. *Radius variation along diffuser section*

The diffuser is a continuous increasing passage from the inlet to exit. The main function of the diffuser is to convert the kinetic energy of fluid into pressure energy. For the selected CRKEC constant and diffuser length, the computed inlet and outlet radius for SSED is 0.08 mm and 22.45 mm and for TSED is 36 mm and 36 mm. The rate of change in the radius is nearer to the outlet. The variation in radius along the diffuser is shown in Fig 4.

2 COMPUTATIONAL STUDIES

The actual flow through the ejector systems considered in this work is an axisymmetric, steady turbulent compressible flow. All the flow variables are expected to vary along with axial and radial directions. One-dimensional gas dynamics theory can be considered equivalent to area-averaged axisymmetric flow. Computational fluid dynamic (CFD) tool has been utilized to estimate flow characteristics and ejector parameters using the geometry generated using one-dimensional analysis. The conservation equations governing the fluid flow in an ejector are considered, assuming compressible, steady-state, axisymmetric flow. The Favre-averaged Navier-Stokes equations are the most suitable for variable density flows and will be used in the present study. The total energy equation including viscous dissipation is also included and coupled with the ideal gas law set. The standard k-ε model is a semi-empirical model based on model transport equations for the turbulence kinetic energy (k) and its dissipation rate (ε). Turbulence models used in the present study rely on the Boussinesq hypothesis, which is based on an eddy viscosity assumption, making the Reynolds stress tensor averaging proportional to the mean deformation rate tensor.

The grid independence test is generally used to select optimal grid size for CFD analysis. In general, local flow variables predicted by the CFD studies are used to decide the optimal grid size. This study utilized the global performance parameter of ejector "entrainment ratio (ω)" at design conditions. Various mesh sizes (8,000 to 8,000) were used to perform grid independence tests on a two-stage ejector. The standard, k–ε turbulence model, has been utilized to study the grid-independent test. The gradient mesh was employed near the wall and dense mesh within the mixing section to resolve shocks, expansion waves, and mixing phenomena. All the mesh sizes demonstrated close agreement with the analytical one with a small deviation. It is also observed that further refinement of mesh is not required. Therefore, considering computational time and accuracy, all further studies were carried out using 45,47 cells for both ejectors.

3 RESULTS AND DISCUSSION

The design of ejector components and their computations are discussed in Sections 2 and 3 respectively. The computed geometries for SSE and TSE ejectors have been compared and presented for design conditions. A detailed discussion on the physics of flow through specially designed two-stage ejector (TSE) in comparison to single-stage ejector (SSE) are discussed in this section. The nozzle exit position (NXP) relative distance of the primary nozzle outlet to the mixing chamber inlet was fixed at zero for all the studies.

The static pressure variations along the mixing-diffuser section for SSE and TSE is shown in Fig. 5 A strong pressure pulsation has been observed in the mixing section of both the ejector sections. This pulsation is due to the mixing of primary supersonic flow with incompressible subsonic primary/secondary induced flow [21]. The primary and induced fluids undergo intense interaction inside the mixing section. The intense interaction can be seen from fluctuations in the prediction of centreline static pressure in the mixing section. During this interaction, both fluids exchange their momentum and kinetic energy and reach an internal equilibrium, resulting in an almost uniformly mixed flow. As the flow travels downstream, the pulsation of static pressure is diminishing and almost negligible at the exit of the diffuser.

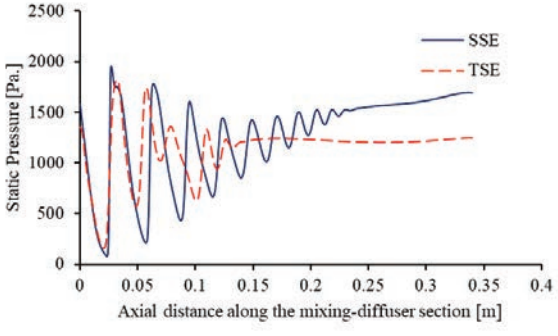

Fig. 5. *Axial variation of centreline static pressure along mixing-diffuser section*

The CFD centreline Mach number and temperatures variation are shown in Figs. 6 and 7 The intense interaction of primary and secondary flow can be seen in the mixing section. From the Mach number plot (Fig. 0) , the presence of alternate oblique shocks and expansion waves can be seen. Because of the presence of the oblique shocks, the Mach number remained largely supersonic and showed significant pulsations followed by shockless diffusion in both the ejectors. Due to the oblique shocks and expansion waves in the mixing section, the average values of static pressure and temperature (Figs. 5 and 7 are nearly passing through the centres of pulsations. However, the local average Mach number predicted by the D model is less than the centreline Mach number predicted by CFD. The pressure loss in the mixing section is higher than in the diffuser section because of the oblique shocks and expansion waves. The Mach number and static temperature variations predicted by the CFD centreline for both the ejectors qualitatively match each other. There is a minor mismatch in a quantitative variation of these parameters at the exit of the diffuser.

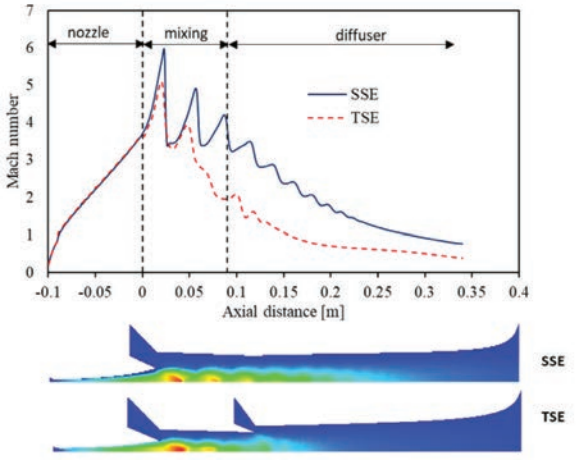

Fig. 6. *Axial variation of centreline Mach number along mixing-diffuser section*

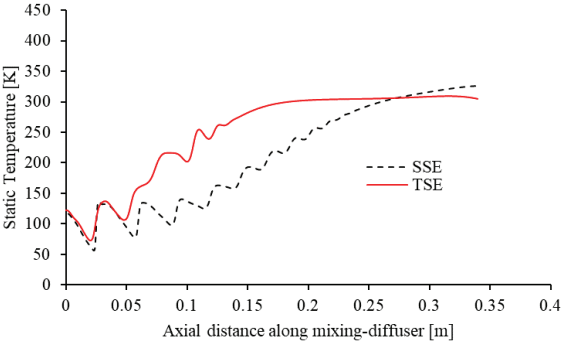

Fig. 7. *Axial variation of centreline static temperature along the mixing-diffuser section*

The entrainment ratio (ω) is a well-known and key performance parameter of the ejector system. The CFD on-design value of entrainment ratio for both the single-stage and two-stage ejectors are shown in Fig. 8 The two-stage ejector entrainment ratio ω is

higher than that of the single-stage ejector. The TSE entrainment ratio compared to SSE at on-design is Ø % higher. This is due to the utilization of the redundant flow energy at the second stage for inducing secondary induced flow in a two-stage ejector.

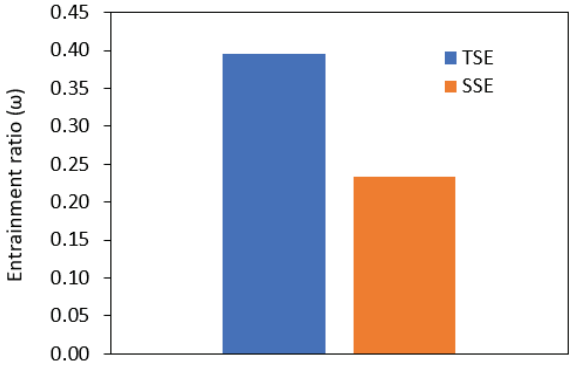

Fig. 8. *Entrainment ratio (ω) at on-design for SSE and TSE*

4 CONCLUSIONS

This study developed an analytical model for a two-ejector design. The coordinates of the ejector profile and flow properties were computed based on the CRKEC approach using MATLAB. The computed geometrical profile has been utilized for the CFD study. The performance of a two-stage ejector is compared with a single-stage stage ejector designed based on the same analytical model. The analytical results and CFD results for both the ejectors have been presented and compared at on-design conditions. The results showed that the two-stage performance is Ø % higher than that of the single-stage ejector. The entrainment region is one of the most crucial components of the ejector, as it causes significant loss due to the mixing of supersonic primary and subsonic induced flow. The CRKEC approach can help compute geometrical profile and flow characteristics in small steps.

5 REFERENCES

[1] Yari, M. (2009). Performance analysis and optimization of a new two-stage ejector-expansion transcritical CO_2 refrigeration cycle. *International Journal of Thermal Sciences*, vol. 48, no. 10, p. 1997-2005, **DOI:10.1016/j.ijthermalsci.2009.01.013**.

[2] Yan, J., Wen, N., Wang, L., Li, X., Liu, Z., Li, S. (2018). Optimization on ejector key geometries of a two-stage ejector-based multi-evaporator refrigeration system. *Energy Conversion and Management*, vol. 175, p.142-150, **DOI:10.1016/j.enconman.2018.08.110**.

[3] Grazzini, G., Rocchetti, A. (2002). Numerical optimisation of a two-stage ejector refrigeration plant. *International Journal of Refrigeration*, vol. 25, no. 5, p. 621-633, **DOI:10.1016/S0140-7007(01)00063-9**.

[4] Işkan, Ü., Direk, M. (2021). Experimental investigation on the effect of expansion valves in a dual evaporator ejector refrigeration system using R134a and R456a. *Energy Sources, Part A: Recovery, Utilization, and Environmental Effects*, **DOI:10.1080/15567036.2021.1982076**.

[5] Ünal ,S. (2015). Determination of the ejector dimensions of a bus air-conditioning system using analytical and numerical methods. *Applied Thermal Engineering*, vol. 90, p. 110-119, **DOI:10.1016/j.applthermaleng.2015.06.090**.

[6] Ünal, S., Yilmaz, T. (2015). Thermodynamic analysis of the two-phase ejector air-conditioning system for buses. *Applied Thermal Engineering*, vol. 79, p. 108-116, **DOI:10.1016/j.applthermaleng.2015.01.023**.

[7] Qamar, A., Kerdi, S., Ali, S.M., Shon, H.K., Vrouwenvelder, J.S., Ghaffour, N. (2021). Novel hole-pillar spacer design for improved hydrodynamics and biofouling mitigation in membrane filtration. *Scientific Reports*, vol. 11, art. ID 6979, **DOI:10.1038/s41598-021-86459-w**.

[8] Suresh Kumar, S.M., Duraibabu, D., Subramanian, K. (2014). Studies on mechanical, thermal and dynamic mechanical properties of untreated (raw) and treated coconut sheath fiber reinforced epoxy composites. (2014). *Materials & Design*, vol. 59, p. 63-69, **DOI:10.1016/j.matdes.2014.02.013**.

[9] Singhal, G., Rajesh, R., Mainuddin, Tyagi, R.K., Dawar, A.L., Subbarao, P.M.V, Endo, M. (2006). Two-stage ejector based pressure recovery system for small scale SCOIL. *Experimental Thermal and Fluid Science*, vol. 30, no. 5, p. 415-426, **DOI:10.1016/j.expthermflusci.2005.09.002**.

[10] Yang, Y., Du, W., Ma, T., Lin, W., Cong. M,, Yang, H., Yu, Z. (2020). Numerical studies on ejector structure optimization and performance prediction based on a novel pressure drop model for proton exchange membrane fuel cell anode. *International Journal of Hydrogen Energy*, vol. 45, no. 43. p. 23343-23352, **DOI:10.1016/j.ijhydene.2020.06.068**.

[11] Chen, F., Hou, M., Li, J., Pei, Y., Wang, Y. (2021). Proton exchange membrane fuel cell ejector test platform design and ejector test analysis. *World Electric Vehicle Journal*, vol. 12, no. 3, art. ID 103, **DOI:10.3390/wevj12030103**.

[12] Keenan, J.H., Neumann, E.P. (1942). A Simple Air Ejector. *Journal of Applied Mechanics*, vol. 9, no. 2, p.A75-A81, **DOI:10.1115/1.4009187**.

[13] Nguyen, V.V., Varga, S., Dvorak. V. (2019). HFO1234ze(e) as an alternative refrigerant for ejector cooling technology. *Energies*, vol. 12, no. 21, art. ID 4045, **DOI:10.3390/en12214045**.

[14] Eames, I.W. (2002). A new prescription for the design of supersonic jet-pumps: The constant rate of momentum change method. *Applied Thermal Engineering*, vol. 22, no. 2, p. 121-131, **DOI:10.1016/S1359-4311(01)00079-5**.

[15] Kitrattana, B., Aphornratana, S., Thongtip, T., Ruangtrakoon, N. (2017). Comparison of traditional and CRMC ejector performance used in a steam ejector refrigeration. *Energy Procedia*, vol. 138, p. 476-481, **DOI:10.1016/j.egypro.2017.10.229**.

[16] Kumar, V., Singhal, G., Subbarao, P.M.V. (2013). Study of supersonic flow in a constant rate of momentum change (CRMC) ejector with frictional effects. *Applied Thermal*

Engineering, vol. 60, no. 1-2, p. 61-71, **DOI:10.1016/j.applthermaleng.2013.06.045**.

[17] Kumar, V., Singhal, G., Subbarao, P.M.V. (2018). Realization of novel constant rate of kinetic energy change (CRKEC) supersonic ejector. *Energy*, vol. 164, p. 694-706, **DOI:10.1016/j.energy.2018.08.184**.

[18] Vereda, C., Ventas, R., Lecuona, A., Venegas, M. (2012). Study of an ejector-absorption refrigeration cycle with an adaptable ejector nozzle for different working conditions. *Applied Energy*, vol. 97, p. 305-312, **DOI:10.1016/j.apenergy.2011.12.070**.

[19] Kong, F.S., Kim. H.D., Jin, Y., Setoguchi, T. (2013). Application of Chevron nozzle to a supersonic ejector-diffuser system. *Procedia Engineering*, vol. 56, p. 193-200, **DOI:10.1016/j.proeng.2013.03.107**.

[20] Atmaca, A.U., Erek, A., Ekren, O. (2020). One-dimensional analysis of the convergent-divergent motive nozzle for the two-phase ejector: Effect of the operating and design parameters. *Applied Thermal Engineeering*, vol. 181, art. ID 115866, **DOI:10.1016/j.applthermaleng.2020.115866**.

[21] Kumar, V., Subbarao, P.M.V., Singhal, G.(2019). Effect of nozzle exit position (NXP) on variable area mixing ejector. *SN Applied Sciences*, vol. 1, art. ID 1473, **DOI:10.1007/s42452-019-1496-y**.

[22] Bartosiewicz, Y., Aidoun, Z., Desevaux, P., Mercadier, Y. (2005). Numerical and experimental investigations on supersonic ejectors. *International Journal of Heat and Fluid Flow*, vol 26, no. 1, p. 56-70, **DOI:10.1016/j.ijheatfluidflow.2004.07.003**.

[23] Sierra-Pallares, J., García del Valle, J., Paniagua, J.M., García, J., Méndez-Bueno, C., Castro, F. (2018). Shape optimization of a long-tapered R134a ejector mixing chamber. *Energy*, vol. 165, p. 422-438, **DOI:10.1016/j.energy.2018.09.057**.

[24] Kong, F., Kim, H.D. (2016). Optimization study of a two-stage ejector - diffuser system. *International Journal of Heat and Mass Transfer*, vol. 101, p. 1151-1162, **DOI:10.1016/j.ijheatmasstransfer.2016.05.129**.

[25] Kumar, A., Kumar, V., Subbarao, P.M.V., Yadav, S.K., Singhal, G. (2021). Numerical assessment on the performance of variable area single- and two-stage ejectors: A comparative study. *Proceedings of the Institution of Mechanical Engineers, Part E: Journal of Process Mechanical Engineering*, vol. 236, no. 1, p. 114-125, **DOI:10.1177/09544089211033129**.

[26] Yadav, S.K., Pandey, K.M., Kumar, V., Gupta, R. (2020). Computational analysis of a supersonic two-stage ejector. *Materials Today: Proceedings*, vol. 38, p. 2700-2705, **DOI:10.1016/j.matpr.2020.08.483**.

[27] Ding, Z., Wang, L., Zhao, H., Zhang, H., Wang, C. (2016). Numerical study and design of a two-stage ejector for subzero refrigeration. *Applied Thermal Engineering*, vol. 108, p. 436-448, **DOI:10.1016/j.applthermaleng.2016.07.104**.

[28] Kong, F., Kim, H.D. (2015). Analytical and computational studies on the performance of a two-stage ejector-diffuser system. *International Journal of Heat and Mass Transfer*, vol. 85, p. 71-87, **DOI:10.1016/j.ijheatmasstransfer.2015.01.117**.

Vsebina

Strojniški vestnik - Journal of Mechanical Engineering
letnik 68, (2022), številka 5
Ljubljana, maj 2022
ISSN 0039-2480

Izhaja mesečno

Razširjeni povzetki (extended abstracts)

Strojniški vestnik - Journal of Mechanical Engineering 68(2022)5, SI 41

Prejeto v recenzijo: 2021-10-12
Prejeto popravljeno: 2022-02-21
Odobreno za objavo: 2022-03-07

Meritev izkoristka reduktorjev električnih gospodarskih vozil med posebnimi voznimi cikli

Tomas Petr –J osef Brousek –J akub Jezek – Tomas Zvolsky –R obert Vozenilek
Tehniška univerza Liberec, Oddelek za vozila in motorja, Češka republika

V predstavljeni študiji je bil preučen izkoristek menjalnika avtonomnega električnega gospodarskega vozila, ki skupaj z izkoristkom elektromotorja pomembno vpliva na njegovo porabo. Predstavljena je metoda za neposredno določitev izkoristka avtonomnega električnega gospodarskega vozila med voznimi cikli z namenom pridobivanja podatkov o vplivu izkoristka menjalnika na porabo teh vozil.

Izkoristek menjalnika je bil izmerjen v treh voznih ciklih, ki simulirajo delovne operacije gospodarskih vozil. Ti cikli so: CARB Heavy Heavy – Duty Diesel Truck Creep Segment, Central Business District Segment of the Transit Coach Operating Duty Cycle in NREL Port Drayage Creep Queue Cycle (Kalifornija). V predstavljeni metodi je bila na preizkuševališču za pogonske sklope izmerjena mehanska moč na vhodu in izhodu menjalnika pri vseh treh ciklih.

Za eksperimentalno določitev izkoristka menjalnika med voznimi cikli so bili na osnovi sil upora, ki delujejo na vozilo med vožnjo, pridobljeni vhodni podatki v obliki vhodnih in izhodnih hitrosti menjalnika ter navora. Vhodni podatki so bili določeni z napredno simulacijo omenjenih ciklov v programski opremi Ricardo Ignite. Med eksperimenti so bile izmerjene vrednosti vhodne in izhodne hitrosti ter navora na menjalniku. Meritve so bile obdelane s programsko opremo Matlab za določitev izkoristka in izgub moči v menjalniku med voznimi cikli.

Izkoristek menjalnika je pri vseh izmerjenih voznih ciklih signifikantno odvisen od vhodnega navora in hitrosti. Pri višjih vrednostih vhodnega navora so bile dosežene vrednosti izkoristka menjalnika okrog 94 %, pri nižjih vrednostih vhodnega navora pa okrog 50 %. Prav slednji režim prevladuje v obravnavanih voznih ciklih in menjalnik zato večino časa obratuje z razmeroma nizkim izkoristkom 50 %.

Slab izkoristek je mogoče pripisati dvema vzrokoma. Prvi so lastnosti in vozni profili uporabljenih voznih ciklov gospodarskih vozil. Ti vozni cikli predstavljajo razmeroma nizko obremenitev in s tem nizek povprečni vhodni navor na menjalniku. Menjalnik je torej večino časa obratoval v območju nizkega vhodnega navora. Drugi možni vzrok so vgrajene komponente iz običajnega menjalnika Škoda MQ200. Zobniki v menjalniku so verjetno optimizirani za višje vrednosti vhodnega navora, pri katerih komponente delujejo z višjim izkoristkom. Za potrditev pravega vzroka slabega izkoristka pri nizkih vrednostih vhodnega navora bodo nujne podrobnejše meritve posameznih podsistemov menjalnika.

Predstavljena metoda za meritev izkoristka menjalnika v voznih ciklih je primerna osnova za nadaljnje raziskave in razvoj menjalnikov za električna vozila. Ugotovljene vrednosti trenutnega izkoristka menjalnika v voznih ciklih specialnih gospodarskih vozil, ki pogosto vozijo z nizko hitrostjo in pod nizkimi obremenitvami, nakazujejo na včasih spregledano dejstvo, da lahko izkoristek menjalnika pomembno vpliva na skupni izkoristek električnega sistema za prenos moči, s tem pa tudi na porabo električnega vozila.

Ključne besede: izkoristek, menjalnik, transmisija, sistem za prenos moči, električni pogon, električno vozilo, vozni cikel

*Naslov avtorja za dopisovanje: Tehniška univerza Liberec, Oddelek za vozila in motorja, Češka republika, tomas.petr@tul.cz

Strojniški vestnik - Journal of Mechanical Engineering 68(2022)5, SI 42

Prejeto v recenzijo: 2021-05-29
Prejeto popravljeno: 2022-01-10
Odobreno za objavo: 2022-03-08

Polaktivna vklopna regulacija vibroizolacijskega sistema

Zeyu Weng* – Shengli Liu – Teqi Xu – Xiaoyu Wu – Zhe Wang – Jie Tang
Tehniška univerza v Zhejiangu, Kolidž za strojništvo, Kitajska

Vibroizolacija tipa 'splav' učinkovito izolira mehanske vibracije in zmanjšuje hrup ladijskih pogonskih sistemov, ima pa tudi svoje pomanjkljivosti. Omenjeni vibroizolacijski sistemi namreč dobro izolirajo vibracije pri višjih frekvencah, medtem ko pri nižjih frekvencah, zlasti v bližini resonančne frekvence, ne dajejo učinka blaženja ali pa vibracije celo okrepijo. Zato je predstavljena nova tehnika polaktivne regulacije vibroizolacije za ladijske pogonske sisteme, ki odpravlja te pomanjkljivosti. V članku so predstavljeni ti glavni raziskovalni cilji:

(1) Opravljen je bil preizkus delovanja vklopnega blažilnika. Preučeni so bili hitrost, poraba moči ter odzivni čas v izključenem in vključenem stanju vklopnega blažilnika. Določeni so bili parametri zmogljivosti vklopnega blažilnika.
(2) Določen je bil analitični model vibroizolacijskega sistema z upogljivimi temelji, vključno z enačbo za popis njegove dinamike. Na podlagi dveh različnih ciljev regulacije sta bila razvita algoritma za polaktivno regulacijo in njuna regulacijska zakona. Prvi algoritem zmanjšuje kinetično energijo splava, drugi pa uravnoveša kinetično energijo splava z najmanjšo vhodno energijo sistema.
(3) Opravljene so bile simulacije originalnega sistema, sistema z vklopnim blažilnikom in sistema z algoritmično reguliranim blažilnikom. Učinkovitost vibroizolacije je bila ocenjena glede na pospeške temeljev. Predstavljena je primerjava razlik v časovnem odzivu osnovnega pospeška vibroizolacijskega sistema v stanju izklopa, v stanju vklopa in z obema algoritmoma. Z analizo trendov krivulj osnovnega pospeška v frekvenčni domeni za originalni sistem, stanje izklopa, stanje vklopa ter za sistema, ki vključujeta prvi in drugi regulacijski algoritem, je bila preverjena učinkovitost regulacijskih algoritmov pri dušenju vibracij. Rezultati simulacij so pokazali, da regulacijska algoritma učinkovito odpravita resonančni pojav ter zmanjšata amplitudo osnovnega pospeška v pasu okrog resonančne frekvence.
(4) Postavljen je bil sistem za preizkušanje vibroizolacijskega sistema s polaktivno regulacijo, ki ga sestavljajo trije glavni deli: preizkuševališče za vibroizolacijski sistem, sistem vklopnega krmilnika in podsistem za analizo. Preučen je bil vpliv pospeškovnega odziva vibroizolacijskega sistema v različnih stanjih in pri različnih frekvencah. Polaktivna regulacija z enim in z drugim algoritmom bolje omejuje vibracije v bližini resonančne frekvence kot nereguliran sistem, medtem ko je učinek blaženja vibracij pri ostalih frekvencah približno enak. Oba algoritma uspešno izboljšata delovanje vibroizolacije okrog resonančne frekvence.

Rezultati simulacij in eksperimentov so pokazali, da se z uvedbo polaktivne regulacije vibroizolacijskih sistemov tipa 'splav' izboljša učinek blaženja vibracij pri nizkih frekvencah, še posebej okrog resonančne frekvence. S tem je potrjena učinkovitost predlaganih regulacijskih algoritmov.

Ključne besede: splav, polaktivna regulacija, vibroizolacija, vklopni algoritem

*Naslov avtorja za dopisovanje: Zhejiang tehnična univerza, Hangzhou, Kitajska, wengzy8888@163.com

Strojniški vestnik - Journal of Mechanical Engineering 68(2022)5, SI 43

Prejeto v recenzijo: 2022-02-09
Prejeto popravljeno: 2022-03-10
Odobreno za objavo: 2022-04-13

Vpliv porazdelitve točk merjenja vibracij in hrupa na njihovo občutljivost pri diagnosticiranju kavitacije črpalk

Runze Zhou[1*] – Hui Chen[2, 3] – Liang Dong[4] – Houlin Liu[4] – Zeyu Chen[1] – Yuhang Zhang[1] – Zhiming Cheng[1]

[1]Univerza Jiangsu Zhenjiang, Raziskovalno središče za fluidno tehniko, Kitajska
[2]Znanstveno-tehnološki laboratorij za raketne motorje na tekoče gorivo, Kitajska
[3]Inštitut za letalsko in vesoljsko pogonsko tehniko Xi'an, Kitajska
[4]Univerza Jiangsu, Nacionalno raziskovalno središče za črpalke, Kitajska

Kavitacija je glavni povzročitelj slabšanja hidravlične učinkovitosti centrifugalnih črpalk in pomemben kazalnik njihove zmogljivosti. Kavitacije ni mogoče popolnoma omejiti in za zanesljivo delovanje črpalk je nujno učinkovito zaznavanje pojava in razvoja kavitacije, kakor tudi izbira ustreznih obratovalnih pogojev, ki kavitacijo vnaprej preprečijo. Proces kavitacije se deli v faze nastanka, razvoja in degradacije. Za različne faze je značilno spreminjanje veličin, kot so tlak, vibracije in raven hrupa. Na podlagi teh sprememb je mogoče napovedovati intenzivnost kavitacije, kar je že potrdilo več raziskav, manjkajo pa študije občutljivosti napovedovanja kavitacije na porazdelitev merilnih točk. Signali vibracij na različnih mestih imajo v praksi različne lastnosti. Učinkovitost napovedovanja kavitacije je v različni meri občutljiva tudi na hrup, ki se prenaša po kapljevini, in na lastnosti tlačnih impulzov. Članek zato obravnava vpliv porazdelitve merilnih točk za vibracije in hrup na občutljivost diagnosticiranja kavitacije, ter določitev optimalnih mest za merilne točke z namenom izboljšanja točnosti in učinkovitosti diagnosticiranja kavitacije. Za točnejše zaznavanje kavitacije je bil preučen vpliv porazdelitve merilnih točk na občutljivost diagnosticiranja kavitacije pri centrifugalnih črpalkah. Predmet raziskave je centrifugalna črpalka s predstopnjo (inducerjem) in delilnimi lopaticami. Za zajem signalov vibracij in hrupa, ki se prenaša po kapljevini, so bili uporabljeni pospeškomeri in hidrofoni v različnih točkah na črpalki. Spekter signala vibracij in hrupa pri različnih vrednostih NPSH je bil konstruiran po metodah kvadratične sredine (RMS) in hitre Fourierjeve transformacije (FFT) za primerjavo občutljivosti merilnih točk na nastanek in razvoj kavitacije. Uporabljena sta bila tudi model turbulence SST k–ω in Zwartov model kavitacije za analizo porazdelitve kavitacijskega volumna v črpalki v različnih fazah kavitacije. S postavitvijo nadzornih točk na izhodu iz rotorja je bila preučena tudi porazdelitev signala tlačnih impulzov v frekvenčni domeni. Izmerjeni so bili tok motorja, tlačni impulzi, vibracije in hrup med kavitacijskim preizkusom s fiksnim ventilom. Signali so bili nato obdelani z izračunom kvadratične sredine, hitro Fourierevo transformacijo in izračunom ravni zvočnega tlaka, temu pa je sledila kvantitativna primerjava občutljivosti napovedovanja kavitacije v različnih merilnih točkah. V kombinaciji z računalniško dinamiko fluidov so bile analizirane lastnosti razvoja kavitacije in tlačnih impulzov v črpalki. Pretok se v fazi razvoja kavitacije zmanjšuje počasneje od sesalne višine. Ko se sesalna višina zmanjša za 3 %, se pretok zmanjša za približno 2,8 %. V določeni meri se zmanjša tudi tok motorja. Ko je vrednost NPSH manjša od 0,5 m, tok naglo upade za približno 12 %. Raven vibracijskih pospeškov se signifikantno poveča v vseh merilnih točkah. Merilni točki na vstopni prirobnici in v osi ohišja črpalke sta občutljivejši za napovedovanje kavitacije in v obeh je bil zabeležen 0,6-odstotni upad. Frekvenčni pas okrog vrha signala hrupa se signifikantno skrči. V delovni točki NPSHr se raven zvočnega tlaka oz. hrupa na vstopu zmanjša za 14 %, na izstopu pa za 1 %. Za napovedovanje kavitacije je zato primernejša vstopna merilna točka za hrup, ki se prenaša po kapljevini. Intenzivnost tlačnih impulzov na vhodu se zmanjšuje, medtem ko je trend na izhodu ravno obraten. Spremembe intenzivnosti tlačnih impulzov so bolj izražene na vhodu kot na izhodu. Ko se sesalna višina zmanjša za 3 %, se intenzivnost impulzov zmanjša za 66,3 % na vhodu in za 13,9 % na izhodu. Glavna frekvenca signala tlačnih impulzov je porazdeljena okrog frekvence prehoda lopatic fBPF. Z razvojem kavitacije se pojavita vpliv harmonikov na glavno frekvenco in premik nekaterih glavnih frekvenc. Merilne točke za vibracije, hrup v kapljevini in tlačne impulze na vstopni prirobnici in v osi ohišja črpalke imajo dobro občutljivost in so primerne za diagnosticiranje kavitacije.

Predlagano razporeditev merilnih točk za diagnosticiranje kavitacije bo mogoče uporabiti tudi pri drugih črpalkah. Metodo bo mogoče razširiti za diagnosticiranje ostalih napak pri črpalkah, kot so poškodbe rotorja, napake poravnave gredi in neuravnoteženost gredi. Zaradi mejnih vrednosti napovedovanja signalov napak je treba vsakokrat upoštevati značilnosti in zahteve za konkretno vrsto črpalke.

V nadaljnjih študijah bo mogoče natančnost diagnosticiranja kavitacije še dodatno izboljšati. Članek razkriva spektralne lastnosti tlačnih impulzov, vibracij in hrupa pri centrifugalnih črpalkah, ko se razvije kavitacija. Preskusi kavitacije so bili opravljeni s fiksnim ventilom in ta metoda je bolj realistična. Preverjena je bila občutljivost metode diagnosticiranja kavitacije in predlagana je optimalna porazdelitev merilnih točk. Članek tako ponuja izhodišča za izboljševanje učinkovitosti in točnosti diagnosticiranja kavitacije.

Ključne besede: diagnosticiranje kavitacije, centrifugalna črpalka, vibracije in hrup, občutljivost merilnih točk, spektralna analiza

*Naslov avtorja za dopisovanje: Univerza Jiangsu Zhenjiang, Raziskovalno središče za fluidno tehniko, Kitajska, 798917967@qq.com

Strojniški vestnik - Journal of Mechanical Engineering 68(2022)5, SI 44

Prejeto v recenzijo: 2022-01-07
Prejeto popravljeno: 2022-02-14
Odobreno za objavo: 2022-03-01

Optimizacija mesta pritrditve masnih blažilnikov za boljše omejevanje drdranja pri tankostenskem rezkanju

Mohanraj Selvakumar[1]* – Prabhu Raja Venugopal[1] – Gautham Velayudhan[1]
[1]Tehniški kolidž PSG, Oddelek za strojništvo, Indija

Regenerativno drdranje je vrsta samovzbujenih vibracij, ki se pojavljajo med rezkanjem in med drugimi obdelovalnimi postopki, zanj pa je značilno črpanje energije za začetek in rast iz interakcij med rezalnim orodjem in obdelovancem. Zaradi drdranja se pojavi nestabilnost sistema, ki je nezaželena in je ni mogoče preprosto obvladati. Drdranje med drugim povzroča slabo kakovost obdelanih površin, skrajšanje obstojnosti orodja, nižjo stopnjo odvzema materiala in hrupnost obdelave. Običajno se pojavi zaradi najbolj gibkega elementa v dinamični verigi strukture. Pri tankostenskem rezkanju, ki je eden od glavnih obdelovalnih postopkov za izdelavo lahkih monolitnih delov v letalski in vesoljski industriji, je najbolj gibek del obdelovanec, zato se pojavlja vse več raziskav o stabilnosti tankostenskih delov proti drdranju. Drdranje je mogoče omejiti s primerno tehniko za modifikacijo struktur.

Masni blažilniki so učinkovito sredstvo za omejevanje drdranja pri vsakem procesu obdelave z odrezavanjem. So razmeroma preprosta in cenena rešitev za zmanjšanje drdranja z dodajanjem sistema vzmeti in mase k glavni strukturi. Pri oblikovanju masnih blažilnikov se običajno uporabijo parametri, ki ustrezajo dominantni lastni obliki strukture, pritrdijo pa se na mesto, kjer je amplituda vibracij največja. Opisani pristop ne zagotavlja vedno optimalnih rezultatov pri tankostenskem rezkanju, vzrok pa je v lahkih obdelovancih. Pravo mesto za masni blažilnik na obdelovancu je zato treba določiti ob upoštevanju mase blažilnika. Uporaba masnih blažilnikov za grobo rezkanje ni primerna, saj se zaradi velike količine odstranjenega materiala močno spreminja dinamika strukture, površinska hrapavost pa je pri teh obdelavah tudi manj pomembna. Drdranju se je treba izogniti med končno obdelavo, saj je od tega odvisna kakovost površine izdelkov. Stabilnost tankih sten proti drdranju med končno obdelavo je mogoče izboljšati z namestitvijo masnega blažilnika na površino, ki leži nasproti obdelovane tanke stene.

V članku je predstavljena metoda na osnovi numeričnih tehnik za optimizacijo mesta pritrditve masnih blažilnikov, namenjena izboljšanju stabilnosti tankostenskih obdelovancev proti drdranju, ki upošteva vpliv mase blažilnikov. Dominantna oblika obdelovanca je določena na podlagi simuliranega in izmerjenega frekvenčnega odziva obdelovanca. Razvita sta bila dva masna blažilnika z eno prostostno stopnjo in njun model po metodi končnih elementov za napovedovanje odziva sistema obdelovanca in blažilnika. Preučen je bil tudi vpliv mesta pritrditve blažilnika na stabilnost tankostenskega obdelovanca proti drdranju. Mesto pritrditve masnega blažilnika je bilo optimizirano po metodi odzivnih površin za še boljšo stabilnost obdelovanca proti drdranju. Na obdelovancih z masnimi blažilniki in brez njih so bili opravljeni udarni preskusi. Pri obdelovancih z enim oziroma dvema masnima blažilnikoma je bilo ugotovljeno 32- oz. 60-odstotno izboljšanje dinamične stabilnosti. Ugotovljeno je bilo, da je uporaba enega masnega blažilnika učinkovita le na prvi polovici poti rezkarja. Za izboljšanje stabilnosti proti drdranju po celotni poti orodja sta potrebna dva masna blažilnika. Opravljeni so bili tudi testi protismernega rezkanja na obdelovancih z masnimi blažilniki in brez njih za validacijo predlagane metodologije. Preskusi so pokazali, da prinaša uporaba masnih blažilnikov 60-odstotno izboljšanje celotne dinamične stabilnosti obdelovanca, kar ustreza trikratnemu izboljšanju produktivnosti ob 38-odstotni izboljšavi površinske hrapavosti.

Ključne besede: drdranje, tankostensko rezkanje, masni blažilnik, optimizacija po metodi odzivnih površin

*Naslov avtorja za dopisovanje: Tehniški kolidž PSG, Oddelek za strojništvo, Indija, smr.mech@psgtech.ac.in

Strojniški vestnik - Journal of Mechanical Engineering 68(2022)5, SI 45

Prejeto v recenzijo: 2021-12-30
Prejeto popravljeno: 2022-02-24
Odobreno za objavo: 2022-02-24

Napovedovanje časovne trdnosti sočelnih zvarov z napakami na več mestih

Ebron Shaji* - Prabhu Raja Venugopal - Gautham Velayudhan - Mohanraj Selvakumar
Tehniški kolidž PSG, Oddelek za strojništvo, Indija

Sočelno varjenje je postopek za preprosto in trdno spajanje raznih komponent. Utrujenostne lastnosti zvarov so sicer dobre, napake v zvarih, kot so nepopolna prevaritev, nepopolna spojitev, zajede in poroznost, pa lahko privedejo do porušitve. Napaka v zvaru lahko v pogojih cikličnih obremenitev povzroči nastanek razpoke, rast razpoke v zvaru pa običajno pripelje do porušitve zvara. Trajanje rasti razpoke je odvisno od hitrosti rasti začetne razpoke do kritične velikosti, napovedati pa ga je mogoče s faktorjem intenzitete napetosti (SIF) na konici razpoke. V priročnikih so sicer na voljo enačbe za računanje vrednosti faktorja SIF za preprostejše zvarne spoje, toda iskanje primernih rešitev za konstrukcije z različnimi oblikami zvarov ter kompleksnimi geometrijami in obremenitvami je težavno.

Pričujoča študija obravnava prisotnost napak na različnih mestih v zvaru, vrste obremenitev, vrste napak in njihovo velikost. Napake v zvaru so bile modelirane kot poleliptične razpoke na osnovi priporočil IIW za konstruiranje zvarnih spojev in komponent na utrujanje. Faktor intenzitete napetosti v bližini napak je bil ocenjen z integralom M, čas rasti pa je bil izračunan po Parisovem zakonu s programsko opremo Fracture Analysis Code (FRANC3D). Glavna cilja študije sta napoved in rangiranje vpliva napak v zvarih na časovno trdnost sočelnih zvarnih spojev.

Za izdelavo sočelnih zvarnih spojev je bilo izbrano jeklo ASTM A517 kakovosti F. Za začetne dimenzije napak v zvaru so bile določene največje dopustne vrednosti iz meril za sprejemljivost zvarov po ASME B31.3. Napake v zvarih so bile modelirane kot ekvivalentne razpoke, rast razpok pa je bila simulirana s programsko opremo za simulacije FRANC3D. Obravnavani problem ima veliko spremenljivk, zato je bila izbrana faktorska zasnova po metodi Taguchi s petimi faktorji in tremi ravnmi. Za vsak podatkovni set v matriki zasnove je bila določena časovna trdnost sočelnega zvara s programsko opremo FRANC3D. Razmerje med signalom in šumom (S/N) je bilo določeno po kriteriju »več je bolje«. Za določitev časovne trdnosti sočelnega zvara je bil razvit kvadratični model drugega reda. V izbrani empirični formuli je upoštevan vpliv posameznih faktorjev in njihovih medsebojnih interakcij. Za validacijo empiričnega modela je bila opravljena eksperimentalna raziskava z značilnim podatkovnim setom.

Iz razmerja S/N izhaja, da ima vrsta obremenitev največji vpliv med obravnavanimi kontrolnimi dejavniki. Faktor L1 (natezna obremenitev) ima nižje razmerje S/N kot ostali dve vrsti obremenitev, kar pomeni, da je natezna obremenitev bolj kritična. Analiza vpliva napak v zvarih na časovno trdnost je pokazala, da pomanjkljiva prevaritev in zajede privedejo do minimalne trajne trdnosti, ko je zvarni spoj izpostavljen čistim membranskim napetostim. V prisotnosti več napak oz. pri kombiniranem vplivu treh napak z dodanima napakama na eni četrtini ali na treh četrtinah dolžine zvara je zmanjšanje časovne trdnosti signifikantno večje kot v prisotnosti napake sredi zvara. Primerjava rezultatov eksperimentov in empiričnega modela je pokazala 14-odstotno odstopanje časovne trdnosti. Odstopanje med napovedmi numeričnega in empiričnega modela je 4-odstotno, kar vliva zaupanje v uporabo numeričnega postopka in empiričnega modela za določanje časa rasti razpoke.

V predstavljenem delu je bila kot glavni parameter namesto obremenitve uporabljena napetost. Napake so modelirane parametrično in velikost napak je zato sorazmerna z geometrijskimi dimenzijami plošče. Rezultati so neodvisni od geometrije in splošno veljavni.

Ključne besede: sočelni spoj, napake v zvarih, rast razpok, utrujenostne obremenitve, časovna trdnost, zasnova eksperimentov

*Naslov avtorja za dopisovanje: Tehniški kolidž PSG, Oddelek za strojništvo, Indija, 1601rm01@psgtech.ac.in

Strojniški vestnik - Journal of Mechanical Engineering 68(2022)5, SI 46

Prejeto v recenzijo: 2021-11-11
Prejeto popravljeno: 2022-03-14
Odobreno za objavo: 2022-03-28

Večciljna optimizacija tribološkega vedenja kompozitov na osnovi PTFE pri manjših obremenitvah s sivo relacijsko analizo po Taguchiju

Musa Alhaji Ibrahim[1,2,*] – Hüseyin Çamur[2] – Mahmut A. Savaş[2] – Alhassan Kawu Sabo[3]

[1] Znanstveno-tehniška univerza zvezne države Kano, Tehniška fakulteta, Nigerija
[2] Univerza Bližnjega vzhoda, Tehniška univerza Mersin, Ciper
[3] Znanstveno-tehniška univerza zvezne države Kano, Enota za projektiranje in razvoj, Nigerija

Polimerni kompoziti so se uveljavili v avtomobilski in letalski industriji ter v gradbeništvu zaradi svoje visoke specifične trdnosti in togosti. Prav zaradi teh dveh glavnih lastnosti so v prednosti v primerjavi z monolitnimi kovinami oziroma z njihovimi zlitinami. Zanje so značilni tudi obstojnost proti koroziji, majhno trenje, preprosta izdelava ter dušenje hrupa in vibracij. Abrazivna obraba je pogosta pri rudarski opremi, gradbeni mehanizaciji in transportnih drčah v termoelektrarnah.

Glavni cilj pričujoče študije je optimizacija triboloških parametrov (sila, velikost zrn ter drsna razdalja) in njihovega vpliva na abrazivne tribološke lastnosti kompozitov na osnovi politetrafluoroetilena (PTFA) pri lažjih obremenitvah s hibridno sivo relacijsko analizo po Taguchiju.

Oblikovano je bilo ortogonalno polje Taguchi L_9 in izvedenih je bilo devet nizov eksperimentov na tribometru. Pri vsakem eksperimentu sta bila zabeležena količnik trenja (μ) in specifična stopnja abrazivne obrabe (A_w). Nato je bila opravljena analiza variance (ANOVA) za določitev parametra z največjim vplivom na abrazivne tribološke lastnosti kompozitov. Glede vpliva sile, drsne razdalje in velikosti zrn na vrednost μ je bilo ugotovljeno, da se količnik trenja povečuje od 5 N do 8 N in nato zmanjšuje od 8 N do 10 N. Povečanje velikosti zrn in drsne razdalje je povzročilo linearno zmanjšanje vrednosti μ. Povečanje sile, velikosti zrn in drsne ojačitve je podobno povzročilo zmanjšanje vrednosti Aw. Enkratna optimizacija po metodi Taguchi je pokazala, da so optimalni pogoji za želeno vrednost μ doseženi pri sili 10 N, velikosti odprtine 1000 in razdalji 350 m. Napovedana optimalna kombinacija procesnih parametrov je bila kodirana z oznako L9_D3. Tudi ocenjeni optimalni parametri za minimalno vrednost A_w so sila 10 N, velikost odprtine 1000 in drsna razdalja 350 m (koda L9_D3).

Rezultati analize ANOVA so pokazali, da na vrednost μ najbolj signifikantno vpliva velikost zrn, temu pa sledita sila in drsna razdalja. Prispevki sile, velikosti zrn in drsne razdalje znašajo 14,62 %, 69,34 % in 6,94 %. Podobno tudi na vrednost Aw signifikantno vplivajo velikost zrn, drsna razdalja in sila, njihovi prispevki pa znašajo 42,64 %, 23,40 % in 15,05 %. Rezultati sive relacijske analize po Taguchiju so pokazali, da je optimalna kombinacija parametrov sila 10 N, velikost zrn 1000 in drsna razdalja 350 m (koda L9_D3). Analiza variance je razkrila, da je velikost zrn s prispevkom 67,69 % najpomembnejši parameter abrazivnega tribološkega vedenja ojačenih kompozitov na osnovi PTFE. Validacijski preskusi z optimalno kombinacijo parametrov so pokazali 55,22-odstotno izboljšanje sive relacijske stopnje.

Študija je bila omejena le na manjše obremenitve. V prihodnjih raziskavah bo mogoče preučiti tribološke lastnosti pri večjih obremenitvah ter zbrati več podatkov za razvoj modelov umetne inteligence za napovedovanje sive relacijske stopnje. Študija daje prispevek k raziskavam obrabne obstojnosti polimernih kompozitov s kombiniranjem odzivov μ in A_w v enem samem odzivu.

Sledi sklep, da je optimalna kombinacija parametrov za ta odziv enaka optimalni kombinaciji za zmanjšanje μ in A_w in s tem prinaša prihranek pri stroških, energiji in času.

Ključne besede: PTFE, ogljikova vlakna, bronasta vlakna, abraziv, Taguchi, siva relacijska analiza

*Naslov avtorja za dopisovanje: Znanstveno-tehniška univerza zvezne države Kano, Tehniška fakulteta, Nigerija, musaibrahim@kustwudil.edu.ng

Strojniški vestnik - Journal of Mechanical Engineering 68(2022)5, SI 47

Prejeto v recenzijo: 2021-12-30
Prejeto popravljeno: 2022-03-13
Odobreno za objavo: 2022-03-28

Numerična analiza sistema dvostopenjskega ejektorja-difuzorja na osnovi konstantne hitrosti sprememb kinetične energije

Virendra Kumar[1] – Anil Kumar[2] – Surendra Kumar Yadav[3] – Anshul Yadav[4] – Lalta Prasad[5] – Jerzy Winczek[6] *

[1] Kolidž za inženiring in tehnologijo Noida, Indija
[2] Inštitut za tehnologijo Kamla Nehru, Indija
[3] Univerza K R Mangalam, Gurugram, Indija
[4] CSIR - centralni inštitut za raziskave soli in morskih kemikalij, Indija
[5] Nacionalni inštitut za tehnologijo Uttarakhand, Indija
[6] Tehniška univerza v Čenstohovi, Poljska

Preprosta zgradba in zanesljivost sta glavna razloga pogoste uporabe ejektorjev za črpanje, induciranje, mešanje in/ali rekomprimiranje primarnega/pogonskega in dveh sekundarnih/induciranih tokov. Uporabljajo se v industrijskih aplikacijah hlajenja, klimatizacije, sistemih za desalinizacijo morske vode, kemičnih laserjih, gorivnih celicah itd. Konvencionalni enostopenjski ejektorji (SSE) izkoriščajo načeli mešanja s konstantnim presekom (CAM) in mešanja s konstantnim tlakom (CPM). Slabost ejektorjev je nizek izkoristek zaradi izgub v mešalni komori in termodinamičnega šoka v difuzorju konstantnega preseka. Raziskovalci so se lotili omenjenega problema s fizikalnim enodimenzionalnim plinskodinamičnim pristopom konstantne hitrosti spremembe gibalne količine (CRCM) in s pristopom konstantne spremembe kinetične energije (CRKEC). Zasnova ejektorjev tako danes prehaja iz enostopenjske v dvo- oz. večstopenjsko. Dvostopenjska kompresija je drug način za zmanjšanje izgub zaradi dušenja in za izboljšanje učinkovitosti sistema. Enostopenjski ejektor ima vhod za primarni tok, vhod za sekundarni/inducirani tok, mešalno komoro in difuzor. Drugi inducirani/nošeni tok vstopa pri dvostopenjskih ejektorjih na izhodu mešalnega odseka SSE. Na ta način je bolje izkoriščeno praznjenje odvečne gibalne količine na izhodu mešanja prve stopnje ejektorja. Sistem ima običajno en vhod za pogonski tok in dva vhoda za inducirani tok (primarni in sekundarni). Sekundarni inducirani tok pospešuje kombinirani (primarni pogonski in inducirani) tok iz prve stopnje. Proces izmenjave gibalne količine med pogonskim in induciranim tokom pogosto imenujemo odnašanje. Stopnja odnašanja je globalni zmogljivostni parameter, predstavlja pa razmerje med masnima pretokoma induciranega in pogonskega toka. Opisani pristop omogoča zmanjšanje termodinamičnega šoka v difuzorju ejektorja v projektirani delovni točki.

V predstavljeni študiji je bil uporabljen enodimenzionalni plinskodinamični pristop CRKEC za projektiranje SSE in dvostopenjskega ejektorja (TSE) za vodno paro. Geometrijske koordinate posameznih komponent SSE in TSE so bile izračunane lokalno v programskem paketu MATLAB z malim korakom (d = 0,5 mm). Izračunana geometrija ejektorjev je bila numerično analizirana s komercialno programsko opremo ANSYS Fluent. Problem za numerično analizo je dvodimenzijski osnosimetrični stacionarni turbulentni stisljivi tok. Mreža računske domene je bila oblikovana s strukturiranimi četverorobimi elementi. Za točnejše rezultate je bilo uporabljenih več celic v predelih z višjim hitrostnim gradientom. Za analizo neodvisnosti rezultatov od mreže je bil uporabljen standardni model turbulence k–ε. Relativna razdalja izhodnega položaja šobe (NXP) od mešalne komore za primarno šobo je bila nastavljena na nič. Predstavljena je primerjava zmogljivosti dvostopenjskega ejektorja in pretočnih lastnosti v primerjavi z enostopenjskim ejektorjem. Ugotovljeno je bilo, da je rekuperacija tlaka na izhodu enostopenjskega ejektorja večja kot pri dvostopenjskem ejektorju. Globalni zmogljivostni parameter stopnja odnašanja (ω), ki je izračunan kot razmerje med induciranim in pogonskim masnim pretokom, se izboljša za 70 % z vključitvijo druge stopnje. Ugotovljeno je bilo tudi zmanjšanje tlačnih nihanj zaradi mešanja primarnega nadzvočnega toka in sekundarnega podzvočnega toka v primerjavi z enostopenjskim ejektorjem. Pristop CRKEC pomaga pri računanju geometrijskega profila in pretočnih karakteristik z malimi koraki. Za podrobnejšo analizo zmogljivosti bodo potrebni še preskusi delovanja prototipov TSE, narejenih po pristopu CRKEC, zunaj projektirane delovne točke.

Ključne besede: ejektor, CRKEC, dvostopenjski ejektor, enostopenjski ejektor, CFD, curkovna črpalka, CRMC

*Naslov avtorja za dopisovanje: Tehniška univerza v Čenstohovi, 42-201 Częstochowa, Poljska, winczek@gmail.com

Prof.d r.K arl Kuzman

Zapustil nas je redni profesor Fakultete za strojništvo Univerze v Ljubljani in član Uredniškega odbora revije Strojniški vestnik prof. dr. Karl Kuzman. Bil je leta 1941 rojen Vitanjčan, ki je mladostna leta preživel neposredno ob tovarni Unior. Šolal se je na gimnaziji v Celju, kjer je srednješolsko izobraževanje končal leta 1960. Vpisal se je na Fakulteto za strojništvo Univerze v Ljubljani, kjer je leta 1965 diplomiral pri prof. dr. Francu Golograncu.

Po krajši zaposlitvi v Uniorju se je leta 1967 vrnil na Fakulteto za strojništvo Univerze v Ljubljani kot asistent in leta 1972 tudi magistriral. Vrnil se je v Zreče, kjer je med leti 1973 in 1978 bil na različnih vodilnih funkcijah Uniorja.

Leta 1978 se je vrnil na Fakulteto za strojništvo Univerze v Ljubljani, kjer je leta 1984 doktoriral pri mentorju prof. dr. Ervinu Prelogu in somentorju prof. dr. Vincencu Čižmanu. Leta 1988 je prevzel vodenje Katedre za obdelovalno tehniko ter ob upokojitvi prof. dr. Franca Gologranca tudi vodenje Laboratorija za preoblikovanje. Njegovo raziskovalno delo je obsegalo širok opus s področij: termo-mehanskega kovanja, kovaškega valjanja, lamelnih preoblikovalnih orodij, hladnega iztiskavanja jekel, simulacij procesov hladnega preoblikovanja z numeričnimi metodami, zagotavljanja geometrijske natančnosti preoblikovanih izdelkov, oblikovanja predhodno hladno preoblikovanih izdelkov in energijskega vrednotenja procesov preoblikovanja.

Kot vrhunski strokovnjak je bil prof. dr. Karl Kuzman član več mednarodnih znanstvenih združenj ter sodeloval s številnimi priznanimi znanstveniki v tujini. Intenzivno je sodeloval s Prof. Dr.-Ing. Kurtom Langejem iz Stuttgarta in Prof. Dr.-Ing. Manfredom Geigerjem s Friedrich-Alexander-Universität Erlangen-Nürnberg v Nemčiji. V okviru projekta TEMPUS je omogočil tudi izmenjave na doktorski šoli, kar je vodilo v podpis pogodbe o sodelovanju med fakultetama v Ljubljani in Erlangnu ter razširitvi sodelovanja z Univerzama v Eindhovenu na Nizozemskem in Lyngby na Danskem. Bil je član mednarodnega združenja za hladno kovanje ICFG, kateremu je tudi predsedoval med leti 2003 in 2007 V svoji znanstveni karieri je aktivno sodeloval tudi v mednarodnem združenju za preoblikovanje pločevine IDDGR. Že zelo zgodaj je razumel pomembnost obravnave ekoloških tem v proizvodnji, zato se je pridružil mednarodnem komiteju za ekologijo in ekonomijo ICEM. Najbolj ponosen je bil na članstvo v Mednarodni akademiji za obdelovalne tehnologije CIRP. Bil je avtor več kot 300 znanstvenih člankov in konferenčnih prispevkov ter soavtor enega patenta.

Leta 1990 je prof. dr. Karl Kuzman prejel od Vlade Republike Slovenije nagrado Sklada Borisa Kidriča za izume in izboljšave na področju tehnike, leta 1994 pa plaketo in priznanje za sodelovanje s Tehniško fakulteto iz Maribora. Leta 200 je za uvajanje inkrementalnega preoblikovanja na fasadne panele v sodelovanju s podjetjem Trimo Trebnje dobil mednarodno prestižno nagrado RedDot award, Architecture and interior design.

Na osnovi profesorjeve ideje razvojne pomoči slovenskim orodjarjem je kot član Odbora za orodjarstvo pri GZS bil pobudnik za ustanovitev zavoda TECOS, Razvojnega centra orodjarstva Slovenije, ki je bil ustanovljen leta 9 v Celju. TECOS je dolgo let vodil kot prvi direktor. Na Ministrstvu za znanost in tehnologije je prof. dr. Karl Kuzman bil v letih 1993/94 namestnik nacionalnega koordinatorja raziskovalnega polja Proizvodne tehnologije in sistemi, od leta 9 pa nacionalni koordinator.

Predvsem pa je bil prof. dr. Karl Kuzman enkraten predavatelj in pedagog Fakultete za strojništvo Univerze v Ljubljani. Svojo profesorsko pot je pričel leta 1978 in bil od leta 1996 redni profesor. Dekan Fakultete za strojništvo je bil med leti 2005 in 2007. Bil je mentor več kot 300 študentom, 16 magistrantom in 10 doktorandom. Za študente je pripravil zgledni študijski gradivi Vaje iz tehnike preoblikovanja in Tehnološke karakteristike preoblikovalnih strojev. Sodeloval je tudi pri izdelavi in sourejanju Strojno-tehnološkega priročnika pod uredništvom prof. dr. Hinka Murna, ki je izšel pri Tehniški založbi in je bila ponatisnjen v štirih ponatisih. Prof. dr. Karl Kuzman je bil tudi redaktor leta 2010 izdanega priročnika proizvodnega strojništva Moderno proizvodno inženirstvo.

Sodelavci in njegovi študenti bomo profesorja Kuzmana ohranili v trajnem spominu.

Zapisal: izr. prof. dr. Tomaž Pepelnjak,
član Uredniškega odbora SV-JME

Guide for Authors

All manuscripts must be in English. Pages should be numbered sequentially. The manuscript should be composed in accordance with the Article Template given above. The suggested length of contributions is 10 to 20 pages. Longer contributions will only be accepted if authors provide justification in a cover letter. For full instructions see the Information for Authors section on the journal's website: http://en.sv-jme.eu .

SUBMISSION:

Submission to SV-JME is made with the implicit understanding that neither the manuscript nor the essence of its content has been published previously either in whole or in part and that it is not being considered for publication elsewhere. All the listed authors should have agreed on the content and the corresponding (submitting) author is responsible for having ensured that this agreement has been reached. The acceptance of an article is based entirely on its scientific merit, as judged by peer review. Scientific articles comprising simulations only will not be accepted for publication; simulations must be accompanied by experimental results carried out to confirm or deny the accuracy of the simulation. Every manuscript submitted to the SV-JME undergoes a peer-review process.

The authors are kindly invited to submit the paper through our web site: http://ojs.sv-jme.eu. The Author is able to track the submission through the editorial process - as well as participate in the copyediting and proofreading of submissions accepted for publication - by logging in, and using the username and password provided.

SUBMISSION CONTENT:

The typical submission material consists of:

- A **manuscript** (A PDF file, with title, all authors with affiliations, abstract, keywords, highlights, inserted figures and tables and references),
- Supplementary files:
  - a **manuscript** in a WORD file format
  - a **cover letter** (please see instructions for composing the cover letter)
  - a ZIP file containing **figures** in high resolution in one of the graphical formats (please see instructions for preparing the figure files)
  - possible **appendicies** (optional), cover materials, video materials, etc.

Incomplete or improperly prepared submissions will be rejected with explanatory comments provided. In this case we will kindly ask the authors to carefully read the Information for Authors and to resubmit their manuscripts taking into consideration our comments.

COVER LETTER INSTRUCTIONS:

Please add a **cover letter** stating the following information about the submitted paper:

1. Paper **title**, list of **authors** and their **affiliations**. **One** corresponding author should be provided.
2. **Type of paper**: original scientific paper (1.01), review scientific paper (1.02) or short scientific paper (1.03).
3. A **declaration** that neither the manuscript nor the essence of its content has been published in whole or in part previously and that it is not being considered for publication elsewhere.
4. State the **value of the paper** or its practical, theoretical and scientific implications. What is new in the paper with respect to the state-of-the-art in the published papers? Do not repeat the content of your abstract for this purpose.
5. We kindly ask you to suggest at least two **reviewers** for your paper and give us their names, their full affiliation and contact information, and their scientific research interest. The suggested reviewers should have at least two relevant references (with an impact factor) to the scientific field concerned; they should not be from the same country as the authors and should have no close connection with the authors.

FORMAT OF THE MANUSCRIPT:

The manuscript should be composed in accordance with the Article Template. The manuscript should be written in the following format:

- A **Title** that adequately describes the content of the manuscript.
- A list of **Authors** and their **affiliations**.
- An **Abstract** that should not exceed 250 words. The Abstract should state the principal objectives and the scope of the investigation, as well as the methodology employed. It should summarize the results and state the principal conclusions.
- 4 to 6 significant **key words** should follow the abstract to aid indexing.
- 4 to 6 **highlights;** a short collection of bullet points that convey the core findings and provide readers with a quick textual overview of the article. These four to six bullet points should describe the essence of the research (e.g. results or conclusions) and highlight what is distinctive about it.
- An **Introduction** that should provide a review of recent literature and sufficient background information to allow the results of the article to be understood and evaluated.
- A **Methods** section detailing the theoretical or experimental methods used.
- An **Experimental section** that should provide details of the experimental set-up and the methods used to obtain the results.
- A **Results** section that should clearly and concisely present the data, using figures and tables where appropriate.
- A **Discussion** section that should describe the relationships and generalizations shown by the results and discuss the significance of the results, making comparisons with previously published work. (It may be appropriate to combine the Results and Discussion sections into a single section to improve clarity.)
- A **Conclusions** section that should present one or more conclusions drawn from the results and subsequent discussion and should not duplicate the Abstract.
- **Acknowledgement** (optional) of collaboration or preparation assistance may be included. Please note the source of funding for the research.
- **Nomenclature** (optional). Papers with many symbols should have a nomenclature that defines all symbols with units, inserted above the references. If one is used, it must contain all the symbols used in the manuscript and the definitions should not be repeated in the text. In all cases, identify the symbols used if they are not widely recognized in the profession. Define acronyms in the text, not in the nomenclature.
- **References** must be cited consecutively in the text using square brackets [1] and collected together in a reference list at the end of the manuscript.
- **Appendix(-icies)** if any.

SPECIAL NOTES

Units: The SI system of units for nomenclature, symbols and abbreviations should be followed closely. Symbols for physical quantities in the text should be written in italics (e.g. *v*, *T*, *n*, etc.). Symbols for units that consist of letters should be in plain text (e.g. ms^{-1}, K, min, mm, etc.). Please also see: http://physics.nist.gov/cuu/pdf/sp811.pdf .

Abbreviations should be spelt out in full on first appearance followed by the abbreviation in parentheses, e.g. variable time geometry (VTG). The meaning of symbols and units belonging to symbols should be explained in each case or cited in a **nomenclature** section at the end of the manuscript before the References.

Figures (figures, graphs, illustrations digital images, photographs) must be cited in consecutive numerical order in the text and referred to in both the text and the captions as Fig. 1, Fig. 2, etc. Figures should be prepared without borders and on white grounding and should be sent separately in their original formats. If a figure is composed of several parts, please mark each part with a), b), c), etc. and provide an explanation for each part in Figure caption. The caption should be self-explanatory. Letters and numbers should be readable (Arial or Times New Roman, min 6 pt with equal sizes and fonts in all figures). Graphics (submitted as supplementary files) may be exported in resolution good enough for printing (min. 300 dpi) in any common format, e.g. TIFF, BMP or JPG, PDF and should be named Fig1.jpg, Fig2.tif, etc. However, graphs and line drawings should be prepared as vector images, e.g. CDR, AI. Multi-curve graphs should have individual curves marked with a symbol or otherwise provide distinguishing differences using, for example, different thicknesses or dashing.

Tables should carry separate titles and must be numbered in consecutive numerical order in the text and referred to in both the text and the captions as Table 1, Table 2, etc. In addition to the physical quantities, such as *t* (in italics), the units [s] (normal text) should be added in square brackets. Tables should not duplicate data found elsewhere in the manuscript. Tables should be prepared using a table editor and not inserted as a graphic.

REFERENCES:

A reference list must be included using the following information as a guide. Only cited text references are to be included. Each reference is to be referred to in the text by a number enclosed in a square bracket (i.e. [3] or [2] to [4] for more references; do not combine more than 3 references, explain each). No reference to the author is necessary.

References must be numbered and ordered according to where they are first mentioned in the paper, not alphabetically. All references must be complete and accurate. Please add DOI code when available. Examples follow.

Journal Papers:

Surname 1, Initials, Surname 2, Initials (year). Title. *Journal*, volume, number, pages, DOI code.

[1] Hackenschmidt, R., Alber-Laukant, B., Rieg, F. (2010). Simulating nonlinear materials under centrifugal forces by using intelligent cross-linked simulations. *Strojniški vestnik - Journal of Mechanical Engineering,* vol. 57, no. 7-8, p. 531-538, DOI:10.5545/sv-jme.2011.013.

Journal titles should not be abbreviated. Note that journal title is set in italics.

Books:

Surname 1, Initials, Surname 2, Initials (year). Title. Publisher, place of publication.

[2] Groover, M.P. (2007). *Fundamentals of Modern Manufacturing*. John Wiley & Sons, Hoboken.

Note that the title of the book is italicized.

Chapters in Books:

Surname 1, Initials, Surname 2, Initials (year). Chapter title. Editor(s) of book, book title. Publisher, place of publication, pages.

[3] Carbone, G., Ceccarelli, M. (2005). Legged robotic systems. Kordić, V., Lazinica, A., Merdan, M. (Eds.), Cutting Edge Robotics. Pro literatur Verlag, Mammendorf, p. 553-576.

Proceedings Papers:

Surname 1, Initials, Surname 2, Initials (year). Paper title. Proceedings title, pages.

[4] Štefanić, N., Martinčević-Mikić, S., Tošanović, N. (2009). Applied lean system in process industry. *MOTSP Conference Proceedings*, p. 422-427.

Standards:

Standard-Code (year). Title. Organisation. Place.

[5] ISO/DIS 16000-6.2:2002. *Indoor Air – Part 6: Determination of Volatile Organic Compounds in Indoor and Chamber Air by Active Sampling on TENAX TA Sorbent, Thermal Desorption and Gas Chromatography using MSD/FID.* International Organization for Standardization. Geneva.

WWW pages:

Surname, Initials or Company name. Title, from http://address, date of access.

[6] Rockwell Automation. Arena, from *http://www.arenasimulation.com,* accessed on 2009-09-07.

EXTENDED ABSTRACT:

When the paper is accepted for publishing, the authors will be requested to send an **extended abstract** (approx. one A4 page or 3500 to 4000 characters or approx. 600 words). The instruction for composing the extended abstract are published on-line: http://www.sv-jme.eu/information-for-authors/ .

COPYRIGHT:

Authors submitting a manuscript do so on the understanding that the work has not been published before, is not being considered for publication elsewhere and has been read and approved by all authors. The submission of the manuscript by the authors means that the authors automatically agree to publish the paper uder CC-BY 4.0 Int. or CC-BY-NC 4.0 Int. when the manuscript is accepted for publication. All accepted manuscripts must be accompanied by a Copyright Agreement, which should be sent to the editor. The work should be original work by the authors and not be published elsewhere in any language without the written consent of the publisher. The proof will be sent to the author showing the final layout of the article. Proof correction must be minimal and executed quickly. Thus it is essential that manuscripts are accurate when submitted. Authors can track the status of their accepted articles on https://en.sv-jme.eu/.

PUBLICATION FEE:

Authors will be asked to pay a publication fee for each article prior to the article appearing in the journal. However, this fee only needs to be paid after the article has been accepted for publishing. The fee is 380 EUR (for articles with maximum of 6 pages), 470 EUR (for articles with maximum of 10 pages), plus 50 EUR for each additional page. The additional cost for a color page is 90.00 EUR (only for a journal hard copy; optional upon author's request). These fees do not include tax.

Strojniški vestnik -Journal of Mechanical Engineering
Aškerčeva 6, 1000 Ljubljana, Slovenia, e-mail: info@sv-jme.eu

9 770039 248001
ISSN 0039-2480

http://www.sv-jme.eu

Contents

Papers